INTERFACIAL STATES, ENERGETICS, AND PASSIVATION OF LARGE-GRAIN AND THIN-FILM ANTIFLUORITE CESIUM TITANIUM BROMIDE

WPI

Jocelyn L. Mendes
A Major Qualifying Project Report
in partial fulfillment of the requirements for the
Degree of Bachelor of Science in Chemistry
submitted to the Faculty of

WORCESTER POLYTECHNIC INSTITUTE
100 Institute Road
Worcester, Massachusetts 01609

Typeset in LaTeX. Printed in the United States of America.

CONTENTS

LIST OF FIGURES

LIST OF TABLES

PREFACE

We studied the surface chemistry, atmospheric stability, and passivation of solar-relevant Cs_2TiBr_6. In particular, we studied the synthesis of both large-grain and thin film Cs_2TiBr_6. A high-temperature melt successfully produced high quality large-grain samples with >1 mm^2 facets as verified by optical microscopy and scanning electron microscopy (SEM). We confirmed synthesis using X-ray diffraction (XRD). X-ray photoelectron spectroscopy characterized the resulting surface chemistries. Following initial characterization, we established the surface basicity of interfacial bromine species on both oxide-rich and oxide-free surfaces. In an attempt to further understand metal oxide species on the Cs_2TiBr_6 surface and with pristine-material properties of particular interest, we investigated a series of physicochemical surface treatments including rinsing, abrasion, and cleaving in ultrahigh vacuum (UHV). For each surface treatment, X-ray photoelectron spectroscopy (XPS) quantified surface chemical species, while ultraviolet photoelectron spectroscopy (UPS) established valence-band structure as a function of surface treatment. Amorphous titanium oxide with crystalline cesium bromide dominates the surfaces of nascent Cs_2TiBr_6 material. UHV cleaving yielded oxide-free surfaces with excellent alignment between valence-band structure and a density functional theory (DFT)-calculated density of states, a 3.92 eV work function,

and 1.42 eV Fermi energy vs the valence band maximum. Band energetics are commensurate with moderate n-type doping for this melt-synthesized large-grain Cs_2TiBr_6. TiO_2 is well aligned with the band edges of Cs_2TiBr_6 for facile electron transport, and we hypothesized that it would act as an ideal passivation material. These findings motivated us to fabricate a Schlenk-line integrated atomic layer deposition (ALD) instrument for air-free passivation of Cs_2TiBr_6 with TiO_2 and present preliminary ALD studies on silicon and Cs_2TiBr_6 surfaces. We discuss the implications of these surface chemical and electronic results for photovoltaics.

ACKNOWLEDGMENTS

I would first like to thank Professor Grimm for being my biggest mentor at WPI and striking a balance between guidance and freedom in lab that has allowed me to grow as a scientist and has prepared me for my future in this field. Professor Grimm has taught me the most important thing about research: that is failure is part of research, and as long as you have a path forward, failure is okay. Sasha, I owe so much of the groundwork of this project to your efforts and knowledge and am so grateful for all of the skills that you taught me. This project would not have been possible without your work or expertise. I also want to thank both Alex and Julia for always being around to chat with, ask questions, or help when I break things. It was a pleasure to work with you both and I am eternally grateful for all of the knowledge I was able to gain from working with you. To Emma, I am super excited to see where you will go in the Grimmgroup and am grateful to have been able to work with you even if it was limited by COVID.

I would also like to thank David LaPré, the Early Research Experience in E-term, the WPI School of Arts and Sciences, Dean Jean King, and Professor Suzanne Weekes for financially supporting this research and providing me with opportunities to attend professional development that have prepared me for my future beyond WPI.

I want to thank my mom, dad, and Karissa for always supporting me, especially by listening to me drone on and on about lab things. You have always been happy to support whatever I want to do with my life, even if that means moving across the country to do more school. Alex, thank you for being my biggest cheerleader, and not doubting for a second that I would get into my top grad schools, even when I was unsure of myself.

J. L. M., 3 April 2021

GLOSSARY

ALD	atomic-layer deposition
$B(C_6F_5)_3$	*tris*(pentafluorophenyl)borane

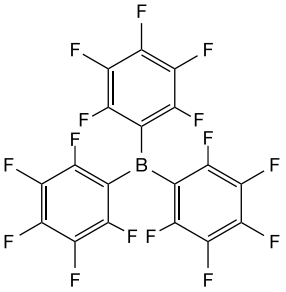

DCM	dichloromethane
DFT	density functional theory
FPT	freeze pump thaw (degassing)
fwhm	full-width-at-half-maximum

PV	photovoltaic(s)
SEM	scanning electron microscopy
TEMATi	*tetrakis*(ethylmethylamino)titanium(IV) 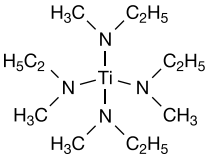
TPD	temperature programmed desorption
UPS	ultraviolet photoelectron spectra/spectroscopy
XPS	X-ray photoelectron spectra/spectroscopy
XRD	X-ray diffraction
UHV	ultrahigh vacuum
UHP	ultrahigh purity (gas)

CHAPTER 1

SOLAR ENERGY AND NONTRADITIONAL LIGHT ABSORBERS

1.1 Why Do We Care About Solar Energy?

The ten warmest years on record globally have all occurred in the 21st century, with the last decade being the warmest decade ever.[1] The greenhouse effect, in which thermal solar radiation is absorbed by atmospheric gases, paired with human activities that increase greenhouse gas quantity, is responsible for rising global temperatures.[2] Fossil fuel combustion for energy needs accounts for a majority of the yearly greenhouse gas emissions.[3] In addition, these fossil fuels, such as coal and oil, are finite and are considered non-renewable. Therefore, addressing concerns about a warming planet while also addressing long-term global energy needs requires a search for alternatives to emission-producing, non-renewable energy resources.

Among renewable energy sources, solar energy is particularly compelling. In 2011, the amount of direct solar energy that reached the Earth in one hour exceeded total global energy consumption per year.[3] As the most abundant energy resource on the planet, solar energy provides a lucrative alternative to non-renewable energy sources.

The abundance and lack of emissions associated with solar energy has driven research for several decades. The high availability of solar energy drives research into the effective collection and harnessing of this energy source.

Solar energy can be collected through several technologies, including photovoltaics that directly convert solar energy into electrical energy, solar-thermal[4] that absorb light and use the resulting heat, and solar fuels[5] that convert solar energy into energetic chemical bonds for later use. The solar-thermal and solar fuels avenues are particularly compelling with many recent advances,[6–7] however our particular attention is on materials science improvements to emerging photovoltaic systems.

Of solar electricity technologies, solar photovoltaics (PV) are widely employed with steady advancements since their inception.[8] Advances have increased both the solar-to-electric conversion efficiency as well as the cost-per-watt affordability of these technologies.[9] Solar PVs consist of several device types, including wafer and thin film devices. Single-junction, crystalline silicon solar PV devices comprise ~90% of current global solar PV production.[8] The proliferation of silicon solar PVs is due largely to the ability of scalable, cost-effective production, however these devices have a maximum theoretical thermodynamic efficiency limit of ~30% and experimental efficiencies are reaching that limit.[10] Wafer alternatives to silicon include III–V materials such as gallium arsenide (GaAs). These alternatives have higher efficiencies than silicon but are much more expensive to produce and are largely relegated to niche aerospace and military applications.[11] Thin film devices using perovskite semiconductors have also been an emerging area of research for solar PV devices, and have seen comparable efficiencies to silicon PV setups.[12–13] These devices have seen further improvements to efficiency, but many perovskites of interest contain toxic materials and exhibit stability issues.[14–15]

With the limitations of current solar PV technology in mind, present PV research is driven by metrics including earth abundance, efficiency, cost effectiveness, and low toxicity.

1.2 How Could We Improve Upon Existing Photovoltaics?

Silicon has a maximum theoretical efficiency of ~30% that commercial devices are quickly approaching.[16] Thus, the opportunity for radical improvements to photovoltaic efficiencies must re-evaluate the PV module itself. Tandem arrangements of two solar absorber materials enable efficiencies that are significantly higher than those of each component absorber. Figure 1.1A shows a Shockley-Queisser limit plot with many semiconductor absorbers vs their band gap energies, which reveals that silicon is worth pursuing in tandem arrangements for its relatively high theoretical efficiency and low cost.[17] As seen in Fig. 1.1B peak tandem efficiencies occur when the bottom absorber has a band gap of 1.0 eV and the top has a band gap of 1.6 eV.

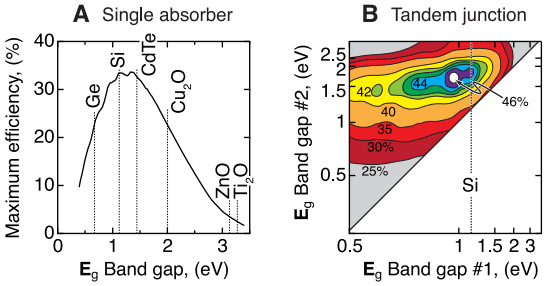

Figure 1.1 Shockley-Queisser limit plot for (**A**) single-absorber and (**B**) two-absorber, tandem-junction devices based on bulk-recombination-limited voltages, complete absorption of above-bandgap light, and ideal diode behavior.

While an idealized combination of 1.0 and 1.6 eV materials may prove elusive, the broad efficiency landscape in Fig. 1B affords combinations of other band gaps that would demonstrate performance gains relative to single-absorber devices. For instance, a combination of a bottom absorber with a band gap of 1.1 eV (dashed line) still demonstrates significant improvements over a single-absorber device. This is particularly compelling as silicon's 1.12 eV band gap energy paired with the fact that infrastructure for its production and use is quite robust. This allows for silicon PVs to remain cost effective despite efficiency limits. Therefore, improvements to efficiency of PV devices consider tandem-junction PV in which silicon is one of multiple absorbing materials. This would allow for improvements to be made upon current single junction silicon configurations without ditching the technology entirely. Silicon's 1.12 eV band gap positions it well as a bottom absorbing material in a tandem PV configuration.[18]

The top absorbing material in a dual junction tandem PV device would need to absorb higher energy light than silicon for improved efficiency as illustrated in Fig. 1.1B. Ideally, this top absorber should have a band gap energy of 1.6–1.9 eV. Therefore, we are motivated to study materials that not only possess this physical property, but also fulfill the previously mentioned performance metrics of earth abundance, efficiency, cost effectiveness, and low toxicity.

Of top absorbers, there are various candidate semiconductor materials. As mentioned, devices containing perovskites have seen rapid improvements in efficiencies and many perovskites, such as methylammonium lead iodide, have ideal band gap energies that fall within the range of 1.6–1.9 eV.[19–21] However, many candidate perovskite materials contain lead which presents toxicity concerns.[22] These concerns point towards a search for lead-free alternatives that demonstrate a ~1.8 eV band gap with good efficiencies, Earth abundance, and low toxicity.[23]

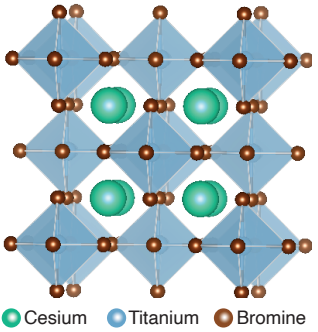

Figure 1.2 The Cs_2TiBr_6 unit cell closely resembles an antifluorite, Na_2O, structure in which polyatomic anions of $(TiBr_6)^{2-}$ octahedra occupy each unit cell corner and face, while Cs^+ cations fill all eight available tetrahedral holes.

1.3 Why Do We Care About Cs_2TiBr_6?

Cesium titanium(IV) bromide, Cs_2TiBr_6, emerges as a candidate for potential perovskite alternatives that fulfill the aforementioned performance metrics of efficiency, earth abundance, and low toxicity, while also having an ideal band gap for maximized efficiencies in tandem junction configurations with silicon.[24–25] The ~1.8 eV band gap positions Cs_2TiBr_6 as a candidate top absorber to pair with silicon in tandem PV configurations.[25] And the lack of lead, and relative earth abundance of the starting materials suggests that this material merits further study for tandem junction PV applications.

Unlike perovskites of an ABX_3 stoichiometry, with A^{n+} cations at the unit cell corners, B^{2n+} cations in the unit cell body center, and X^{n-} anions at the unit cell faces, Cs_2TiBr_6 follows a different structure. Similar to the more common potassium hexachloroplatinate, K_2PtCl_6, Cs_2TiBr_6 closely resembles an antifluorite, Na_2O, structure in which polyatomic anions of $(TiBr_6)^{2-}$ octahedra occupy each unit cell corner and face, while Cs^+ cations fill all eight available tetrahedral holes, Fig. 1.2.

Cs_2TiBr_6 is also attractive for its recent reports of promising power conversion efficiencies in thin films.[24] Despite promising PV results for Cs_2TiBr_6, much remains unknown about the chemical properties, carrier dynamics, and interfacial stability of the material. Preliminary findings suggest differing stabilities between thin film and large-grain material,[24,26] suggesting that future studies of the stability and interfacial chemistry of the material are merited to establish Cs_2TiBr_6 for solar energy conversion applications.

Herein, we discuss the implications of studying both large-grain and thin-film Cs_2TiBr_6 respectively for fundamental characterizations and for device-relevant studies. To conduct these studies, we optimized the synthesis of

large-grain and of thin-film and material. Following synthesis optimization of large-grain Cs_2TiBr_6, we studied the Lewis basicity of interfacial halides to establish reactivity and surface terminations. Additionally, we studied the effects of Lewis acid adsorption on Cs_2TiBr_6 surfaces on the stability of the material. After probing the interfacial chemistry of Cs_2TiBr_6, we studied its ambient atmospheric stability using X-ray photoelectron spectroscopy (XPS) and X-ray diffraction (XRD). We found that the surfaces readily oxidize in air to form amorphous TiO_2 and crystalline CsBr. In an effort to characterize oxide-free surfaces, we employed physiochemical polishing of the surfaces by rinsing with DCM and sanding. Physiochemical polishing proved unsuccessful in fully removing interfacial metal oxides, but UHV cleaving yielded oxide-free surfaces, with near stoichiometric atomic ratios. UHV cleaving enabled ultraviolet photoelectron spectroscopy (UPS) to characterize the energetics and band-edge energies of oxide-free material. Energetic determinations revealed that the band edge energies align well with those of TiO_2 for electron transport. To enable deposition of TiO_2 on this otherwise air-unstable material, we constructed a Schlenk-line-integrated atomic layer deposition (ALD) instrument to deposit a passivating and electron-conductive layer of TiO_2 onto Cs_2TiBr_6 surfaces directly following thin-film synthesis. With these studies, we aim to elucidate the effects of interfacial chemical states, atmospheric stability, and passivation on the electronic properties of this solar-relevant material.

CHAPTER 2

OPTIMIZATION OF SYNTHESIS, STABILITY, AND SURFACE BASICITY STUDIES OF CESIUM TITANIUM(IV) BROMIDE AND CESIUM TIN(IV) BROMIDE

Abstract

Recent reports on thin film Cs_2TiBr_6, a nontoxic, Earth-abundant solar energy conversion material, suggest promising power conversion efficiencies. Here, we optimize the synthesis of large-grain Cs_2TiBr_6 by a high-temperature melt of CsBr and $TiBr_4$ that yielded samples with $\geq$1 mm_2 facets. Following synthesis optimization, we elucidated the resulting interfacial chemical states and fundamental properties of the material. Solvent compatibility was established with DCM, acetonitrile, toluene, and 2-methyltetrahydrofuran for future adsorption and electrochemical studies. The surface basicity of interfacial bromine was established by adsorption of Lewis acids to large-grain Cs_2TiBr_6. For each adsorption study X-ray photoelectron spectroscopy (XPS) quantified surface chemical species, while X-ray diffraction (XRD) established ambient stabilities. We discuss the implications of these surface chemical and stability results for photovoltaics.

Special thanks to Weiran (Sasha) Gao for initiating these experiments and conducting initial studies.

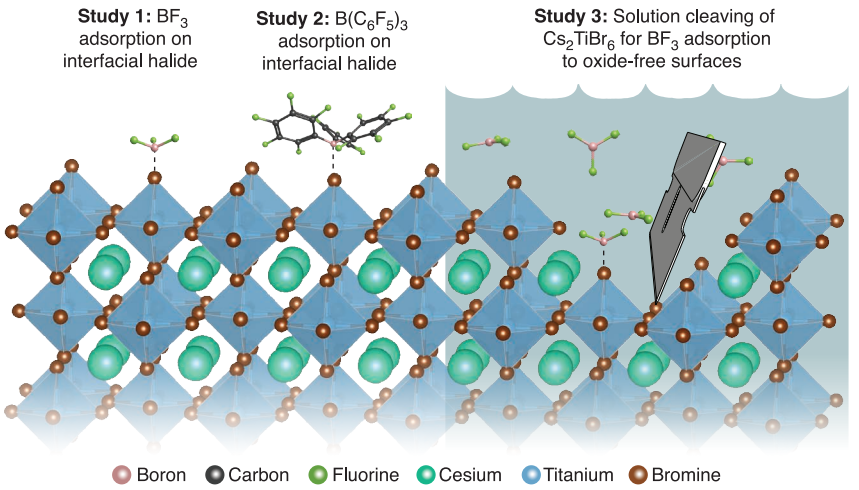

Figure 2.1 Three surface basicity studies were undertaken to probe the basicity of interfacial halide species. **Study 1** examined a 1-h reaction at room temperature with BF_3 etherate, **Study 2** employed a 1-h reaction at room temperature with a bulkier Lewis acid, *tris*(pentafluorophenyl)borane, and the subsequent ambient stability was quantified. In **Study 3**, Cs_2TiBr_6 was cleaved in a BF_3 solution and reacted for 5 min at room temperature to examine adsorption on oxide-free surfaces. All samples were studied using XPS.

2.1 Introduction

Promising preliminary PV results paired with conflicting reports of atmospheric stability prompt further study of Cs_2TiBr_6.[24] In this chapter, we aimed to synthesize high quality, large-grain Cs_2TiBr_6 material and study the surface basicity of the resulting material to elucidate the interfacial chemistry and stability of the material.

Here we explore the optimization of synthesis, stability, and early surface studies of Cs_2TiBr_6 and Cs_2SnBr_6. While a majority of efforts focused on Cs_2TiBr_6, we additionally explored the synthesis of Cs_2SnBr_6 for its possible increased atmospheric stability over the titanium-based material. However, little work was performed in optimizing the synthesis of the tin-based material and offers the opportunity for future study.

This chapter breaks the surface basicity experiments into three components, titled **Study 1**, **Study 2**, and **Study 3**. Figure 2.1 depicts these studies.

Study 1, as in Fig. 2.1, aimed to study the surface basicity of interfacial halides in the presence of Lewis acids with small ligands. We chose BF_3·etherate for this study for the small size of BF_3 and the detectability of said substituents in XPS. *We hypothesize* that BF_3 will adsorb to interfacial Br^- species.

Study 2, shown in Figure 2, aimed to study the surface basicity and subsequent stability of interfacial bromines in the presence of Lewis acids with bulky ligands. The bulky Lewis acid chosen for this study was *tris*(pentafluoro phenyl)borane, $B(C_6F_5)_3$, for its bulky phenyl ligands and the multitude of XPS detectable fluorine substituents. *We hypothesize* that $B(C_6F_5)_3$ will adsorb to bromine at the Cs_2TiBr_6 surface and improve atmospheric stability.

Following the results of **Study 1** and **Study 2**, we undertook an additional study. **Study 3** aimed to study the surface basicity of interfacial halides on oxide-free Cs_2TiBr_6 surfaces. This study recognized the presence of metal oxides at the Cs_2TiBr_6 surface and aimed to deconvolve the location of adsorption of Lewis acids by reacting oxide free interfaces with BF_3. To ensure no oxides were present during adsorption, the BF_3 was complexed with pyridine to exclude etherate and the crystal was cleaved directly in the reaction solution, as seen in Fig. 2.1. *We hypothesize* that BF_3 will adsorb to basic bromines on oxide free Cs_2TiBr_6 surfaces. With these studies, we aim to elucidate the effects of optimized synthetic conditions, Lewis acid adsorption, and atmospheric stability on the properties of this solar-relevant material.

2.2 Experimental

2.2.1 Materials and Chemicals

All chemicals were used as received unless otherwise noted. Chemicals used in the synthesis of cesium titanium bromide included cesium bromide (CsBr, 99.9% trace metals basis, Sigma Aldrich), and titanium(IV) bromide ($TiBr_4$, 98%, Sigma Aldrich) that was further purified by sublimation. Dichloromethane (DCM, ACS Grade, Fisher), methanol (anhydrous, 99.8%, Sigma Aldrich), diethyl ether (anhydrous, 99.8%, Sigma Aldrich), acetonitrile (anhydrous, 99.8%, Sigma Aldrich), dimethyl sulfoxide (DMSO, anhydrous, 99.8%, Sigma Aldrich), 2-methyltetrahydrofuran (2-MeTHF, anhydrous, 99.0%, Sigma Aldrich), and toluene (anhydrous, 99.8%, Sigma Aldrich) were dried in a commercial solvent drying system and were further degassed then stored over molecular sieves (3Å, Alfa Aesar, freshly activated prior to use). Pyridine and ethylene glycol were vacuum distilled, degassed and stored over molecular sieves. A Milli-Q filtration system provided all water at 18 MΩ cm resistivity (Millipore). Chemicals used in adsorption studies on Cs_2TiBr_6 surfaces included boron trifluoride diethyl etherate ($BF_3{\cdot}O(CH_2CH_3)_2$, 46.5% BF_3, Alfa Aesar), *tris*(pentfluorophenyl)borane ($B(C_6F_5)_3$, 95%, Sigma Aldrich) were used as received.

2.2.2 Instrumentation for Synthesis

Inert environments for sample synthesis, processing, reactions, and storage included an argon-purged (ultrahigh purity, UHP, Airgas) Schlenk line

equipped with an oil diffusion pump having a base pressure below 1×10^{-3} torr. Larger inert environments included a nitrogen-purged (UHP, Airgas) recirculating glove box (mBraun Inc., Stratham, NH) with an active catalyst to maintain oxygen concentrations below 1 ppm, as measured by a commercial O_2 sensor. A commercial N_2 generator (Model N2-45, Parker Balston, Lancaster, NY) provided the atmosphere for a flush box (Terra Universal, Fullerton, CA) with an O_2 concentration below 5 ppt (thousand), as measured at a commercial O_2 sensor.

Ampoules were sealed in an in-house built tube-sealing apparatus described in Chapter 3, In brief, the apparatus is built around a repurposed rotary evaporator (Rotavapor R110, BÜCHI) to rotate the tube during in vacuo sealing to assure even, consistent heating, and steady, safe flamework. In place of a solvent trap, a direct connection to the Schlenk line affords high vacuum conductivity and rapid pumping (50 mm Rotavap flange adapter, Adams & Chittenden Scientific Glass Coop., Berkeley, CA). Sealing against the rotavapor vacuum gasket, a 6061 aluminum tube replaces the standard vapor tube and with a bottom connection consisting of a KF flange in place of a traditional 24/40 ₹ fitting. For sealing, a loaded tube was transferred to the sealing apparatus and initially evacuated with the butterfly valve closed to minimize possible contamination of the highly reactive $TiBr_4$ with oxygen. Prior to opening the butterfly valve, the reactants at the bottom of the ampoule were submerged in liquid nitrogen to minimize unwanted vacuum sublimation of $TiBr_4$. Following evacuation of the connecting tubing, the butterfly valve was opened to the Schlenk line slowly to fully evacuate the quartz tube. The quartz tube was rotated at ~1 Hz and a propane-oxygen flame sealed the tube to yield a 22–25-cm-long ampoule.

High-temperature melt syntheses utilized horizontally mounted 5-cm-I.D. tube furnaces that were constructed from two abutting tubular ceramic heaters (CRFC-series, Omega Engineering, Norwalk, CT). A 30-cm-long and a 15-cm-long heater defined two independently controlled heating zones. Temperature controllers (Love 32B, Dwyer Instruments, Michigan City, IN) recorded temperatures at K-type thermocouples (Nextel ceramic braid insulation, Omega Engineering, spot welded in house) that were positioned at the center of each zone. An in-house-written LabVIEW program interfaced with the temperature controllers for conducting temperature ramp-soak-and-cooling profiles and recording temperature data.

2.2.3 Synthesis and Optimization of Large-Grain Cs_2TiBr_6 Crystals

A multivariate design-of-experiments approach was employed to optimize the synthesis of Cs_2TiBr_6 crystals with success quantified by a visual inspection of facet size and shape. To minimize the number of variables involved, syntheses utilized 19-mm-diameter quartz ampoules that were loaded in the recirculating glovebox. All syntheses occurred in a two-zone tube furnace.

Varied parameters included starting material preparation and quantities and temperature profiles during synthesis. A breakdown of experimental conditions across each batch can be found in Table D.1 in Appendix D. Section §A.2 details the preparation of quartz ampoules.

CsBr and $TiBr_4$ were measured in the recirculating glovebox, loaded into a clean, dry quartz ampoule using a glass funnel, and sealed with a KF-flange adapted butterfly valve. After tube loading, the ampoules were transferred to a Schlenk line-adapted tube sealing setup detailed in §A.2, sealed under vacuum, and transferred to a two-zone tube furnace. Figure 2.2A illustrates the typical orientation of the sealed reaction ampoules in the two-zone tube furnace. The reaction ampoules were loaded into the tube furnace so that the end with the reactants was in the front end of the furnace and the end with no reactants was in the back end of the furnace. Some runs utilized a fiber quartz plug, illustrated in Fig. 2.2A, which was placed about halfway into the furnace to tilt the reaction ampoule so that the reactants remained at the front end without creeping up the sides of the ampoule, or flowing while in a molten state.

2.2.3.1 Variation of Starting material preparation and quantity Starting material quantity and preparation was the first variable to be considered while optimizing the synthesis of Cs_2TiBr_6 to yield high-quality material. We varied reagent quantities to yield ~1–3 g of total starting material (CsBr and $TiBr_4$). The starting materials were either loaded into quartz ampoules stoichiometrically, with a 5% $TiBr_4$ excess, or with a 10% $TiBr_4$ excess. Grinding of starting materials in the glovebox prior to loading in quartz ampoules was also attempted on some batches. For batches that employed grinding of starting materials, the reagents were measured and combined in a mortar and ground with a pestle. After reagents were well combined, they were loaded into the ampoule using a funnel. The funnel was specifically employed to minimize contamination of the ampoule sidewalls that might otherwise interfere with the proper flame sealing or degrade the stability of the quartz ampoule at the point of heating.

2.2.3.2 Variation of temperature profiles Following attempts to optimize the preparation and quantity of starting materials, we varied the temperature programs to optimize the nucleation of multifaceted, large-grain material through the high-temperature melt synthesis. As demonstrated by Figure 2.2B, a general temperature program included a ramp step for both the back and front thermocouples to the heating temperature, followed by holding at a soak step for a given time, and ending with a linear cooling step to room temperature. The T_{heating} parameter was the first variable that was changed, and was varied between 200 and 800 °C. The T_{heating} values that were below 650 °C yielded unsuccessful melting of the CsBr starting material and were not considered further.

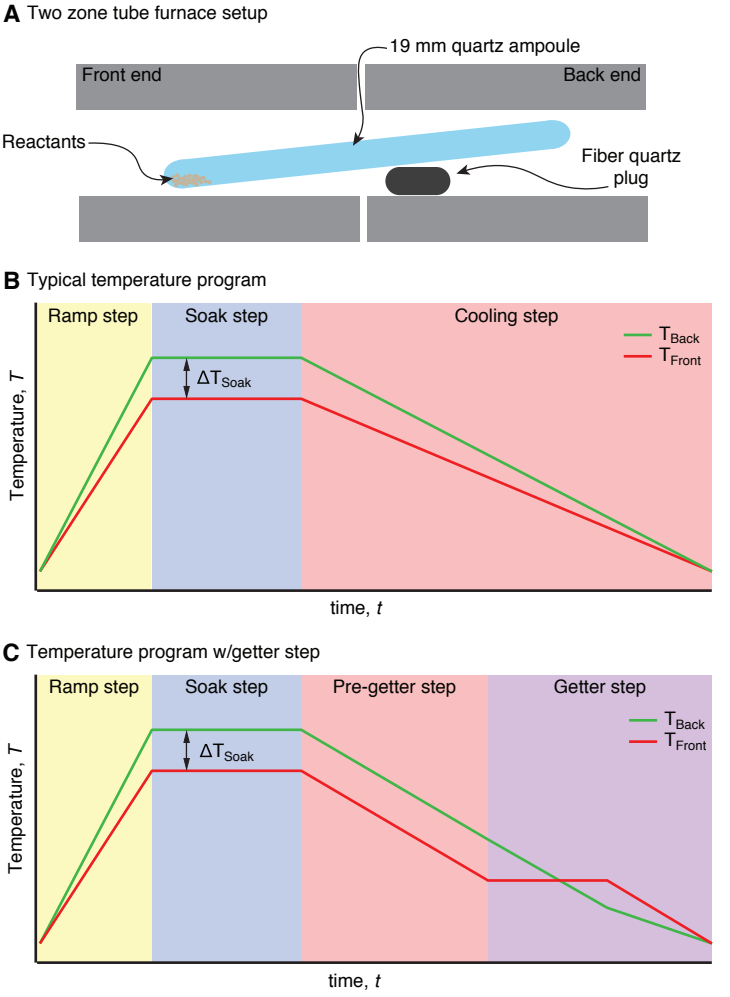

Figure 2.2 Two zone tube furnace set-up (**A**) for high temperature melt syntheses of Cs_2TiBr_6 contains sealed, 19 mm quartz ampoules which sit with the reactants in the front end and the back end raised by a fiber quartz plug to keep growth local to the front end of the ampoule. A typical temperature program for high temperature melt (**B**) contains three main steps: a ramp to heating temperatures, a soak at heating temperatures, and a linear ramp to room temperature. The temperature at the front end of the two-zone tube furnace is represented by the red line (T_{Front}) and the temperature at the back end is represented by the green line (T_{Back}). A ΔT during the soak step was employed with the back end always being held at a hotter temperature than the front end. Temperature programs with a getter step (**C**) were attempted to getter excess $TiBr_4$ vapor towards the back end of the reaction ampoule. This step was added during the cooling step and switched which end of the furnace was the hotter end. In a typical temperature program with a getter step, an inversion of which end was the hotter end occurs around ~250 °C, the melting point of $TiBr_4$.

Next, the multi-zoned nature of the tube furnace was manipulated to heat the front and back of the reaction ampoule at different temperatures. Figure 2.2A illustrates which end of the reaction tube is considered the front and which is considered the back. A tilt of the ampoule in which the front end was lower than the back end was utilized in some batches in order to keep nucleation at the front end of the ampoule and can be seen in Figure 2.2A. The tilt was enabled by a small piece of fiber quartz placed halfway in the furnace.

In varying the $T_{\text{soak, front}}$ and $T_{\text{soak, back}}$ temperatures during heating, the front end was always kept at a colder temperature as compared to the back end. The only time in which the front end was at a hotter temperature than the back end was when we attempted a getter step during cooling to draw excess titanium bromide away from the crystals. In our hands, this getter step was unsuccessful at producing high-quality, faceted material. The ΔT for the temperature of the back end as compared to the front end typically varied by +20–50 °C. The ΔT was maintained during the ramp and cooling steps as well to keep the T_{front} lower than the T_{back} to prevent condensation of $TiBr_4$ at the back end.

After varying soak temperatures and ΔT between the front and back end of the reaction ampoules, the duration of temperature programs was varied to improve mixing of liquid CsBr and gas phase $TiBr_4$ and to improve nucleation during cooling. The duration of ramping, tramp, to T_{soak} was varied between 0 and 1800 min. The duration of holding, t_{soak}, at T_{soak} was varied between 30 and 1800 min. Following optimization of heating parameters, the duration of the cooling step, t_{cooling}, was varied. t_{cooling} ranged between 600 and 9400 min. For a more detailed account of all temperatures, t_{ramp}, t_{soak}, t_{cooling}, and ΔT see Table D.1 in Appendix D.

To address the condensation of $TiBr_4$ vapor onto Cs_2TiBr_6 surfaces and the reaction ampoule in reactions that utilized a 5–10% stoichiometric excess of $TiBr_4$, a getter step was attempted. Figure 2.2C plots a temperature program that employed a getter step to draw the $TiBr_4$ vapor towards the back end of the reaction ampoule during cooling to promote condensation of excess $TiBr_4$ away from the synthesized crystals. This getter step was attempted near the melting temperature of $TiBr_4$ (230 °C). As demonstrated by the plot in Fig. 2.2C, when the pre-getter cooling temperature reached 250 °C the T_{front} was held at 250 °C while the T_{back} was allowed to continue to cool linearly. This resulted in the front end of the reaction ampoule becoming the hotter end, in an effort to drive the $TiBr_4$ vapor to the back end. After 10 h, the temperature at the front end was cooled linearly. This resulted in the front end of the ampoule being hotter for the remainder of cooling.

While optimizing the synthesis of T_{front}, we were interested in determining when nucleation occurred (during heating or cooling). In order to elucidate this, we sealed an already synthesized T_{front} crystal into a quartz ampoule, placed it into one of our clamshell furnaces that can be opened from the top

and heated the crystal up to 680 °C. After 5–10 min of heating, we opened the furnace and recorded visual observations about whether the material was liquid or solid at heating temperatures. The experimental section of Chapter 3 contains more details about the chosen optimized synthetic protocol.

2.2.4 Cs_2SnBr_6 Synthesis and Characterization

We synthesized Cs_2SnBr_6 by a high temperature melt using optimized Cs_2TiBr_6 parameters. As with Cs_2TiBr_6, the Cs_2SnBr_6 precursors (CsBr and purified $SnBr_4$) were loaded in quartz ampoules in the glovebox and sealed under vacuum. Temperature programs for the Cs_2SnBr_6 synthesis followed the optimized Cs_2TiBr_6 temperature programs. These temperature programs included a 15 h linear ramp to 680 and 710 °C, a 25 h soak at 680 and 710 °C, followed by a 96 h linear ramp to 0 °C in both zones.

The resulting Cs_2SnBr_6 was characterized by both X-ray diffraction (XRD) and X-ray photoelectron spectroscopy to confirm successful synthesis.

2.2.5 Solvent Stability of Cs_2TiBr_6

After optimizing the synthetic variables to yield high-quality, large-grain Cs_2TiBr_6, we studied the material's stability in a variety of solvents to find solvents that would orthogonally etch $TiBr_4$ from Cs_2TiBr_6 surfaces without modifying the chemistry of the Cs_2TiBr_6 surfaces. In addition, solvent stability was considered in an effort to find solvents that could be used in future adsorption studies and photoelectrochemical testing.

Each solvent stability study was conducted using degassed, dry solvents in the flush box. Generally, the protocol for testing the solvent stability of a surface went as follows. First, 10–20 mg of powdered Cs_2TiBr_6 was placed at the bottom of a clean 5 mL vial. Next, ~2 mL of the desired dry solvent was pipetted into the vial. The vial was sealed and swirled around. Optical changes, including color changes of the powder and color changes of the solvent were recorded. For solvents that did not affect a color change, XPS scanned the resulting samples to determine whether the lack of color change correlated to the solvent not modifying or reacting with the Cs_2TiBr_6 surface.

The solvents employed included dichloromethane (DCM), methanol, ethylene glycol, pyridine, dimethyl sulfoxide (DMSO), diethyl ether, toluene, acetonitrile, propylene carbonate, 2-methyltetrahydrofuran (2-MeTHF). Outside of the flush box, similar stability studies utilized DI water and acetone.

2.2.6 Study 1: BF_3 Adsorption

In the recirculating glovebox, a DCM rinsed and sanded Cs_2TiBr_6 crystal was added to a Schlenk flask. The Schlenk flask was transferred to the

Schlenk line, evacuated and placed under argon. A 0.2 mmol equivalent of BF_3 was syringe transferred to another evacuated Schlenk flask under argon containing 10 mL of dry DCM. To rinse the crystal, 10 mL of dry DCM was cannula transferred into the flask containing the crystal and then cannula transferred to waste. The BF_3 solution was then cannula transferred to the flask containing the crystal and the reaction occurred for 1 hour at 25 °C. After the reaction the BF_3 solution was cannula transferred to waste and the crystal was rinsed 3 times with 10 mL of dry DCM. The Schlenk flask was subsequently transferred back to the flush box for mounting on an XPS puck and affected with carbon tape. The puck was loaded in a vacuum suitcase and transferred to the XPS instrument for surface analyses.

2.2.7 Study 2: Tris(pentafluorophenyl)borane Adsorption and Atmospheric Stability

Tris(pentafluorophenyl)borane, $B(C_6F_5)_3$, was adsorbed to both powdered and large-grain Cs_2TiBr_6. Large-grain crystal samples were prepared by the same method as detailed in the BF_3 etherate study. A DCM rinsed and sanded crystal was added to a Schlenk flask in the recirculating glovebox. The Schlenk flask was transferred to the Schlenk line, evacuated and placed under argon. Next, 1 mmol of the $B(C_6F_5)_3$ solid was measured in the glovebox and added to a Schlenk flask. On the Schlenk line under argon, addition of 10 mL of dry DCM to the $B(C_6F_5)_3$ via cannula transfer yielded a 0.1 M solution of $B(C_6F_5)_3$. Cannula transfer of dry DCM over the Cs_2TiBr_6 crystal followed by removal of the DCM via cannula served to remove any interfacial $TiBr_4$ prior to reaction with the borane species. Via cannula transfer, the 0.1 M $B(C_6F_5)_3$ solution submerged the Cs_2TiBr_6 crystal for 1 h at room temperature. After the 1 h reaction period, the $B(C_6F_5)_3$ solution was cannula transferred to waste and the crystal was rinsed 3 times with 10 mL of dry DCM. The Schlenk flask was subsequently transferred back to the flush box for mounting on an XPS puck and affected with carbon tape. The puck was loaded in a vacuum suitcase and transferred to the XPS instrument for surface analyses.

For powdered samples, the DCM rinsed cesium titanium bromide powder was placed in a 5 mL vial in the flush box. For these experiments, 1 mmol of the $B(C_6F_5)_3$ was dissolved in 10 mL of dry DCM. To the vial containing the crystal powder, a clean stir bar and the $B(C_6F_5)_3$ solution in DCM was added. The reaction occurred with stirring in the flush box at room temperature for 1 hour. The DCM/$B(C_6F_5)_3$ solution was poured into waste and the powder was rinsed 3 times with 10 mL equivalents of dry DCM. The $B(C_6F_5)_3$ adsorbed powder was transferred to a Teflon XRD sample holder and sealed with Kapton tape to exclude air. Sample scanning was completed once with the Kapton tape on the sample for an air-free scan. Subsequent removal of the Kapton tape and successive and repetitive sample scanning in 10 min

intervals at 2θ angles of 28–30.5° established a time evolution of oxidation with $B(C_6F_5)_3$ adsorbed to the surface.

2.2.8 Preparation of BF_3·Pyridine Complex

A protocol established by Chénard et al.[27] yielded a BF_3·pyridine complex. Purging cycles of evacuation and argon filling yielded a Schlenk flask for the reaction. A hypodermic needle transferred the BF_3·etherate from its septum-sealed reagent bottle that additionally contained an argon connection to the Schlenk link to maintain positive atmospheric pressure. Prior to hypodermic transfer, three successive cycles of filling the needle with the positive argon atmosphere above the BF_3·etherate and evacuation in air flushed oxygen from the dead volume of the hypodermic needle and syringe. Following the third purge, the syringe transferred 50 mmol (2 equiv, 6.4 mL) of $BF_3{\cdot}O(CH_2CH_3)_2$ into the Schlenk flask. Next, 25 mmol (1 equiv, 2mL) of degassed, dry pyridine was cannula transferred to the flask containing the $BF_3{\cdot}O(CH_2CH_3)_2$. Following one hour submersion in an ice bath, a cloudy, white precipitate had formed in the brown pyridine solution, which was the desired BF_3·pyridine complex. The flask warmed to room temperature and then was filtered in the flush box by rinsing with additional dry, degassed pyridine over filter paper. A typical yield was ~0.05 g. The BF_3·pyridine complex was transferred to a 1 mL vial and stored in the recirculating glovebox until use. Removal of the white precipitate from the Schlenk flask was difficult and required scraping the sides of the Schlenk flask, a modified method for easier extraction in the flush box is discussed below.

An alternative extraction protocol of the BF_3·pyridine complex from the reaction flask involved using a pressure vessel instead of a Schlenk flask. The pyridine and BF_3 etherate were combined in the flush box and sealed in a pressure vessel with a stir bar. The pressure vessel was then removed from the flush box and stirred in an ice bath for an hour. After the reaction, the same extraction protocol was enacted in the flush box. This method resulted slightly higher yields of ~0.1–0.05 g of the complex due to the flatter shape of the pressure vessel which allowed for easier scraping of the sides.

2.2.9 BF_3·Pyridine Complex Adsorption

We adsorbed the BF_3·pyridine complex to oxide-free antifluorite crystal surfaces. The complex was synthesized to exclude the ether from the reaction and minimize oxidation at Cs_2TiBr_6 surfaces. To adsorb to oxide free surfaces, Cs_2TiBr_6 crystals were cleaved in a DCM solution of the complex. In the recirculating glovebox, a 1 mmol solution of the complex was created by dissolving the complex into ~10 mL of DCM. The sparingly soluble nature of the BF_3·pyridine complex required that the mixture be shaken vigorously in a sealed vial for 15 min. The solution was transferred to a petri dish for

cleaving in which metal tweezers held a Cs_2TiBr_6 crystal in place in the petri dish while a razor blade pushed down in between the tweezers to cleave the sample in half as it was submerged in the BF_3-containing solution. Care was taken to cleave gently, so as to not shatter the brittle sample. Once successfully cleaved, the crystal was left in the solution for 5 min. After the reaction, the sample was rinsed 3 times with DCM. The rinsed sample was immediately mounted onto an XPS puck using carbon tape, loaded into the vacuum suitcase, and transferred to the XPS for pumping and scanning.

2.3 Results

2.3.1 Synthesis Optimization of Cesium Titanium(IV) Bromide and Cesium Tin(IV) Bromide

The multivariate, design-of-experiments approach to optimizing the synthesis of Cs_2TiBr_6 yielded large-grain samples with >1 mm^2 facets. We present in detail the outcome of tuning different aspects of the synthetic protocol and we discuss the optimal protocol to yield high quality large grain material.

When varying starting material preparations and loadings, we found that loadings with ~3 g of total reagent material most consistently yielded the desired crystal sizes. Loadings with less than 2 g of total starting material resulted in nucleation that occurred on large sections of the reaction ampoule. Nucleation on large areas of the reaction ampoule resulted in a thin, dark red layer of Cs_2TiBr_6 covering ~5 cm^2 of the reactant end of the ampoule and required scraping with a razor blade for removal. The scraping with a razor blade extracted a fine powder of the material, that was ideal for XRD studies but did not yield any large-grain facets that were necessary for adsorption, stability, and cleaving experiments. Therefore, loadings below 3 g of total reagent materials were not considered further.

Beyond reagent quantity, we additionally explored physical mixing of the starting materials prior to loading in quartz ampoules by grinding with a mortar and pestle. This preparation of the starting materials did not improve the physical appearance, number of facets, or size of facets on resulting large-grain samples and was therefore not considered further. We determined that batches with a ten percent $TiBr_4$ excess were most successful in producing desired large-grain material, as confirmed by XPS. However, this stoichiometric excess also yielded $TiBr_4$ contamination on the surface of the Cs_2TiBr_6 samples in addition to condensation of $TiBr_4$ at the front end of the reaction ampoule during cooling.

Temperature programs had the most influence on crystal size, quality, and facets. Figure 2.3 shows the variability of crystal quality and facets based upon changes made to the temperature programs. Figure 2.2B in the experimental section provides an example of a typical temperature program.

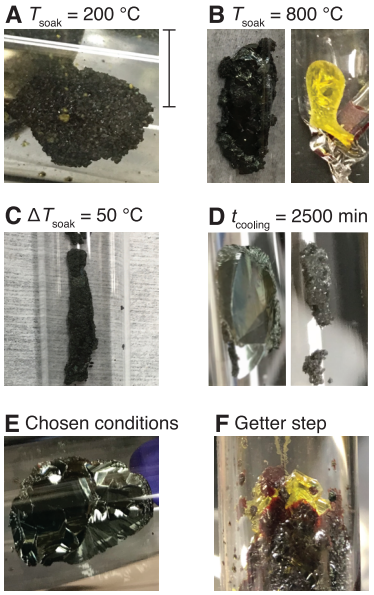

Figure 2.3 Optical images of Cs_2TiBr_6 crystals synthesized by high temperature melt and varying heating temperatures, ΔT, cooling, and duration of heating. Crystals synthesized at temperatures below the melting point of CsBr (**A**) appeared gritty and contained no facets. Crystals synthesized at temperatures significantly higher than the melting point of CsBr (**B**) saw deposition of $TiBr_4$ at the back end of the reaction ampoule and crystals with no visible facets. Variations of ΔT that were greater than ~30 °C (**C**) also resulted in gritty crystals with little to no facets. Crystals synthesized using shorter $t_{cooling}$ durations (**D**) contained a mixture of samples with visible facets and gritty, unfaceted crystals. Crystals synthesized using the optimized conditions (**E**) contained >1 mm^2 facets. Crystals synthesized using a getter step (**F**) had $TiBr_4$ recrystallized around the synthesized crystal. The scale bar in the top left represents 1 cm for each of the images shown.

Programs with T_{soak} temperatures that were below the ~630 °C melting temperature of the CsBr starting material were unsuccessful in effecting high-temperature-melt synthesis. Figure 2.3A illustrates that a T_{soak} below ~630 °C produced granular, gritty looking samples. Conversely, when T_{soak} went significantly above the ~630 °C melting point of CsBr, growth runs resulted in deposition of $TiBr_4$ at the back end of the reaction ampoule, and resulted in $TiBr_4$-deficient samples, as seen in Figure 2.3B. The left-hand frame of Fig. 2.3B presents a typical lumpy $TiBr_4$-deficient crystal from the front zone, while the right-hand frame reveals $TiBr_4$ deposition at the back end of the growth tube. A T_{soak} of ~680 °C at the reactant end of the ampoule was chosen based upon these findings.

The last exploration of growth temperatures varied ΔT between the front and back end of the reaction ampoules. The back end remained hotter than the front end in an effort to drive the $TiBr_4$ towards the cooler front end where the liquid CsBr was located. The ΔT between the front end and back end ranged from 20–50 °C. Figure 4C illustrates a run in which the heating temperature difference between the front and back end was ΔT = 50 °C (e.g. $T_{soak,\,front}$ = 680 °C and $T_{soak,\,back}$ = 730 °C). As demonstrated by the image in frame C, such a large ΔT resulted in the formation of a long, gritty crystal with no visible facets. A ΔT_{soak} of 30 °C was chosen based upon these findings where the front-end soak temperature was held at 680 °C and the back end was held at 710 °C during the soak step.

After establishing temperature ranges, subsequent investigations varied the durations of ramping, heating, and cooling time periods. First, the tramp to the heating temperature was varied between 0 and 1800 min. Ramping below 900 min resulted in gritty crystals with no visible facets. Ramping times above 900 min demonstrated little to no difference in crystal quality or facet size. Based upon this, 900 minutes was chosen as the tramp to minimize the duration of ramping while also producing high-quality material. The duration of the soak step was then varied between 30 and 1800 min. Soak durations below 900 min resulted in crystals with little to no facets, while soaking for 900 min resulted in a few facets mixed with some gritty material. Soak step durations ranging between 1500 and 1800 min resulted in highly faceted material with >1 mm^2 facets as demonstrated by the image of a sample that was held at the soak step for 1500 min in Fig. 2.3E. The duration of linear ramping to 0 °C, or $t_{cooling}$, was varied next. The $t_{cooling}$ values ranged between 600 and 9400 min. Cooling durations ranging between 600 and 4500 min resulted in material that had little to no facets and material that had crept up the sides of the reaction ampoule, coating it in a thin layer of Cs_2TiBr_6. Figure 2.3D illustrates a typical crystal with a $t_{cooling}$ that was too fast. The image on the left of frame D demonstrates high-quality facets but the remainder of the material produced from a shortened cooling duration is represented by the image in the right of the frame, indicating that nucleation can occur at the beginning of and during cooling. Longer cooling durations above 5600 min resulted in high-quality, polycrystalline, multi-faceted material. A cooling duration that lasted longer than 7800 min yielded no additional improvements in facet area or crystal visual quality and was and deemed gratuitous and unnecessary. Therefore, we selected a cooling duration of 6500 min. The optimization of temperature program durations resulted in an ideal temperature program that lasted for ~144 hours or ~6 days.

Figure 2.3F shows a Cs_2TiBr_6 sample that was synthesized using a getter step. As seen in frame F, $TiBr_4$ crystallized around the edges of the crystal, meaning that the getter step was unsuccessful in driving the $TiBr_4$ to the back end of the reaction ampoule. In our hands, multiple attempts to employ a getter

Table 2.1 Stability Observations of Cs_2TiBr_6 in Various Solvents

Solvent	Observation
Water	Dissolved, no color change
Acetone	Dissolved, white precipitate
DCM	No dissolution, solution turned yellow in presence of excess $TiBr_4$
DMSO	Slowly dissolves, no color change
Acetonitrile	No dissolution or color change
Toluene	No dissolution or color change
Ethylene glycol	Slowly dissolved, solution turned dark red
Propylene carbonate	Very slow dissolution
2-MeTHF	No dissolution or color change

step were unsuccessful in driving the $TiBr_4$ vapor to condense in the back end of the reaction vessel, away from the cooling crystal samples.

Each of these optimization parameters resulted in a high-temperature melt synthesis that yielded large-grain, high-quality, multi-faceted Cs_2TiBr_6 samples. When cut with a razor blade to specific sizes for the subsequent studies detailed in this chapter, care had to be taken to not shatter the crystals as they were brittle. Chapter 3 discusses more in-depth optical and scanning electron microscopy (SEM) imaging of high-quality material.

Cs_2SnBr_6 synthesis yielded gritty, granular yellow-green crystals. This material was not faceted and given time constraints of the project, was not pursued beyond a few syntheses. The Cs_2SnBr_6 crystals demonstrated improved ambient atmospheric stability and stability in water that was not observed for Cs_2TiBr_6 crystals. Given the overall time constraints of the project, the optimization of Cs_2SnBr_6 growth and its subsequent analyses represents an important target for future study.

2.3.2 Solvent Stability

To establish solvent compatibility for etching, adsorption, and photoelectrochemical studies several solvents were tested on Cs_2TiBr_6 to establish solvent stability. Two solvents, water and acetone, were observed in air while rinsing powdered samples from vials. Water completely dissolved the samples, while acetone dissolved the powder but left a white precipitate. Many dried, degassed solvents were tested on Cs_2TiBr_6 surfaces in the flush box. Table 2.1 provides visual observations of the result of rinsing Cs_2TiBr_6 with each solvent.

Based on visual observations from rinsing Cs_2TiBr_6 with a range of dried, degassed solvents, DCM was chosen as a candidate for future chemical polishing studies. DCM dissolved $TiBr_4$ while not reacting with Cs_2TiBr_6 surfaces. Rinsing with DCM yielded a light-yellow-hued solution. Subsequent rinses of Cs_2TiBr_6 in DCM resulted in a lighter and lighter color of yellow until the solution was clear, indicating that the DCM was only dissolving unreacted $TiBr_4$. These observations suggested that DCM would be an excellent candidate for orthogonal etching of $TiBr_4$ without changing the surface chemistry of the Cs_2TiBr_6.

In addition to observations about DCM, tests of acetonitrile, toluene, and 2-MeTHF did not induce any dissolution or color change when applied to Cs_2TiBr_6 surfaces. This merits further consideration of these solvents for photoelectrochemistry, with acetonitrile being particularly valuable to non-aqueous photoelectrochemistry.

2.3.3 Studies 1 and 2: Surface Basicity via $B(C_6F_5)_3$ and BF_3·etherate

Utilizing established solvent stability, adsorption studies were undertaken using DCM as a solvent. DCM was chosen for its ability to orthogonally etch $TiBr_4$ off of samples without reacting with the Cs_2TiBr_6 surfaces. These adsorption studies aimed to elucidate the surface basicity of interfacial halides at the Cs_2TiBr_6 surface. The two chosen Lewis acids for these surface basicity studies were boron trifluoride etherate (**Study 1**) and *tris*(pentafluorophenyl) borane (**Study 2**). These Lewis acids were chosen for the presence of fluorine, as fluorine is easily detectable in XPS. Confirmation of surface adsorption of BF_3·etherate and $B(C_6F_5)_3$ onto Cs_2TiBr_6 surfaces was conducted by identifying fluorine features in XPS.

Figure 2.4 presents the representative Cs $3d_{5/2}$, F 1s, O 1s, Ti 2p, C 1s, and Br 3d X-ray photoelectron regions as a function of surface preparation. Preparations in Fig. 2.4 include (A) a sanded and DCM rinsed sample, (B) a BF_3-adsorbed sample, and (C) a $B(C_6F_5)_3$ adsorbed sample. A sanded and DCM rinsed sample was chosen as the "control" as crystals used in the adsorption studies were sanded and rinsed with DCM prior to being transferred into each respective reaction flask. Due to the extremely air sensitive nature of these samples, we recognize that surface oxidation may take place during the surface processing involved in the adsorption studies that is commensurate with additional TiO_2 formation at the Cs_2TiBr_6 interface. This consideration is discussed further in §3.3. Figure 2.4 normalizes the spectra between frames based on the cumulative area of all presented features.

Each representative spectrum in Fig. 2.4 has a characteristic Cs $3d_{5/2}$ feature at ~723 eV that we attribute to lattice Cs^+. Small shifts in the location of this peak, as seen in frame B, are attributed to the charge neutralization that was required to combat surface charging and differed between each sample. In

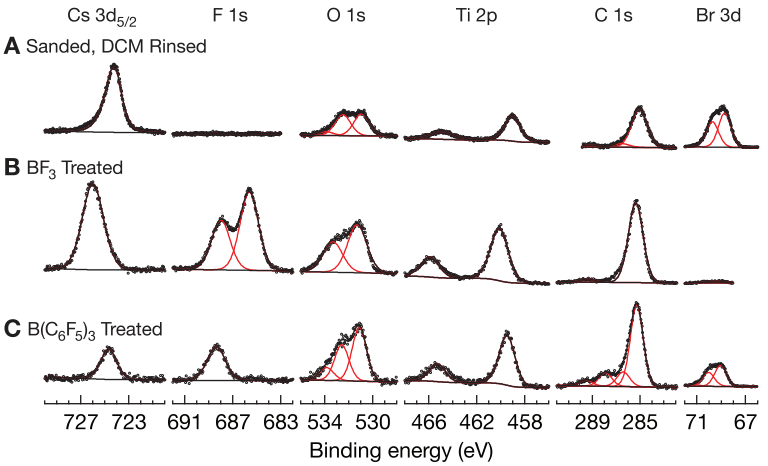

Figure 2.4 Representative XP spectra of (**A**) sanded and rinsed, (**B**) BF_3 in ether (following sanding and rinsing), (**C**) *tris*(pentafluorophenyl)borane (following sanding and rinsing) Cs_2TiBr_6 samples. Sanded and rinsed surfaces demonstrate no observable fluorine while BF_3 and $B(C_6F_5)_3$ treated samples have large F 1s features. Oxide features and organic contaminants increase following surface treatments. All samples were processed and transferred to the analysis chamber in inert environments to exclude air. The total *y*-axis amplitude of photoelectron counts is normalized between each frame.

frame A, the absence of detectable F 1s signal indicates no surface fluorine species, as expected for sanded and DCM control samples. Frames B and C both contain detectable F 1s signals, with frame B containing a fluorine doublet, at ~685 eV and ~689 eV, and frame C containing a singular F 1s feature, at ~689 eV. The relative peak areas of the F 1s features on both the BF_3 and $B(C_6F_5)_3$ treated samples indicates multilayer coverage.[28–29] This could be due to the hour-long duration of the reaction. **Study 3** considered shorter reaction times to effect monolayer coverages. The doublet in the F 1s XP spectra of BF_3 treated Cs_2TiBr_6 surfaces was unexpected, as each of the three fluorine atoms is bound to boron. We ascribe the lower binding energy feature in the F 1s spectra of BF_3 treated samples to BF_3 that had intercalated into the crystal lattice. However, it is difficult to confidently deconvolve these two features without further studies. For frames A–C, we ascribe a feature at ~530 eV in the O 1s region to metallic oxides. The higher binding energy feature in each O 1s region is likely dominated by the surface hydroxyl groups, –OH, that reports assign as 532.9 eV for titanium hydroxide[30] but may contain trace contributions of adventitious, oxidized contaminants as well. While present in each sample's spectra, metal oxide contributions are larger in the ligand-adsorbed samples. One doublet describes well the Ti 2p region throughout all samples studied that we ascribe to Ti^{4+} with Ti $2p_{3/2}$ at ~459 eV and Ti $2p_{1/2}$

Table 2.2 XP Peak Area Ratios for Large-Grain Cs_2TiBr_6 vs Surface Treatment [a]

	Cs	Ti	Br
DCM-rinsed, sanded	0.5	1	2.1
BF_3-treated	0.4	1	0.06
$B(C_6F_5)_3$-treated	0.1	1	3.5

[a] Sensitivity-factor-corrected XP peak-area ratios are normalized to Ti ≡ 1 based on the Cs_2TiBr_6 Stoichiometry.

at ~465 eV. Both lattice and interfacial oxidized titanium likely contribute to the cumulative photoelectron signal and cannot be easily deconvolved for the similar 4+ oxidation state of each titanium species. Contributions to the C 1s regions in each frame include adventitiously adsorbed species at ~285 eV as well as features toward higher binding energy that would indicate oxidized adventitious contamination. High binding energy C 1s features in frame C may also be attributed to the phenyl rings of the $B(C_6F_5)_3$. Br 3d is well described in each representative spectrum by a singular d-orbital doublet with Br $3d_{5/2}$ at ~69 eV.

Beyond the position of each representative spectral feature, the relative change in intensities yields significant insight into each surface composition. Table 2.2 displays sensitivity-factor-corrected peak area ratios for each Cs_2TiBr_6 surface under study that we normalize to Ti ≡ 1 for its contribution to the overall material stoichiometry. Each value in Table 2.2 represents the peak area ratios of the representative spectra in Fig. 2.4. For sanded and DCM rinsed control samples as in Figure 2.4A the sensitivity-factor-corrected peak area ratios are far from the ideal bulk stoichiometry of 2:1:6 for Cs:Ti:Br. We further detail studies that examine the presence of surface metal oxides and their contributions to peak area ratios in the next chapter.

Figure 2.4 and Table 2.2 elucidate the effect of Lewis acid adsorption on interfacial atomic ratios. Relative to DCM rinsed and sanded control samples, the XP spectra of BF_3 treated Cs_2TiBr_6 surfaces as in Figure 2.4B and $B(C_6F_5)_3$ treated Cs_2TiBr_6 surfaces as in Figure 2.4C demonstrate a lower larger contribution of Cs. In the case of BF_3 treated surfaces bromine contributions were also significantly lowered, while the relative intensity of the Ti 2p and O 1s features was greater. This paired with evidence of multilayer adsorption in the F 1s feature of BF_3 treated surfaces suggests an increase in surface metal oxides following treatment, and potentially an attenuation of Cs and Br signal following Lewis acid adsorption in **Study 1**. However, it is difficult to deconvolve whether increased surface oxides or Lewis acid adsorption are to blame for attenuation of Cs and Br peak area ratios relative to Ti on BF_3 treated samples. In the case of $B(C_6F_5)_3$ treated samples from **Study 2**, while Cs contributions were lower, the Br peak area ratio increased relative to tita-

nium, resulting in a stoichiometry of 0.1:1:3.5 for Cs:Ti:Br. This stoichiometry is still incredibly far from the bulk stoichiometry of Cs_2TiBr_6.

The peak area ratios of both the Lewis acid adsorbed surfaces from the first two studies were far from the ideal bulk stoichiometry of 2:1:6 for Cs:Ti:Br. However, it is hard to deconvolve whether the attenuation of Cs (and in the case of BF_3 bromine signal) was a result of adsorption or just a result of increased surface oxides that were generated during surface treatments. With this in mind, **Study 3** aimed to elucidate the affects that surface adsorbed Lewis acids have on the surface chemistry of Cs_2TiBr_6.

Following confirmation of successful adsorption of $B(C_6F_5)_3$ by X-ray photoelectron spectroscopy, an air-exposure XRD elucidated the timescales of oxidation to investigate whether the formation of an interfacial Lewis adduct stabilized the surface against oxidation. Chapter 3 considers air stability XRD studies carried out on nascent powdered samples. XRD studies of ligand adsorbed surfaces were compared with nascent surfaces to elucidate the protecting nature of the ligand from oxidation, if any. Due to time constraints and instrumental limitations only one of the two ligands of interest was studied using this method. Due to the larger nature of the $B(C_6F_5)_3$ ligand, it was chosen for this study.

Figure 2.5 shows a comparison of nascent Cs_2TiBr_6 and $B(C_6F_5)_3$ treated samples that were exposed to air and scanned over a range of $2\theta = 28$–$30.5°$. Such a narrow scan range was chosen due to the close nature of the Cs_2TiBr_6(222) and the CsBr(110) reflections. In Chapter 3 we establish that crystalline CsBr and amorphous TiO_2 are oxidation products of Cs_2TiBr_6. Therefore, to compare the time scales of oxidation on ligand protected and nascent Cs_2TiBr_6 surfaces we chose a narrow scan range to allow for successive 10-min scans while still showing Cs_2TiBr_6 and a crystalline oxidation product.

Figure 2.5A demonstrates that within 1 min of exposure to ambient atmosphere, crystalline CsBr forms on nascent Cs_2TiBr_6 surfaces. Confirmed by the detectable CsBr(110) reflection within one minute. After 100 min, no detectable Cs_2TiBr_6(222) reflections remained, indicating full decomposition of the nascent powdered material. Frame B illustrates $B(C_6F_5)_3$ ligand adsorbed Cs_2TiBr_6 surfaces that were exposed to air for 100 minutes. While these traces contain considerably more background noise than the traces in frame A, the Cs_2TiBr_6(222) and CsBr(110) reflections are still visible within detection limits which allows for comparison. Similar to nascent samples, the CsBr(110) reflection is visible within 1 min of exposure to ambient air, suggesting that surface coverage of the $B(C_6F_5)_3$ ligand does not considerably attenuate oxidation upon initial air exposure. Similarly, after 100 minutes in air, the ligand-adsorbed surfaces had no detectable Cs_2TiBr_6(222) signal. This indicates that the timescale of oxidation in an air ambient of Cs_2TiBr_6 with multilayer coverage of $B(C_6F_5)_3$ is comparable to that of nascent samples.

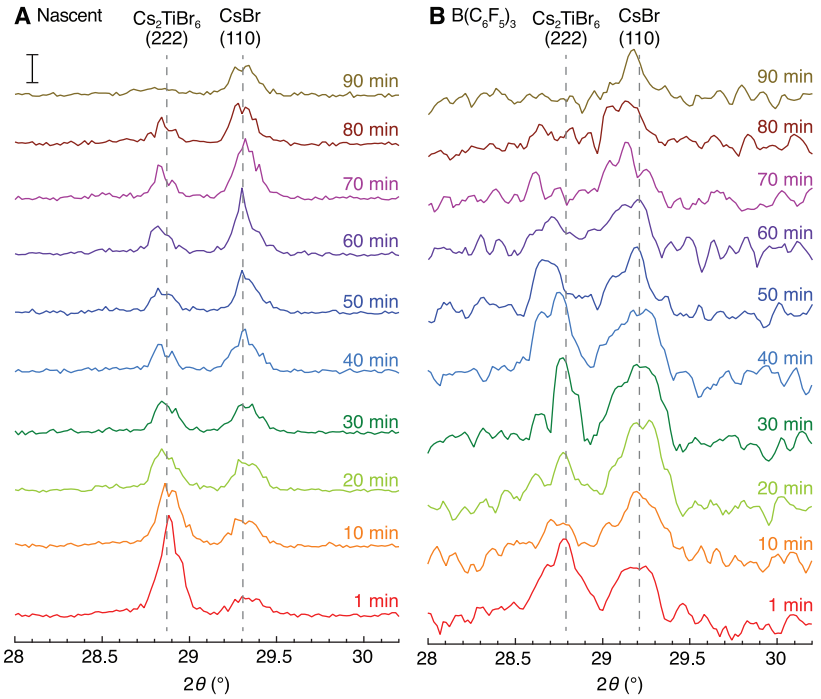

Figure 2.5 XRD traces of (**A**) nascent, and (**B**) $B(C_6F_5)_3$-treated Cs_2TiBr_6 following air exposure. From bottom to top, the traces in (**A**–**B**) show a decrease in the amplitude of the Cs_2TiBr_6(222) reflection and an increase in the amplitude of the CsBr(110) reflection.

2.3.4 Study 3: Ligand Adsorption to Oxide-Free Surfaces

The presence of metal oxides on both BF_3 etherate and $B(C_6F_5)_3$ Cs_2TiBr_6 samples, large relative intensities of F 1s signal indicating multilayer coverage,28 and even in the case of BF_3 treated surfaces a secondary F 1s feature at lower binding energy suggesting intercalation into the crystal lattice, indicated that further studies were necessary to elucidate the surface basicity of Cs_2TiBr_6. When considering additional surface basicity studies several changes were made to the approach to ensure data that was interpretable and unambiguous. A shorter reaction time to limit coverages to monolayers and prevent the formation of multilayers was employed. Exclusion of etherate from the BF_3 ligand by creating a BF_3·pyridine complex was also considered, as solvent stability studies suggested that ether reacts with Cs_2TiBr_6 surfaces to form surface oxides. Additionally, when addressing whether surface adsorbed ligands were adsorbing to Cs_2TiBr_6 or TiO_2 at the material's interface, aggressive steps were taken to ensure no surface metal oxides were present by cleaving samples in the reaction solution.

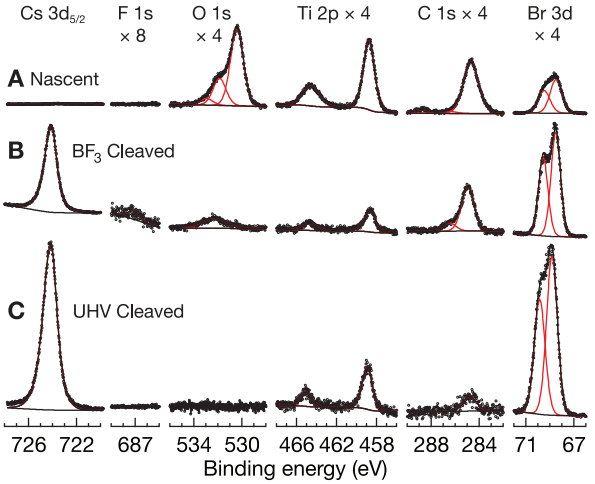

Figure 2.6 Representative XP spectra of (**A**) nascent, (**B**) cleaved in a BF_3 solution, and (**B**) UHV-cleaved samples. Nascent sample interfaces demonstrate no observable cesium but rather are dominated by titanium oxide. Oxide contributions as in the lower binding energy feature in the O 1s region best represent stoichiometric ratios with no observable oxide on UHV-cleaved surfaces (**C**). For BF_3 cleaved samples (**B**), an F 1s feature is visible, indicating successful adsorption of Lewis acids and signal in the O 1s region is only from adventitious contaminants and not metal oxides. The total *y*-axis amplitude of photoelectron counts is normalized between each frame with the O 1s, Ti 2p, C 1s, and Br 3d regions all magnified by 4× vs the Cs $3d_{5/2}$ region and the F 1s region magnified by 8× vs the Cs $3d_{5/2}$ region.

Figure 2.6 presents the representative Cs $3d_{5/2}$, F 1s, O 1s, Ti 2p, C 1s, and Br 3d X-ray photoelectron regions as a function of surface preparation. Preparations in Fig. 2.6 includes (A) a nascent sample, (B) a sample which was cleaved in a solution containing a BF_3·pyridine complex and allowed to react for 5 minutes, and (C) a UHV cleaved sample. UHV cleaving of Cs_2TiBr_6 is considered in more detail in Chapter 3. The nascent sample (Fig. 2.6A) was chosen as the "control" to illustrate surface oxides on samples that had not been processed in any way. The UHV cleaved sample (Fig. 2.6C) was chosen to demonstrate oxide-free Cs_2TiBr_6 surfaces with sensitivity-factor-corrected peak area ratios that are near the ideal stoichiometry of the material.

The representative spectra in frames B–C of Fig. 2.6 have characteristic Cs $3d_{5/2}$ features at ~723 eV that we attribute to lattice Cs^+. Interestingly, the nascent sample in frame A does not have any detectable Cs features, indicating that cleaving in a BF_3·pyridine complex solution and cleaving in UHV increase Cs signal. The absence of detectable F 1s signal in frames A and C indicates no surface fluorine species, as expected for nascent and UHV cleaved samples which have not been exposed to fluorine containing Lewis

Table 2.3 XP Peak Area Ratios for Large-Grain Cs_2TiBr_6 vs Surface Cleaving [a]

	Cs	Ti	Br
DCM-rinsed, sanded	*n/a*	1	0.9
Cleaved under BF_3 solution	3.8	1	8.6
UHV-cleaved	3.1	1	6.9

[a] Sensitivity-factor-corrected XP peak-area ratios are normalized to Ti ≡ 1

acids. Frame B contains a small F 1s feature at ~689 eV. The relative peak area of the F 1s feature on the BF_3 cleaved sample indicates less coverage than in the previously mentioned adsorption studies, largely due to the shorter reaction time. For frame A, we ascribe a feature at ~530 eV in the O 1s region to metallic oxides. This feature is not present in either of the cleaved samples, indicating successful removal of surface metal oxides. The higher binding energy feature in the O 1s regions of the nascent (Fig. 7A) and BF_3 cleaved (Fig. 7B) samples is likely dominated by the surface hydroxyl groups, –OH, that reports assign as 532.9 eV for titanium hydroxide[30] but may contain trace contributions of adventitious, oxidized contaminants as well. One doublet describes well the Ti 2p region throughout all samples studied that we ascribe to Ti^{4+} with Ti $2p_{3/2}$ at ~459 eV and Ti $2p_{1/2}$ at ~465 eV. Both lattice and interfacial oxidized titanium likely contribute to the cumulative photoelectron signal and cannot be easily deconvolved for the similar 4+ oxidation state of each titanium species. Contributions to the C 1s regions in each frame include adventitiously adsorbed species at ~285 eV as well as features toward higher binding energy that would indicate oxidized adventitious contamination. Br 3d is well described in each representative spectra by a singular d-orbital doublet with Br $3d_{5/2}$ at ~69 eV.

Beyond the position of each representative spectral feature, the relative change in intensities yields significant insight into each surface composition. Table 2.3 displays sensitivity-factor-corrected peak area ratios for each Cs_2TiBr_6 surface under study that we normalize to Ti ≡ 1 for its contribution to the overall material stoichiometry. Each value in Table 2.3 represents the peak area ratios of the representative spectra in Fig. 2.6. For nascent samples as in Figure 2.6A, the lack of observable cesium and a small bromine-to-titanium ratio further supports the dominance of interfacial titanium oxide. The sensitivity-factor-corrected Ti/Br peak area ratio was 1:0.9 for the spectra in Figure 2.6A. The large deviation from stoichiometric peak area ratios on nascent sample surfaces, in addition to the low Cs and Br contributions relative to Ti on ligand adsorbed surfaces from Study 1 and Study 2 (Table 2.2) suggests that TiO_2 dominates the chemistry of the surfaces.

Crystal cleavage to remove interfacial metal oxides prior to ligand adsorption was conducted to further elucidate the chemistry of surface adsorbed Lewis acids. Cleaving in the ultrahigh vacuum chamber enabled quantifications of Cs_2TiBr_6 surfaces with minimal opportunity to form interfacial oxides and act as a control for Cs_2TiBr_6 surfaces that have been cleaved in a reaction solution for Lewis acid adsorption. The representative vacuum-cleaved spectra in Figure 7C and the related peak area ratios in Table 2.3 reveal nearly ideal, stoichiometric interfaces. The average Cs/Ti/Br peak area ratios for UHV-cleaved Cs_2TiBr_6 found in Table 1 were 3.1:1:6.9. In addition to significantly improved atomic ratios, no features are visible in the O 1s region including a possible feature at ~530 eV due to metal oxides or at ~532 eV ascribed to adventitious oxygen.[31]

The near ideal, stoichiometric interfaces that are resultant of UHV cleaving (Fig. 2.6C) are fairly close to the peak area ratios seen in Table 2.3 for Cs_2TiBr_6 surfaces that had been cleaved in a BF_3 solution. In addition to this near ideal stoichiometry, Cs_2TiBr_6 surfaces cleaved in a BF_3 solution showed coverages of fluorine commensurate with approximately a monolayer of ligand and no surface oxides at ~530 eV attributable to metal oxides. This suggests that basic interfacial bromine adsorbs Lewis acids on oxide-free Cs_2TiBr_6 surfaces and provides an avenue for future studies.

2.4 Discussion

2.4.1 Cesium Titanium(IV) Bromide and Cesium Tin(IV) Bromide Synthesis Optimization and Stability

In our hands, we did not synthesize high quality Cs_2SnBr_6 and decided that it was not worth our time to perfect, given its high band-gap energy and the already promising energy conversion results of Cs_2TiBr_6. While Cs_2SnBr_6 did exhibit improved stability over Cs_2TiBr_6, we only consider Cs_2TiBr_6 herein.

The optimal conditions for Cs_2TiBr_6 synthesis included ~3 g total reactant loadings, a 10% stoichiometric excess of $TiBr_4$, a fiber quartz spacer to tilt the reaction ampoule, and temperature programs with a 15 h linear ramp to 680 and 710 °C, a 25 h soak at 680 and 710 °C, followed by a 96 h linear ramp to 0 °C in both zones.

Reactant loadings were chosen to produce large-grain crystals for the subsequent adsorption studies so that faceted crystals with large surface areas were available for easy handling and to easily fit the spot sizes of both XPS and XRD. These loadings could be changed to yield crystals of different sizes. However, given the long duration of the temperature programs required to yield high-quality material, higher stoichiometric quantities of the starting materials to yield larger crystals were chosen. In the event that a crystal was

too large, we cut in half in the glovebox using a razor blade, so the larger loadings were not an issue in tuning crystal size.

We suspect that during the high temperature melt synthesis the $TiBr_4$ vapor is mixing with liquid CsBr during the soak step. To further promote this mixing, we tried loadings with a stoichiometric excess of $TiBr_4$. This was chosen to encourage more collisions of $TiBr_4$ with the liquid CsBr. We found that an excess of $TiBr_4$ improved the quality and facets of the material, but the excess also resulted in shiny films of $TiBr_4$ that formed on the crystal surface during cooling. This was later addressed with an added step in the temperature program during cooling to getter $TiBr_4$ away from the cooling crystal, so that the excess could benefit crystallization during the "mixing" stage of the reaction but would not deposit on the surface during cooling. In our hands, this getter step was unsuccessful in drawing $TiBr_4$ away from the cooling Cs_2TiBr_6 crystals and merits further study.

Changes to the temperature programs had the greatest effect on quality of crystallinity and facet size, as demonstrated by Fig. 2.3. The temperature differential between the front end and the back end of the tube was chosen to encourage $TiBr_4$ vapor towards the cooler end, where the liquid CsBr was located. We chose the duration of the soak step to maximize mixing of the starting materials. Following the soak, a long cooldown of four days was employed. While such a long duration of cooling is not ideal in terms of expedited synthesis, this cooling was found to allow for the best nucleation. The nucleation occurs during cooling, as we established that Cs_2TiBr_6 is a liquid at soak temperatures, and therefore, better nucleation resulting in larger facets requires longer cooling times. While it is not presently clear whether nucleation occurs during a specific temperature range of the cooling step, this information could be leveraged to shorten the duration of cooling.

In addition to finding the ideal conditions for Cs_2TiBr_6 synthesis, we established stability in several solvents. We found four solvents in which the crystals had no color change or dissolution. These solvents can be found in Table 2.1. The resulting samples were scanned in XPS to confirm that the solvents had no effect on the surface chemistry. However, we did not include solvent stability XPS in this chapter. As we gained more knowledge about the stability of Cs_2TiBr_6 surfaces and found that oxides readily form at the surface, it became too difficult to deconvolve whether oxide products at the Cs_2TiBr_6 surface following rinsing were due to the solvent used or due to small amounts of oxygen in the flush box. Given that this information was unclear, further studies would be necessary to truly elucidate the stability of Cs_2TiBr_6 in particular solvents, though this information might not be necessary for physiochemical polishing, solvent exchange reactions, and photoelectrochemistry.

2.4.2 Ligand Adsorption and Surface Oxides

We adsorbed Lewis acids to both oxide rich Cs_2TiBr_6 surfaces (**Study 1** and **Study 2**), and oxide-free surfaces (**Study 3**). We aimed for monolayer coverages of these Lewis acids to Cs_2TiBr_6 surfaces in order to establish the surface basicity of interfacial bromine. **Study 1** and **Study 2** employed 1-h reactions at room temperature while **Study 3** employed a much shorter 5-min reaction. XPS revealed that the long reactions in **Studies 1–2** were unnecessary as they resulted in multilayer coverage, which is demonstrated by the intensity of F 1s signal.[28]

Interestingly, the presence of an F 1s doublet seen on BF_3·etherate-adsorbed surfaces that were treated for 1-hour at room temperature suggests adsorption of BF_3 to species other than bromine on the surface. It is presently unclear whether the second F 1s feature at a lower binding energy is caused by BF_3 that had intercalated into the Cs_2TiBr_6 bulk, or whether the ligands were adsorbed to TiO_2 on surface. However, the oxide on surface is expected to be porous and not self-passivating. Therefore, BF_3 could be intercalating past the TiO_2 layer into the Cs_2TiBr_6 bulk. Given how many unknowns are associated with this second F 1s feature we recommend DFT be conducted to establish where these ligand species would end up, as this merits further study. We believe that this doublet is a result of the long duration of the reaction, as it is not present in XP spectra of the BF_3 cleaved surfaces from Study 3 that were only reacted for five minutes.

In addition to the confirmation of adsorption by F 1s signals in the XP spectra of each respective Lewis acid treated surface (Fig. 2.4 and Fig. 2.6), we also observed metal oxides on surfaces of treatments undertaken for **Studies 1–2**. The presence of metal oxides were expected, as DCM rinsing and sanding does not fully remove surface metal oxides. However, the ~530 eV oxygen feature that we attribute to metal oxides grew in intensity following ligand adsorption in the case of the first two studies. Initially we believed that the ether was the culprit of such oxidation, however, oxides were still present on surfaces that had been reacted with $B(C_6F_5)_3$, a Lewis acid that was not complexed with a solvent. After the cleaving experiments undertaken in Chapter 3 it is difficult to deconvolve oxides that are a result of surface processing and oxides that are due to reaction with the ether that the BF_3 solution was stored in.

With that in mind, in order to fully remove oxides, we created a BF_3 pyridine complex to exclude ether and also cleaved the Cs_2TiBr_6 sample in the reaction solution to remove any opportunity for oxides to form in **Study 3**. This resulted in monolayer coverages and no oxide features at ~530 eV. This confirms that BF_3 that has been adsorbed to basic interfacial halogens does appear in XPS at ~689 eV. This does not add additional clarity to the origin of the lower binding energy feature in the F 1s spectra of BF_3 etherate

treated samples. However, **Study 3** presents a route forward for future ligand adsorption studies on oxide-free surfaces.

2.4.3 Ligand Adsorption and Transient Stability

Multilayer coverage of *tris*(pentafluorophenyl)borane on Cs_2TiBr_6 surfaces did not improve or have an effect on ambient atmospheric stability. Figure 5B demonstrates that within minutes of exposure to air $B(C_6F_5)_3$ treated surfaces oxidized to form crystalline CsBr. This is consistent with other ambient stability studies on nascent samples. While the three studies prove that ligand adsorption is possible at basic halides on the Cs_2TiBr_6 surface, $B(C_6F_5)_3$ did not improve transient stability, and other materials may be necessary for passivation. We believe that ligand adsorption would have great use as a soft organic contact to align mismatched silicon and Cs_2TiBr_6 lattices in a tandem junction PV configuration, however, Lewis acid adsorption does not seem to be the route for passivation.[28,32] Instead, we believe that TiO_2, whose band edge positions are well aligned for electron transport with Cs_2TiBr_6, would be an ideal passivation material.[58] We explore TiO_2 passivation of Cs_2TiBr_6 surfaces in more depth in Chapters 4 and 5.

2.5 Conclusions and Future Work

We found that optimal Cs_2TiBr_6 synthesis parameters for high temperature melt include a 10% stoichiometric excess of purified $TiBr_4$ with CsBr. Temperature program optimization included a tramp = 15 h, with soak temperatures of $T_{soak,\,front}$ = 680 °C and $T_{soak,\,back}$ = 710 °C, for a 25 h soak followed by a 96 h linear ramp in both zones. We also established that Lewis acids readily ligate to Cs_2TiBr_6 surfaces and in cases of long exposure can form multilayer coverages confirmed by XPS. The basicity of interfacial halides at the Cs_2TiBr_6 provides a potential route for future passivation efforts and a greater understanding of interfacial chemical states that would be accessible to ligand exchange. However, adsorption of $B(C_6F_5)_3$ to Cs_2TiBr_6 surfaces did not improve the stability of the surfaces in an air ambient as demonstrated by XRD, which indicates that different stabilizing ligands may be necessary for future passivation efforts.

In addition to preliminary information about the surface basicity of interfacial bromine, efforts to explore adsorption of Lewis acids to oxide-free Cs_2TiBr_6 surfaces were undertaken. We found that Lewis acids adsorb to interfacial bromine on oxide-free Cs_2TiBr_6, as confirmed by XPS and exhibit peak area ratios much closer to the ideal bulk stoichiometry of the material, compared to ligands adsorbed to metal oxide rich Cs_2TiBr_6 surfaces. In addition, ligand adsorption to oxide-free Cs_2TiBr_6 surfaces confirmed that adsorption likely occurs at basic interfacial halides.

Given the preliminary information gained through the undertaken surface basicity studies, many future studies are necessary to gain a broader understanding of the surface chemistry of large-grain Cs_2TiBr_6. These studies were mostly done on Cs_2TiBr_6 surfaces that were rich in metal oxides, the following chapter explores oxide-free surfaces in depth. In addition, we consider thin film Cs_2TiBr_6 in further detail in Chapter 5, but to summarize, thin films show moderately improved transient stability. Therefore, we believe undertaking surface basicity studies on Cs_2TiBr_6 thin films, rather than large-grain material, we will be able to gather more information about the effects of ligand adsorption on ambient stability and more importantly charge transport in device relevant materials. Further fundamental surface chemistry experiments to elucidate the chemical species available at the Cs_2TiBr_6 surface for ligation could give insight into what can be bound to the surface for future passivation efforts, soft contacts to silicon, and charge transport in device relevant studies. In addition to further surface basicity studies, cation exchange offers a potential route to study the reactivity of surface cations such as Cs^+.

Another potential route for future work includes elucidating more information about surface bound ligands. While these preliminary fundamental surface chemistry studies did not include anything about binding strengths, future studies may consider doing temperature programmed desorption (TPD) to study the binding energies of surface adsorbed ligands. These results hold promise for potential application in tandem-junction PV but present additional questions about the stability of the material and potential routes for further passivation that merits further study.

CHAPTER 3

INTERFACIAL STATES, ENERGETICS, AND ATMOSPHERIC STABILITY OF LARGE-GRAIN ANTIFLUORITE CESIUM TITANIUM(IV) BROMIDE

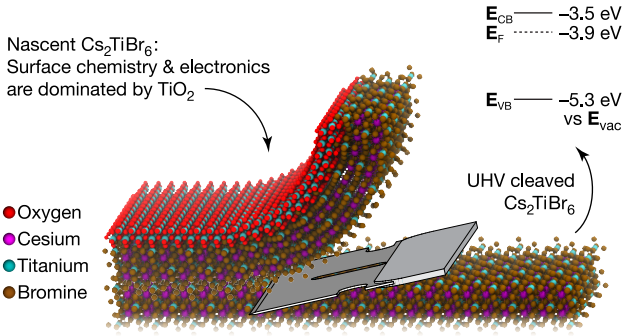

Portions adapted from:

Mendes, J.L.; Gao, W.; Martin, J.L.; Carl, A.D.; Deskins, N.A.; Granados-Focil, S.; Grimm, R.L. Interfacial States, Energetics, and Atmospheric Stability of Large-Grain Antifluorite Cs_2TiBr_6. *J. Phys. Chem. C*, **2020**, *124*, 24289–24297.

Special thanks to Prof. Granados-Focil of Clark University for collecting SEM data, and to Prof. Deskins in Chemical Engineering for the computational chemistry.

Abstract

Recent reports post conflicting results on the atmospheric stability of Cs_2TiBr_6, a non-toxic, Earth-abundant solar energy conversion material. Here, a high-temperature melt of CsBr and $TiBr_4$ yielded large-grain samples with >1 mm^2 facets as verified by optical microscopy and SEM. With the properties of pristine material of particular interest, we investigated a series of physiochemical surface treatments including rinsing, abrasion, and cleaving in ultrahigh vacuum (UHV). For each surface treatment, X-ray photoelectron spectroscopy (XPS) quantified surface chemical species while ultraviolet photoelectron spectroscopy (UPS) established valence band structure as a function of surface treatment. Amorphous titanium oxide with crystalline cesium bromide dominate the surfaces of nascent Cs_2TiBr_6 material. UHV cleaving yielded oxide-free surfaces with excellent alignment between valence band structure and a DFT-calculated density of states, a 3.92 eV work function, and 1.42 eV Fermi energy vs the valence band maximum. Band energetics are commensurate with moderate n-type doping for this melt-synthesized large-grain Cs_2TiBr_6. Titanium oxide once again dominates UHV-cleaved samples following a ten-minute exposure to an air ambient. We discuss the implications of these surface chemical and electronic results for photovoltaics.

3.1 Introduction

Solar photovoltaic (PV) devices are a leading global renewable energy source and their energy conversion efficiency and cost-per-watt have experienced consistent improvements since their inception.[33–34] Present PV devices that dominate solar energy markets are single-junction, silicon-based devices, but such designs are approaching their thermodynamic and practical efficiency limits.[35–36] To overcome the efficiency limits of single-junction devices, tandem-junction PV configurations may enable continued gains both in efficiency and in cost-per-watt metrics. Apart from highly efficient but expensive III–V-based devices, tandem-junction PV research has recently focused on combinations of dissimilar materials in which silicon forms the low-band-gap bottom absorber.

Among top-absorber candidates for tandem junction PV devices, halide perovskite semiconductors have gained interest to address current global energy needs.[37] Lead- and tin-based halide perovskites are particularly compelling for their low expense for fabrication, defect tolerance, and earth abundance, and favorable band gap energies both for single-absorber and tandem-junction PV applications.[13,38–41] Devices with these materials have seen power conversion efficiencies exceed 23%.[12] However, toxicity and stability concerns exist for Pb^{2+}- and Sn^{2+}-based halide perovskite semiconductors, which drives research into alternative materials with promising energy-conversion performance but lower toxicity.[14–15,42]

Considering the potential perovskite alternatives, cesium titanium bromide, Cs_2TiBr_6 emerged as a candidate for solar energy conversion applications.[24,43] Unlike perovskites of an ABX_3 stoichiometry with A^{n+} cations at the unit cell corners, B^{2n+} cations in the unit cell body center, and X^{n-} anions at the unit cell faces, Cs_2TiBr_6 follows a different structure. Similarly to the more common potassium hexachloroplatinate, K_2PtCl_6, Cs_2TiBr_6 closely resembles an anti-fluorite, Na_2O, structure in which polyatomic anions of $(TiBr_6)^{2-}$ octahedra occupy each unit cell corner and face while Cs^+ cations fill all eight available tetrahedral holes. Cs_2TiBr_6 is attractive for its earth abundance, non-toxic components, and recent reports of promising power conversion efficiencies.[24] The ~1.8 eV band gap positions Cs_2TiBr_6 as a candidate top absorber to pair with silicon in tandem PV configurations.[25] Despite these promising PV results for Cs_2TiBr_6, much remains unknown about the chemical properties, carrier dynamics, and interfacial stability of the material. Recent reports on powdered material Cs_2TiBr_6 imply rapid decomposition in an air ambient in contrast to early device reports of good atmospheric stability.[24,44] The diverging nature of atmospheric stability results motivates investigations into the interfacial stability and electronic structure of large-grain, high-quality Cs_2TiBr_6 material.

Herein, we synthesize large-grain Cs_2TiBr_6 from a high-temperature, in vacuo melt, and characterize surface species and electronic structure as a function of surface treatments. We explore multiple physiochemical cleaning treatments to establish the properties of nascent surfaces, pristine surfaces, and the efficacy of each cleaning method to elucidate the physical basis of the contrasting reports. The *in vacuo* high-temperature melt employs a multi-day cooling of a stochiometric excess of $TiBr_4$ with CsBr that yields samples with visible facets in excess of 1 mm^2. Surface preparations for chemical and electronic analyses include nascent surfaces, those subjected to physical abrasion, sequential chemical polishing and physical abrasion, and cleaving under ultrahigh vacuum (UHV). Chemical polishing employs dichloromethane for its ability to orthogonally dissolve $TiBr_4$ while negligibly dissolving Cs_2TiBr_6. Photoelectron spectroscopies quantify chemical and electronic structure as a function of surface preparation. X-ray photoelectron spectroscopy (XPS) ascertains chemical states and relative stoichiometries of near-interfacial species. Ultraviolet photoelectron spectroscopy (UPS) establishes work function and Fermi energy values as well as the density of states near the valence band edge. Density-functional theory (DFT) calculations collaborate electronic structure and the density of states established with the UPS data. Further, X-ray diffraction (XRD) validates successful syntheses and establishes the atmospheric stability of this large-grain Cs_2TiBr_6 material. With these studies we aim to elucidate the effects of interfacial chemical states and atmospheric stability on the electronic properties of this solar-relevant material.

3.2 Experimental Section

Appendix A details in full the materials and chemicals, experimental methods, and analyses employed. Here we present each in brief.

Inert environments for sample synthesis, processing, reactions, and storage included a Schlenk line, a nitrogen-purged recirculating glovebox with an active catalyst to maintain oxygen concentrations below 1 ppm, and a flush box with an oxygen concentration below 5 ppt (thousand), as measured at a commercial oxygen sensor.

Large-grain Cs_2TiBr_6 was synthesized via high-temperature melt in evacuated, sealed quartz ampoules from a 10% stoichiometric excess of purified $TiBr_4$ with CsBr. Under a typical growth condition, ampoules in a two-zone tube furnace underwent a 15 h linear ramp to 680 °C and 710 °C, a 25 h soak at 680 °C and 710 °C, followed by a 96 h linear ramp to 0 °C in both zones.

The resulting large-grain material was subjected to surface processing techniques to remove surface contaminants with physical characterization to establish the efficacy of each process as compared to nascent material. Processing techniques included physical abrasion, a dichloromethane (DCM) rinse followed by physical abrasion, *in vacuo* cleaving. All surface processing was employed in inert environments. In related experiments, exposure to an air ambient following UHV cleaving established the nature of oxidation on otherwise pristine surfaces.

A PHI 5600 multitechnique system acquired all X-ray and ultraviolet photoelectron spectra as described previously.[28–29,45–46] The apparent rapid oxidation of the material necessitated a vacuum suitcase (Transfer Engineering and Manufacturing, Inc., Fremont, CA) for air-free transfer of puck-mounted Cs_2TiBr_6 samples from a recirculating glovebox to the instrument. Peak quantification utilized an in-house-developed LabVIEW program based on published spectral shapes and corrected for instrument specific sensitivity factors,[31,47] and background energy loss functions.[48–50] For ultraviolet photoelectron spectroscopy, a gas discharge lamp (UVS 40A2, Prevac, Rogów, Poland) generated the He I spectroscopic line, $\mathbf{E}_{\mathrm{He\,I}} = h\nu = 21.218$ eV. We report sample work function values, ϕ, as the difference between $\mathbf{E}_{\mathrm{He\,I}}$ and the secondary electron cutoff energy, or $\phi = \mathbf{E}_{\mathrm{He\,I}} - \mathbf{E}_{\mathrm{SEC}}$. We report Fermi level energies relative to valence band maximum energies, or $\mathbf{E}_{\mathrm{F}} - \mathbf{E}_{\mathrm{VBM}}$. Density functional theory (DFT) calculations in the Vienna *Ab Initio* Simulation Package (VASP)[51–54] modeled a Cs_2TiBr_6 bulk cell[25] to reveal valence band electronic structure to compare to the UPS-derived results.

A Bruker-AXS D8 focus powder X-ray diffractometer with Cu Kα_1 radiation collected X-ray diffraction (XRD) data in the range of $2\theta = 10-45°$ on samples mounted in the flush box and isolated from air with low-static Kapton. For studies of the evolution of XRD trace features as a function of air exposure,

the Kapton tape was removed for sample exposure to an air ambient. Air exposure utilized two distinct protocols. In one protocol for full $10-45^\circ$ trace acquisitions, either 10- or 100-min air exposures were followed by transfer back into the recirculating glovebox and resealing under Kapton prior to data collection. In a separate protocol, Kapton tape was removed and a sample was successively and repetitively scanned in 10-min intervals at $2\theta = 28 - 30.5^\circ$ to establish a time evolution of oxidation.

A UV-Visible spectrometer (Evolution 300, Thermo Fisher Scientific, Waltham, MA) collected scattered light from Cs_2TiBr_6 samples mounted in a Praying Mantis diffuse reflection accessory (Harrick Scientific Products, Pleasantville, NY) and isolated from the air ambient with Kapton tape.

At Clark University, a Tescan Analytics Vega3 (Tescan Orsay Holding, A.S., Brno-Kohoutovice, Czechia) scanning electron microscope with a tungsten cathode operating at a 10 kV acceleration potential and a secondary electron detector acquired the images in Fig. 3.1B–C. A Hitachi TM3000 TableTop SEM (Hitachi High-Tech America, Inc., Schaumburg, Illinois) operating with a 15 kV acceleration potential, a four-segment backscatter electron detector, and a silicon drift detector enabled EDX analyses yielded the images in Fig. 3.1D–E. Samples for SEM and EDX analyses were prepared in the recirculating glovebox and transported to the instruments in sealed vials with rapid transfer for SEM analyses.

3.3 Results

3.3.1 Imaging

As synthesized from a high-temperature melt and a long cooling period, crystals appeared red-black to black with red fringing along thin edges. Extrapolations in Fig. A.2 respectively indicate indirect and direct forbidden energy gaps of 1.76 and 1.86 eV for the dark-red, large-grain Cs_2TiBr_6 material under study. This agrees well with early reports of 1.8 eV band gaps for thin film Cs_2TiBr_6,[24–25] and somewhat lower as compared to the 1.9 eV indirect and 2.0 eV direct band gaps from recent powder studies.[44] All UV-Vis data collection utilized samples that were isolated from an air ambient by Kapton tape. Qualitatively, within minutes following exposure to ambient air, samples become wet and begin to lighten in color, indicating the material is hygroscopic and reactive in air.

Optical images, as in Fig. 3.1A, demonstrated crystal facets with ~1 mm^2 areas. Representative SEM images as in Fig. 3.1B–C reveal similar large-grain facets both for nascent samples as in frame B and for a sample that was cleaved in a recirculating glovebox, transported in a sealed container, and expeditiously transferred to the SEM in air in frame C. The cleaved Cs_2TiBr_6 sample in the EDX analyses experienced minimal air exposures of <1 min

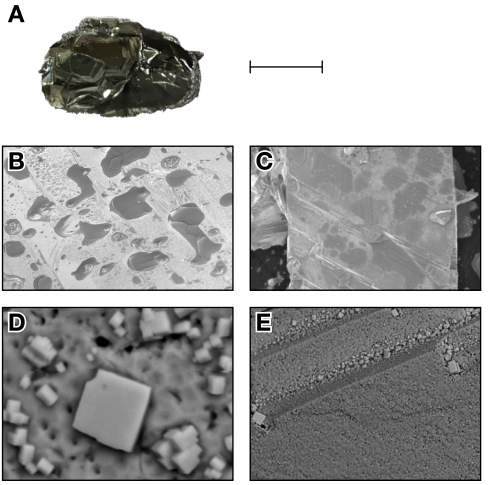

Figure 3.1 Optical image (**A**) of a nascent, large-grain Cs_2TiBr_6 sample reveals large-grain facets in excess of 1 mm^2. Frames (**B**)–(**E**) present SEM images of a (**B**) nascent sample, and (**C**)–(**E**) samples that were freshly cleaved prior to introduction to the SEM with <1 min of air exposure. EDX analysis of the zoomed-in cuboid feature in frame (**C**) reveals atomic ratios of 17.0% Cs, 25.0% Br, 39.6% C, and 18.4% O that suggest a cesium bromide crystal with adventitious contaminants. In contrast to (**D**), a wider-area EDX analysis for frame (**E**) demonstrates atomic ratios of 13.8% Cs, 6.1% Ti, 33.5% Br, 37.1% C, and 9.5% O indicating a distribution that better represents the Cs_2TiBr_6 stoichiometry. The scale bar represents 1 cm for frame (**A**), 200 μm for frames (**B**) and (**C**), 5 μm for frame (**D**), and 30 μm for frame (**E**).[26]

during sample transfer, Fig. 3.1D. Even with of <1 min in an air ambient, high-magnification images (left) revealed micron-sized cubic grains attributable to CsBr based on EDX analyses. Wide-area regions (right) demonstrated EDX-determined Cs:Ti:Br ratios of 2.2:1:5.5, which is a good qualitative match to the bulk Cs_2TiBr_6 stoichiometry. While CsBr is an initial reactant, recent reports demonstrate that CsBr is also an oxidative byproduct[44] whose presence is not unambiguously established by the SEM results. This motivates further investigations into the chemical transformations at Cs_2TiBr_6 surfaces.

3.3.2 Ambient Atmospheric Stability of Cs_2TiBr_6

XRD further validated the presence of Cs_2TiBr_6 and established its oxidative stability. Figure 3.2 presents representative wide-area XRD traces for an individual nascent Cs_2TiBr_6 in frame A prior to exposure to air, following 10 min of ambient air exposure in frame B, and following 100 min of air exposure in frame C. As XRD acquisition timescales are commensurate with the desired air exposure times, air exposure occurred offline from data

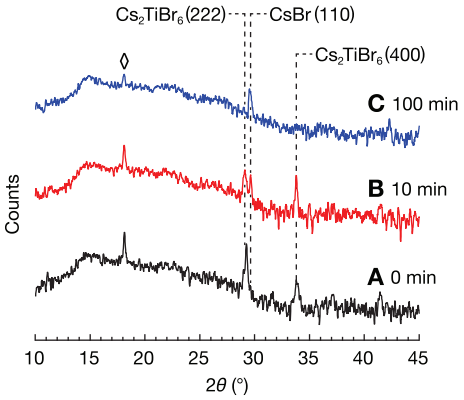

Figure 3.2 Representative XRD traces for Cs_2TiBr_6 samples as a function of air exposure and otherwise isolated from air by Kapton tape during analysis. Cs_2TiBr_6(222) reflections and substrate features, ◇, dominate samples with no air exposure as in (**A**). For (**B**) 10 min and (**C**) 100 min exposures to an air ambient contributions from the Cs_2TiBr_6(222) reflection at 28.9° diminishes in favor of a feature at 29.4° attributed to CsBr(110) reflections.[26] ©2020 American Chemical Society

acquisition with a re-introduction to an inert atmosphere and Kapton sealing prior to subsequent scans. All traces in Fig. 3.2 demonstrate substrate reflections with a diamond annotation, ◇. The nascent sample trace in Fig. 3.2A contains two dominant features, at ~28.9° and ~33.8° which correspond to the Cs_2TiBr_6(222) and (400) reflections, respectively. Following 10 min of air exposure, Fig. 3.2B demonstrates an additional feature at ~29.4° that is adjacent to the Cs_2TiBr_6(222) reflection. The position of the new feature corresponds to the CsBr(110) reflection, indicating a degradation of the large-grain Cs_2TiBr_6 due to its interaction with air as observed for powdered material.[44] As seen in Fig. 3.2C, a longer, 100 min air exposure yields the complete loss of XRD-observable Cs_2TiBr_6 features with only a CsBr(110) reflection feature. Visually, after 100 min in air, the sample was wet and significantly lighter in color. Of particular note, the traces for air-exposed Cs_2TiBr_6 demonstrate no noticeable feature ascribable to crystalline oxides.

The close spacing between the Cs_2TiBr_6(222) and CsBr(110) reflection features at ~28.9° and ~29.4°, respectively, affords a narrow scan window to ascertain the time-evolution of reactivity in air. Figure 3.3A stacks repeated diffraction traces for a single, representative Cs_2TiBr_6 sample as a function of air exposure time. A CsBr(110) reflection feature appears following 1 min of air exposure, indicating that a reaction occurs quite rapidly upon exposure to an air ambient. Throughout a prolonged air exposure, the CsBr(110) reflection steadily increases in area while the adjacent Cs_2TiBr_6(222) reflection decreases

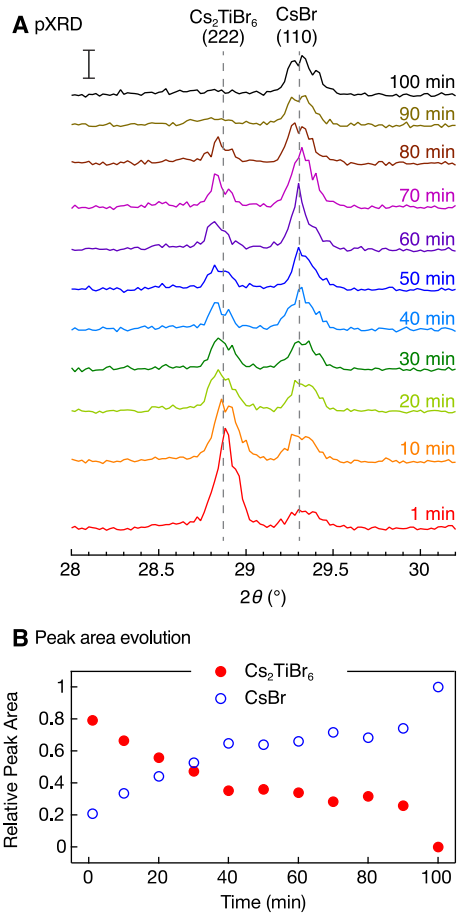

Figure 3.3 XRD traces of (**A**) Cs_2TiBr_6 following air exposure. From bottom to top, the traces in (**A**) show a decrease in the amplitude of the Cs_2TiBr_6(222) reflection and an increase in the amplitude of the CsBr(110) reflection. A plot of relative peak area vs time (**B**) demonstrates the decomposition of the Cs_2TiBr_6 to products including CsBr.[26] ©2020 American Chemical Society

in area. At 90–100 min, XRD traces demonstrate no observable reflections that are ascribable to Cs_2TiBr_6(222).

To gain further insight into the time-evolution of Cs_2TiBr_6 degradation in air, Fig. 3.3B demonstrates fitted peak areas of both the Cs_2TiBr_6(222) and the CsBr(110) reflections vs air exposure time that are normalized to the total peak area at each time. Upon exposure to air, Cs_2TiBr_6 degrades rapidly, as characterized by the sharp negative slope of the relative Cs_2TiBr_6(222) peak area. Figure 3.3B quantitatively demonstrates the trend in decreasing

Cs_2TiBr_6 and increasing CsBr throughout the air exposure duration. While the fitted ratios at 80 and 90 min may imply a decreased rate of oxidation, we attribute those data to errors associated with fitting small-area features in the Cs_2TiBr_6(222).

3.3.3 Chemical Speciation of Cs_2TiBr_6 Surfaces

While the XRD results demonstrate a rapid reaction of large-grain Cs_2TiBr_6 upon air exposure, the only observed crystalline product is cesium bromine with no ascribable oxide features. Photoelectron spectra reveal such interfacial chemistry.

Figure 3.4 presents representative Cs $3d_{5/2}$, O 1s, Ti 2p, C 1s, and Br 3d X-ray photoelectron regions as a function of surface preparations. Preparations in Fig. 3.4 include (A) nascent, (B) sanded, (C) DCM rinsed and then sanded, (D) UHV cleaved, and (E) exposed to air for ten minutes following a UHV cleaving. As discussed below, we particularly chose rinsing to precede sanding to remove any leftover $TiBr_4$ that may have condensed on the crystal during the synthesis cooling. We additionally considered samples following a DCM rinse only, however those samples demonstrated spectra that strongly resembled those of nascent surfaces and will not be considered further. Figure 3.4 normalizes spectra between frames based on the cumulative area of all presented features. The cesium region of the spectrum demonstrated a singular feature in frames B–E at ~723 eV that we ascribe to lattice Cs^+. Interestingly, the nascent sample in frame A demonstrated no observable interfacial cesium within detection limits. For frames A–C and E, we ascribe a blue-shaded feature at ~530 eV in the O 1s region to metallic oxides. The green-shaded feature in each O 1s region are likely dominated by surface hydroxyl groups, –OH, that reports assign as 532.9 eV for titanium hydroxide,[30] but may contain trace contributions of adventitious, oxidized contaminants as well. One doublet describes well the Ti 2p region throughout all samples studied that we ascribe to Ti^{4+} with Ti $2p_{3/2}$ at ~459 eV and Ti $2p_{1/2}$ at ~465 eV. Both lattice and interfacial oxidized titanium likely contribute to the cumulative photoelectron signal and cannot be easily deconvolved for the similar 4+ oxidation state of each titanium species. Contributions to the C 1s region include adventitiously adsorbed species at ~285 eV as well as features towards higher binding energy that would indicate oxidized adventitious contamination. Br 3d is well described by a singular d-orbital doublet with Br $3d_{5/2}$ at ~69 eV. Of value in elucidating the nature of the oxides, scans to higher binding energies revealed no features that would indicate the presence of BrO_x^- species including hypobromite through perbromate. The absence of detectable bromine oxides and a lack of oxidation pathways for Cs^+ suggests that interfacial titanium oxides yield the observed metal-associated O 1s features.

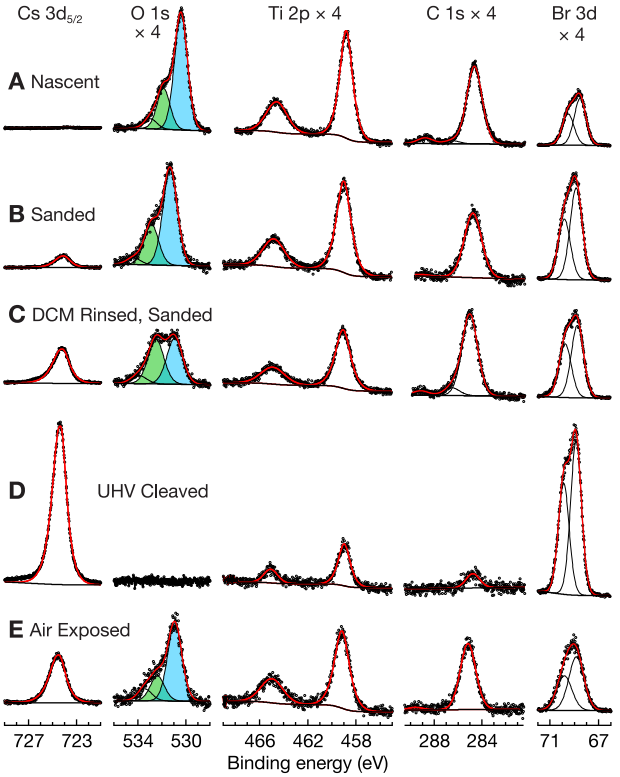

Figure 3.4 Representative XP Spectra of (**A**) nascent, (**B**) sanded, (**C**) DCM rinsed and sanded, (**D**) UHV cleaved, and (**E**) UHV-cleaved sample following a subsequent ten-minute exposure to air. Nascent sample interfaces demonstrate no observable cesium but rather are dominated by titanium oxide. Oxide contributions noted by the blue-shaded feature in the O 1s region decrease with physiochemical processing (**B**,**C**) and best represent stoichiometric ratios with no observable oxide on UHV-cleaved surfaces (**D**). For UHV-cleaved samples subsequently subjected to 10 min in air (**E**), oxide features return with a concomitant suppression of Cs and Br contributions. The total *y*-axis amplitude of photoelectron counts is normalized between each frame with the O 1s, Ti 2p, Cs 1d, and Br 3d regions all magnified by 4× vs the Cs $3d_{5/2}$ region.[26]

Beyond the position of each spectral feature, the relative change in intensities yields significant insight into each surface composition. Table 3.1 displays sensitivity-factor-corrected peak area ratios for each Cs_2TiBr_6 surface under study that we normalize to Ti ≡ 1 for its contribution to the overall material stoichiometry. Each value in Table 3.1 represents averages and standard deviations for a minimum of four samples. For nascent samples as in Fig. 3.4A, the lack of observable cesium and a small bromine-to-titanium ratio further supports the dominance of interfacial titanium oxide. Sensitivity-

Table 3.1 Sensitivity-factor-corrected XP peak area ratios for large-grain Cs_2TiBr_6 samples as a function of surface treatment that we normalize to titanium based on the Cs_2TiBr_6 stoichiometry [a]

	Cs	Ti	Br
Nascent	*n/a*	1	1.4 ± 0.7
Sanded	0.8 ± 0.6	1	3.1 ± 0.8
DCM Rinsed, Sanded	0.5 ± 0.3	1	2.1 ± 0.8
UHV Cleaved	3.1 ± 0.7	1	6.9 ± 0.1
Air Exposed	1.2 ± 0.6	1	1.9 ± 0.4

[a] Nascent, sanded, DCM rinsed and sanded, and UHV-cleaved-then-air-exposed samples demonstrate significantly suppressed interfacial concentrations of both cesium and bromine, relative to the anticipated 2:1:6 stoichiometry. Although not a perfect match, the UHV-cleaved sample demonstrates relative ratios that best align with the anticipated stoichiometry. Data are presented as average ± standard deviation values for at least four samples each.

factor-corrected Ti:Br ratio averages for nascent samples were 1:1.4 ± 0.7 and specifically 1:0.9 for the spectra in Fig. 3.4A. The large deviation from stoichiometric ratios on nascent sample surfaces motivated the physiochemical cleaning methods under study.

Figure 3.4 and Table 3.1 elucidate the effect of physiochemical treatments on interfacial atomic ratios. Relative to nascent samples, XP spectra of sanded Cs_2TiBr_6 surfaces as in Fig. 3.4B and sequentially DCM-rinsed-and-sanded surfaces as in Fig. 3.4C demonstrate a larger relative contribution from cesium and bromine and a concomitant reduction in interfacial titanium oxides. However, the Cs:Ti:Br ratios both for sanded and for DCM rinsed and sanded surfaces reveal interfacial cesium and bromine quantities that remain well short of the bulk 2:1:6 stoichiometry. Based upon the peak area ratios in Table 3.1, the chemical and physical polishing considered in the present study are not effective in fully removing surface contaminants that are dominated by titanium oxide.

Crystal cleavage in the ultrahigh vacuum chamber enabled quantifications of Cs_2TiBr_6 surfaces with minimal opportunity to form interfacial oxides. The representative vacuum-cleaved spectra in Fig. 3.4D and the related peak area ratios for several samples in Table 1 reveal nearly ideal, stoichiometric interfaces. The average Cs:Ti:Br peak area ratios for UHV cleaved Cs_2TiBr_6 found in Table 3.1 were $3.1 \pm 0.7 : 1 : 6.9 \pm 1.1$. The experimentally derived ratios somewhat overrepresent interfacial cesium and bromine relative to the ideal 2:1:6 stoichiometric ratio for Cs:Ti:Br, but best represent the bulk atomic ratios as compared to other cleaning methods. In addition to significantly improved atomic ratios, no features are visible in the O 1s region including a possible feature at ~530 eV due to metal oxides or at ~532 eV ascribed to

adventitious oxygen.[31] A nominal quantity of observable C 1s exists on the UHV cleaving that we attribute to the ~20 min timescale between cleaving and complete data analysis.

Following scanning of "clean" UHV-cleaved Cs_2TiBr_6 surfaces, we explored changes to interfacial stoichiometry due to a brief exposure to an air ambient. Following UHV cleaving and photoelectron spectroscopy, samples were re-scanned following a ten-minute exposure to the ambient atmosphere. The representative spectra in Fig. 3.4E reveal an increase in surface metal oxide at ~530 eV as well as adventitious C 1s and O 1s features after ten minutes of ambient air exposure relative to the UHV-cleaved spectrum in Fig. 3.4D. Both the areas in Fig. 3.4E and the ratios in Table 3.1 demonstrate Br and Cs deficiencies with a concomitant increase in the Ti peak area relative to UHV-cleaved sample ratios. Thus, the spectra in Fig. 3.4E demonstrate a rapid oxidation at Cs_2TiBr_6 surfaces upon air exposure and indicates that the material readily forms titanium oxide in an air ambient.

3.3.4 Electronic Properties of Nascent, Vacuum-Cleaved, and Air Exposed Cs_2TiBr_6

Ultraviolet photoelectron spectra (UPS) established electronic structure of large-grain Cs_2TiBr_6 to elucidate the effect of the varying chemical speciation as established in the XP spectra and XRD traces.

Figure 3.5 shows UP spectra of a nascent sample, a freshly UHV cleaved sample, and a sample that was exposed to air for 10 min following UHV cleaving. Spectra of sanded and DCM rinsed and then sanded Cs_2TiBr_6 samples largely resembled the nascent sample UP spectrum in frame A and were therefore not considered further. Importantly, we acquired UP spectra for a minimum of three samples with Fig. 3.5 including representative spectra for each surface condition. The red dashed lines in Figure 3.5 represent linear regressions of the low-kinetic-energy (high-binding-energy) edge of the secondary electron feature in each spectrum. The x-axis intercepts of each green-dashed regression mark the energy difference between the binding energy of the valence band maximum vs the sample Fermi level, or $\mathbf{E}_F - \mathbf{E}_{VBM}$. The red-dashed regression to the x-axis reveal secondary-electron photoemission cutoff energies, ESEC, that determine sample work functions, $\phi = \mathbf{E}_{He\,I} - \mathbf{E}_{SEC}$, where $\mathbf{E}_{He\,I} = h\nu = 21.218$ eV, and when $\mathbf{E}_F = 0$ eV based on recent calibrations.[46]

The nascent sample in Fig. 3.5A demonstrates a work function of $\phi = 3.35$ eV with a significant density of states and photoelectron counts at higher binding energies (or lower kinetic energies) than the secondary electron cutoff feature. Such features typically indicate surface contamination.[55–56] Similarly to the unexpected features near the secondary-electron cutoff, the 3.37 eV fitted difference between the valence band maximum and the sample Fermi level

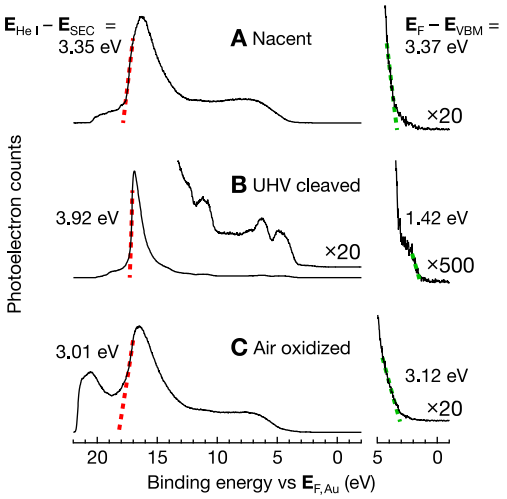

Figure 3.5 Representative ultraviolet photoelectron spectra large-grain Cs_2TiBr_6 surfaces including (**A**) nascent, (**B**) UHV cleaved, and a sample (**C**) following UHV cleaving and ten minutes of air exposure. Relative to nascent and air oxidized samples, a UHV-cleaved sample as in frame **B** demonstrates significantly more well-resolved valence band electronic structure as well as $\mathbf{E}_F - \mathbf{E}_{VBM}$ = 1.42 eV that is reasonable for this ~1.8 eV band gap material. Nascent and air oxidized samples demonstrated valence band electronic structure that resembled TiO_2.[26] ©2020 American Chemical Society

energy is highly unexpected for the ~1.8 eV band gap Cs_2TiBr_6 material under study. The combined ultraviolet photoelectron features in Fig. 3.5A would imply that the interfacial oxide contamination presented by Fig. 3.4A also dominates the electronic structure of nascent samples. Spectra of sanded and DCM rinsed and then sanded Cs_2TiBr_6 samples similarly demonstrate near-Fermi-edge structure that are indicative of oxidation.

In contrast to spectra of nascent samples, the representative UP spectrum for a UHV cleaved sample in Fig. 3.5B demonstrates significantly different features as may be expected for an oxide-free surface as determined by XPS in Fig. 3.4D. The spectrum in Fig. 3.5B possesses a $\phi = 3.92$ eV work function, and a 1.42 eV difference between the valance band maximum and the Fermi level energies. The $\mathbf{E}_F - \mathbf{E}_{VBM}$ = 1.42 eV difference matches well with thin film studies of Cs_2TiBr_6, however the ϕ = 3.92 eV work function value is somewhat lower than the $\phi = 4.4$ eV work function in that study.[24]

Following UHV cleaving and a ten-minute air exposure as shown in Fig. 3.5C, both work function and valence band structure return to similar values as acquired for nascent samples. Interestingly, the spectrum in Fig. 3.5C demonstrates a significant density of states at lower kinetic energy or higher

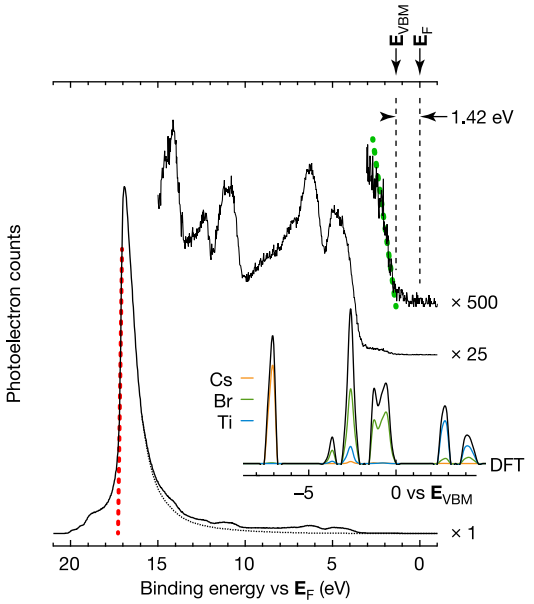

Figure 3.6 A baseline-corrected 25× inset for the UP spectrum of a UHV cleaved, large-grain Cs_2TiBr_6 surface along with a density-of-states DFT calculation. The 500× inset reveals the $E_F - E_{VBM}$ = 1.42 eV shift for alignment of the experimental and calculated results that demonstrate good agreement for valence band features located at ~2.5 and ~4.9 eV and the shoulder feature at a binding energy of ~7.8 eV vs E_F.[26] ©2020 American Chemical Society

binding energy than the secondary electron cutoff itself. As with the nascent sample spectrum in Fig. 3.5A, the observation of such states implies significant contamination on the air exposed surface.

Beyond work function and Fermi-level determination, UHV cleaving and the resulting oxide-free surface reveals significantly more valence band structure in Fig. 3.5B relative to the broad valence features in frames A and C. Figure 3.6 explores the valence structure of the freshly UHV-cleaved, large-grain Cs_2TiBr_6 surface in more detail with a baseline-subtracted 25× inset based on the dashed baseline in the 1× spectrum. The 25× inset reveals valence band features with local maxima at 2.5, 4.9, 6.2, 10.8, 12.4, and 14.2 eV along with a less-well-resolved shoulder feature at a binding energy of 7.4 eV below E_F. To compare with the experimental electronic structure, Fig. 3.6 further includes the density of states as determined by DFT. The DFT results agree well with previous computational analyses of the density of states between 0–3 eV more negative than E_{VBM}, but we include a calculation towards lower energies to compare to the UP spectra. Figure 3.6 presents the DFT results on an energy scale such that 0 eV corresponds to E_{VBM}, as is typical for

electronic structure calculations. Based on the $\mathbf{E}_F - \mathbf{E}_{VBM} = 1.42$ eV from Fig. 3.5B that is reproduced and highlighted in the 500× inset in Fig. 3.6, we shift the energy axis of the DFT plot by 1.42 eV to align directly with the binding energy axis from the UP spectrum. Interestingly the UP spectra and the calculated density of states demonstrates strong qualitative agreement in the intensities of individual features with excellent quantitative agreement in energy alignments. The computational results imply that Br valence states dominate the observed valence edge features in the photoelectron spectrum with lower-energy contributions from cesium valence states.

3.4 Discussion

3.4.1 Properties and Stability of Nascent, Washed, and Abraded Surfaces

As synthesized, large-grain Cs_2TiBr_6 demonstrates significant quantities of an interfacial oxide that is most likely titanium dioxide for the absence of XPS-observable Cs, strongly attenuated Br, and the absence of BrOx– species. Synthesis methods may yield unreacted $TiBr_4$ that deposits on the surface during the cooling stage of the synthesis that may be an additional source of titanium oxide on nascent surfaces. Additional titanium oxide from oxidizing $TiBr_4$ may be the particular cause of no observable Cs species on nascent surfaces as in Fig. 3.4A. Separate synthesis protocols attempted to getter $TiBr_4$ vapor away from the Cs_2TiBr_6 crystal melt during late-stage cooling by dropping the temperature of the non-crystal-containing side of a growth ampoule. In our hands, such gettering steps ultimately yielded Cs_2TiBr_6 samples with poor crystallinity and imperceptibly small facets in the absence of magnification. In the absence of a late-stage getter step, we anticipated that the as-synthesized large-grain Cs_2TiBr_6 crystals may contain a nominal quantity of adsorbed $TiBr_4$. Mentioned in the experimental details in the Supporting Information section in Appendix A, DCM rinsing of nascent samples yielded yellow-colored washings that indicates that as-synthesized, nascent crystals likely did possess adsorbed $TiBr_4$.

Even with rapid, "air-free" transfer from a growth ampoule to the photoelectron spectrometer for analyses, nascent sample surfaces were dominated by titanium oxide. The dominance of metallic-ascribable O 1s and of Ti 2p features along with partially suppressed Br 3d and completely suppressed Cs $3d_{5/2}$ features as in Fig. 3.4A strongly supports the presence of interfacial titanium oxide. The absence of an XRD feature at 25.4° due to a TiO_2 reflection in Fig. 3.2 suggests that any interfacial titanium oxide is likely amorphous.[57] This amorphous titanium oxide further dominates the electronic structure of nascent crystals as revealed in the UP spectrum in Fig. 3.4A that has a Fermi level energy that is 3.1 eV more positive than the valence band edge. While not a realistic result for a ~1.8 eV band gap Cs_2TiBr_6 crystal, 3.1 eV is a

very realistic $\mathbf{E}_F - \mathbf{E}_{VBM}$ value for highly doped, n-type TiO_2.[58] Thus, interfacial titanium oxide dominates both the chemistry and electronic structure of nascent, large-grain Cs_2TiBr_6 surfaces.

In the cases of just DCM rinsing, just physical abrasion, and a combined DCM rinse with physical abrasion, all surfaces demonstrated improved quantities of cesium and bromine relative to titanium. However, as revealed by Table 3.1, those physiochemical surface treatments yielded cesium and bromine quantities that remained well short of the 2:1:6 bulk stoichiometry of Cs_2TiBr_6, and titanium oxide was observed for all so-treated samples.

What is unclear from the present results is whether the physiochemical treatments incompletely removed interfacial oxides, or whether processing in a not-quite-oxygen-free flush box and subsequent "air-free" sample transfer reformed a new oxide. As mentioned in the Supporting Information Section, the typical time between a surface treatment, mounting of a sample on an XPS puck, transfer to the XPS via an air-free transfer suitcase, and initial evacuation was 10–20 min. At ~5 ppt of oxygen in the flush box, 20 min in a flush box ambient translates to an oxygen dose of 30 s in air. Notably, the initial XRD trace in the time study in Fig. 3.3A reveals the presence of a CsBr reflection that indicates that surface decomposition has already initiated following one minute. Thus, the 20 min duration in the flush box ambient may have yielded demonstrable oxidation as observed in the XP spectra in Fig. 3.4B–C. It may be possible for physiochemical treatments to yield a chemically and electronically pristine Cs_2TiBr_6 surface, but the present results imply that such treatments require rapid transfer under a rigorously oxidant-free environment.

XRD and XPS results elucidate viable mechanistic aspects of Cs_2TiBr_6 interfacial oxidation. Cumulative results indicate that oxidation yields crystalline CsBr and amorphous TiO_2 on the surface with likely desorbing species including HBr from a reaction with water and possible Br_2 from a reaction with atmospheric O_2. Both reactions would yield a decrease in XPS-observed bromide, but the relative decrease in interfacial cesium vs titanium for Fig. 3.4E vs 3.4D implies that significant interfacial partitioning occurs concomitantly with oxidation. A model consistent with the data is the formation of a TiO_2-rich layer nearest to the interface with a CsBr-rich layer between the TiO_2-rich layer and the bulk Cs_2TiBr_6 itself. The formation of a sandwiched CsBr layer may yield a metal-insulator-semiconductor (MIS)-style arrangement with the precise implications for photovoltaics depending on the resulting thickness of each layer and defect states due to incomplete restructuring. Carrier transfer dynamics at pristine and oxidized interfaces remain subjects of ongoing study.

3.4.2 Properties of "Pure" Cs_2TiBr_6 Material

Cleaving the large-grain Cs_2TiBr_6 crystals under ultrahigh vacuum conditions revealed unique surface chemistry and electronic properties as compared to other surface preparations. In contrast to the other surface preparations under study, XP spectra of UHV cleaved samples demonstrated no observable O 1s features, and interfacial Cs:Ti:Br ratios that best match the bulk stoichiometries. We interpret these results to mean that the UHV cleaving best reveals pristine Cs_2TiBr_6 surfaces on these large-grain samples, and that the subsequent UPS-derived electronic properties best reflect the interfacial electronics of Cs_2TiBr_6 itself. The resulting Fermi energy of 1.42 eV vs the valence band edge implies moderate n-type doping, and agrees well with our previous collaborative study of thin-film material from the Padture group.[24] Interestingly, the experimental work function of 3.92 eV differs from that report by ~400 mV,[24] and yields a valence band edge of –5.34 eV vs the vacuum energy level, and a conduction band edge of ~–3.5 eV vs the vacuum energy when assuming a band gap energy, $\mathbf{E}_g$, of approximately 1.8 eV.

Beyond differences in valence-vs-Fermi energies and work function values, UHV-cleaved material demonstrates significantly more valence band electronic structure as compared to the nascent and air-oxidized samples. The agreement between the UPS-determined valence structure and the results from a density of states calculation as in Fig. 3.6 further supports the successful observation of interfacial electronic structure for the large-grain Cs_2TiBr_6 samples under study.

3.4.3 Implications for Photovoltaics

Thin films of Cs_2TiBr_6 have demonstrated promising solar-to-electric power conversion efficiencies that indicate promise for both single-absorber and tandem-junction PV. The present study demonstrates instability of large-grain Cs_2TiBr_6 crystals towards oxidation in an air ambient, and a related study noted similar instability in powdered material.[44] In this work, the electronic properties of nascent, oxide-dominated Cs_2TiBr_6 surfaces have electronic structures that differ greatly from "pure" Cs_2TiBr_6 as enabled by UHV cleaving experiments. One possible way to reconcile good PV properties with ambient air instability is that interfacial titanium oxide layers enable carrier conductivity that is not significantly attenuated by a concomitant increase in interfacial CsBr, and that neither chemical species contribute to a deleterious surface trap state density. A related question is whether particular Cs_2TiBr_6 deposition or processing methods yield films that self-passivate with a nominal amount of titanium oxide. Certainly, a conduction band minimum of approximately –3.5 eV vs the vacuum energy level for Cs_2TiBr_6 from this study would be well positioned to inject photogenerated electrons into a passivating TiO_2 layer that has a conduction band minimum at approximately –4.0 eV vs vacuum. Further, the proclivity of Cs_2TiBr_6 to form interfacial

titanium oxide may further suggest that passivation methods might involve atomic-layer deposited TiO_2 that may not significantly disrupt the interfacial chemistry and electronics of Cs_2TiBr_6 in any way that it would not do itself. Further studies that correlate interfacial chemical and electronic structure are clearly warranted.

3.4.4 Conclusions and Future Work

We employed a high-temperature melt to synthesize large-grain Cs_2TiBr_6. The resulting crystals were not air stable and degraded in air to form cesium bromide and titanium oxide. Nascent Cs_2TiBr_6 surfaces demonstrate cesium and bromine deficiencies, but ultrahigh vacuum cleaving yielded peak area ratios that were nearly stoichiometric. The electronic properties of Cs_2TiBr_6 differed based upon surface processing, with nascent samples having fermi levels and work functions that were characteristic of TiO_2 and UHV cleaving yielding valence band structure that agreed with density-of-state calculations for Cs_2TiBr_6 and a Fermi level indicative of an n-type semiconductor. These electronics hold promise for potential application in tandem-junction PV but present additional questions about the stability of the material, while surface metal oxide species present a potential route for future surface passivation.

3.4.5 Supporting Information and Associated Content

Appendix A includes a full description of experimental methods for material preparation, surface treatments, and analytical methodologies. High temperature melt method descriptions include ampoule preparation, sealing, synthesis, and cracking. Surface preparation method descriptions include chemicals used, sample preparation, and the inert environments that were employed. Descriptions of the full analytical methods include spectroscopic conditions, peak fitting parameters, and methods. The Supporting Information further includes representative $(\alpha h\nu)^{1/2}$ and $(\alpha h\nu)^2$ vs photon energy Tauc plots from the UV-Vis results for large-grain Cs_2TiBr_6 samples in Fig. A.2. Lastly, Appendix B describes construction and operating procedures for the *in vacuo* crystal cleaving set-up.

CHAPTER 4

DEVELOPMENT OF A SCHLENK-LINE-INTEGRATED, ATOMIC-LAYER-DEPOSITION INSTRUMENT FOR DIRECT OXIDE PASSIVATION OF ATMOSPHERICALLY UNSTABLE MATERIALS

Abstract

Atomic layer deposition (ALD) provides an avenue for controlled molecular depositions of metal oxides to passivate substrates. We present the development of an ALD instrument which was Schlenk-line integrated to allow for air-free substrate loading and transfer. Our Schlenk-line-integrated ALD was equipped for flow of an inert carrier gas and was programmed with a LabVIEW program for control of precursor dosing. We tested this instrument by depositing TiO_2 thin films of varying thicknesses onto oxidized silicon substrates. X-ray photoelectron spectroscopy characterized the resulting films and identified linearity between film thickness and number of depositions.

4.1 Introduction: Why Are We Doing This?

Atomic layer deposition (ALD) is a thin-film-deposition technique that effects a layer-by-layer growth of films by adsorbing precursors to reaction substrates.[59–60] In ALD, vapor phase precursors are alternatively dosed onto a substrate on which the precursors chemisorb and react with each other.[61] Precursor reactions are self-limiting, which allows for molecular control over film thickness.[60] Not only does ALD offer controlled deposition of thin films, it also offers general uniformity and is a well-established process.[62]

Due to the high level of control over film thickness and uniformity offered by ALD, it has emerged as a useful technique for semiconductor processing, catalysis, and passivation.[62–64] The wide range of materials that are capable of being uniformly deposited as high-quality films by ALD positions it well for these purposes. However, commercial ALD systems can cost >$100,000, which does not make them a cost-effective instrument for fundamental studies in a small academic research laboratory, but rather positions ALD well for industrial applications.[65]

Recent developments have aimed to develop cost effective ALD systems have provided a roadmap to researchers for bringing this exciting deposition technique to the lab bench.[66–67] However, most ALD systems, including those that have been fabricated in a cost-effective way, require transfer of substrates in an air ambient. Given these gaps in both the cost-effective and air-free sample transfer areas of ALD systems, we aimed to develop a Schlenk-line-integrated ALD.

The applications of metal oxide ALD for passivation of perovskite materials for solar PV devices presents an exciting area of exploration for Cs_2TiBr_6.[32,68–70] The band edges of oxide-free Cs_2TiBr_6 are well aligned to the band edges of TiO_2, and TiO_2 is stable in an air ambient while Cs_2TiBr_6 is not.[26] This further motivated us to explore ALD configurations which allow for air free deposition of metal oxides onto Cs_2TiBr_6 surfaces and air free transfer of the resulting samples. With these experimental constraints in mind, we herein outline the needs of such a set-up.

Firstly, air-free ALD would require some type of inert carrier gas other than air and this carrier gas would need to have a controlled and measured flow.[61] A carrier gas with controlled flow would be necessary to move ALD precursors from their respective storage locations to the substrate that deposition is occurring at. From this need, we identified a second need which is for precursors that can be flowed from point A to point B by the carrier gas. Constraints here include vapor pressure, as a precursor that is not capable of being vaporized at a reasonable temperature or pressure would not be ideal in terms of flow. Additionally, control of dosing of the precursors into the instrument would be necessary on timescales within a millisecond to prevent too much vapor from being introduced. Our next need involves temperature

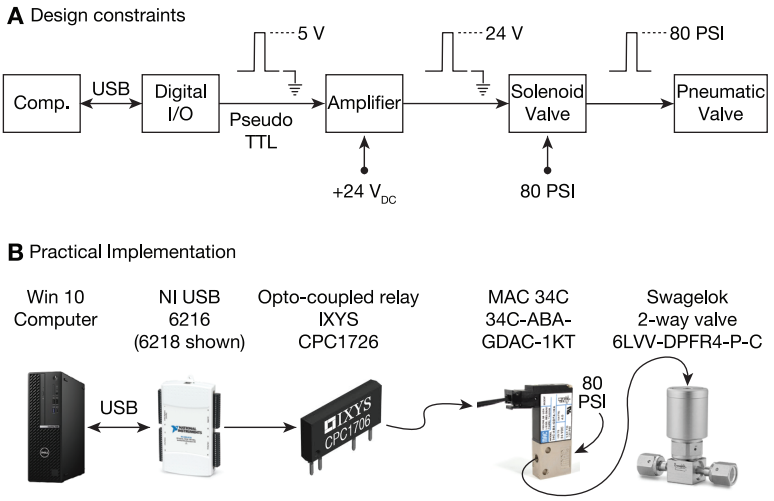

Figure 4.1 Design constraints (**A**) and practical implementation (**B**) of pneumatic valves to control millisecond dosing of vapor phase precursors for transport during ALD. Design constraints (**A**) considered the limitations of a pneumatic valve and then practical implementations (**B**) were based upon what electronics were chosen for such constraints to meet the needs of this Schlenk-line-integrated ALD.

control, as these gas phase ALD reactions occur at temperature and in order for flow to transport precursors from their storage to a substrate for reaction, temperature must be consistent and without cold spots.[64] The presence of cold spots would encourage condensation of precursors before reaching the substrate. Finally, this experimental set-up would need to include a reactor that holds Cs_2TiBr_6 samples and can be Schlenk-line integrated and detachable without venting the entire set-up. Having both of these characteristics would be necessary to load and remove samples for deposition in the recirculating glovebox, which would only be possible if the reactor can be evacuated and is small enough to be pumped into the glovebox (thus removable from the entire apparatus).

4.2 Design Constraints

The following design principles aimed to fulfill the needs of a Schlenk-line integrated ALD for air free deposition and sample transfer. The first design principles we utilized are outlined in Fig. 4.1 and considered the need for controlled millisecond dosing of vapor phase precursors. Quick, controlled opening and closing of valves to let out small amounts of a vapor phase precursor can easily be affected with pneumatic valves. Figure 4.1

demonstrates the necessary design constraints associated with controlling a pneumatic valve.

As show in Figure 4.1A it was desirable for our design to be capable of communicating with a computer so that precursor dosing commands could be preprogrammed. This connection to a computer required communication back and forth with a digital input/output device that would be capable of both sending and receiving digital signals, which took the form of a USB connection between the two. The digital input output device, which utilizes pseudo TTL logic signaling, was capable of sending a 5 V_{DC} or 0 V_{DC} (common/ground) signal, however, solenoid valves that can quickly and effectively deliver pressure to a pneumatic valve require 24 V_{DC}. To bridge this gap, we included an optically-coupled amplifier (optoamplifier) that can switch on and off a connection to a +24 V_{DC} power supply based on the input of a 0-or-5 V_{DC} pseudo TTL logic signal from the digital I/O device. This addition of an amplifier allows a 24 V_{DC} potential to be applied to the solenoid valve to switch. When compressed gas is supplied to the input gas line of the solenoid, the resulting solenoid switching based on the presence or absence of the 24 V_{DC} potential vs its common/ground yields the application of that input gas to its output line. When utilizing an input of 80 PSI of compressed gas, this opening and closing should occur on millisecond timescales.

Figure 4.1B shows the practical implementation of these constraints. Firstly, we connected a Windows 10 computer via a USB to an NI USB 6216, which is a digital I/O device. The NI USB 6216 was selected for its availability in the group, but it fits the design requirements of having many digital I/O lines as well as several 16-bit analog I/O lines as well that are discussed below. Using an in-house-developed LabVIEW program, the computer was able to send a digital output to the NI USB 6216 signaling the pneumatic valve to open. Next, an opto-coupled relay in an integrated circuit received the digital output, the 5 V_{DC} charge, and a +24 VDC charge from a 5 and 24 V_{DC} dual power supply. A +24 V signal was then sent to a MAC 34C solenoid that had 80 PSI of UHP nitrogen connected to it. Once given the 24 V potential, the MAC 34C opens the pressure to a Swagelok 2-way valve which opens until given a subsequent signal to close. Of particular note, the MAC 34C valves being used contained either 1.6 W or 4.0 W solenoids (higher power translates into faster switching). This is notable as the 24 V_{DC} power supply must be capable of sourcing sufficient current to drive *all* of the solenoids simultaneously. Given the need for $\frac{1}{6}$ A for one 4.0 W solenoid, and a maximum of six solenoids for controlling up to six values, the 24 V_{DC} must be able to source a minimum of 1 A of current or 24 W of power.

The second design principles we employed considered how to flow an inert carrier gas over the set-up in a controlled manner to transport the vapor phase precursors to the desired reaction substrate. Not only did this control require the ability to set flow, but also required the ability to measure the resulting

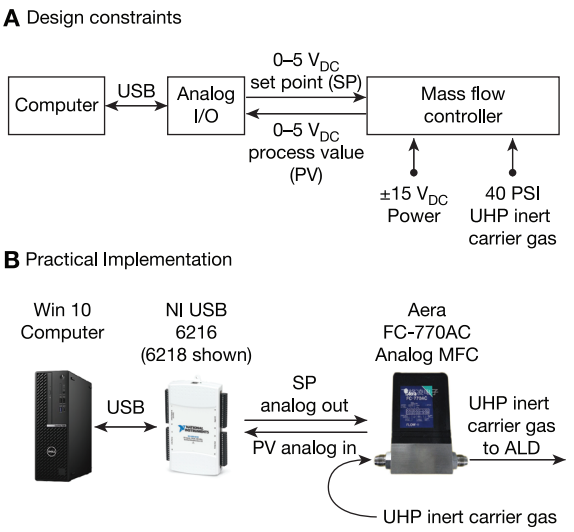

Figure 4.2 Design constraints (**A**) and practical implementation (**B**) of a mass flow controller (MFC) to control and measure flow of an inert carrier gas through the ALD instrument. Design constraints (**A**) considered the limitations of a mass flow controller and then practical implementations (**B**) were based upon what electronics met such constraints for the Schlenk-line-integrated ALD.

flow to ensure that set flow values are correct. In considering these design principles, we determined the following design constraints, outlined in Fig. 4.2A. These design constraints required a mass flow controller. A mass flow controller fulfills both design needs of setting, controlling and measuring flow. In determining the constraints of a mass flow controller's communication with an external control. Some use digital I/O including RS–485, Modbus, and other protocols that would require the proper adapter as well as learning that specific communication protocol. We opted for communication via analog I/O, which is also a fairly common method of communicating with mass flow controllers. So, we first established that a mass flow controller functions by sending and receiving a linear signal ranging between 0–5 V_{DC} that corresponds to no-flow to full-rated flow. (There are gas sensitivity factors that require this reading to be scaled for many gases, but nitrogen does not have that issue. Look up "MFC gas sensitivity factors" on the Internet for more details.) An analog out signal that is generated by some analog I/O board is received by the MFC as the setpoint value (SP), and the MFC sends back another analog signal that is read as an analog in signal by that I/O board as the process value (PV) of the actual flow rate of gas that the MFC is actually flowing. In addition to sending and receiving analog signals, a mass flow controller requires electrical power and the and 40 PSI of carrier gas for the purpose of flow. The MFC we chose utilized ±15 V_{DC} for power. An

analog I/O device would be capable of transmitting and receiving signals for the setpoint and process value, but this device would not be programmable and therefore a USB connection for these signals to be further transmitted to a computer, which could be programmed with set points for flow and could receive process values for measuring flow outputs, all by sending and interpreting 0–5 V_{DC} analog values.

Figure 4.2B illustrates the practical implementation that resulted from the design constraints presented by the need for a mass flow controller for controllable and measurable flow of an inert carrier gas. Previously used in Figure 4.1B's practical implementation of pneumatic two-way Swagelok valves, a Windows 10 computer connected to an NI USB 6216 would allow for analog I/O signals to be transmitted between an Aera FC-770AC mass flow controller (MFC). As mentioned above, the NI USB 6216 has several 16-bit analog in lines, and two 16-bit analog out lines. The number of bits determines the resolution of the unit's conversion from analog to a digital signal, as well as the accuracy with which the unit can generate a specific analog signal. For an analog input or output channel that has a ±10 V range, 16-bits of resolution means that the unit has a voltage step size of 20 V / 2^{16} = 0.305 mV in both the analog voltages that it reads, and the analog outputs that it generates. The 0.305 mV step size of the NI USB 6216 is more than enough resolution for communicating with the MFC, as MFCs have a setpoint accuracy of 1% of its full scale range. Thus, if the MFC communicates based on an analog signal 0–5 V_{DC} that corresponds to no flow to full-rated flow, the minimum accuracy needed in the analog signals should be 50 mV (or 1% of 5 V) or better. Thus the 16-bit analog I/O is actually overkill for this particular application.

The Aera FC-770AC MFC was capable of up to 100 sccm (standard cubic centimeters per minute) flow and was originally for H_2 gas. This specific unit was selected based on other research papers utilizing 20 sccm, having analog I/O, utilizing VCR gasket fittings to be compatible with the rest of the plumbing, being brand new, and being available on eBay for a reasonable price (less than $300). The MFC was connected to a UHP inert carrier gas and an in-house developed LabVIEW program set values for flow based upon a 0–5 V_{DC} range and received process values within a 0–5 V range to measure flow.

4.2.1 Fabrication

The design constraints detailed above, and the resulting practical implementations, were combined during fabrication while working towards full implementation of Schlenk-line integrated ALD.

4.2.1.1 Electronics The electronic controls for the ALD were fabricated and mounted on a square of polycarbonate so that they would be located in the same spot and could be vertically mounted in the fume hood away from the

ALD manifold and reactor. These electronics followed several of the design principles outlined in Figs. 4.1–4.2. Each of the components of the electronics was fastened to the polycarbonate by screws. Male-female threaded hex standoffs (1 3/4", 6-32, McMaster-Carr) were placed throughout the electronics board to fasten a piece of polycarbonate over the top of the set-up to protect it from dust and other hazards in the fume hood. The top and bottom of the electronics board was also lined with polycarbonate, however the two sides were left open for access to wires and airflow. Additionally, the removability and the transparent nature of the top panel of polycarbonate was chosen specifically for debugging, as debugging would be much quicker when able to see all of the wires and able to quickly access them.

Figure 4.3 illustrates the completed electronics. Barrier strip 1 (WM5766-ND, Digi-Key), shown in Fig. 4.3A, connected the wiring for MFC power and MFC signals, and the four pneumatic valves. The barrier strip was left hanging slightly outside of the electronics for easy access to make wired connections and for quick troubleshooting. Figure 4.3B demonstrates the solenoid digital connections, which includes each of the practical applications outlined in Fig. 4.1B. These digital connections were wired to the integrated circuit and are detailed further below. In Figure 4.3C we show a TC Gauge 120 VAC receptacle (Q337-ND, Digi-Key) which supplied power to each of the five temperature controllers (LOVE 32B, Dwyer Instruments, Michigan City, IN) used to heat the ALD and a TC gauge used to measure pressure in the Schlenk line. Next, the multifunction I/O device (NI USB 6216, National Instruments) in Fig. 4.3D connected to the USB Hub (BYEASY USB 2.0 Hub 7 Ports, Amazon) which connected to the computer. Figure 4.3F and 4.3H shows a +5, +24 V power supply and a ±15 V power supply, respectively. The +5, +24 V power supply in Fig. 4.3F supplied power to the USB hub (Fig. 4.3E) and the solenoid digital connections (Fig. 4.3B) while the ±15 V power supply in Fig. 4.3H supplied power to the MFC via barrier strip 1 (Fig. 4.3A). Barrier strip 2 (WM5766-ND, Digi-Key) seen in Figure 4.3G connected all of the internal power wires. Finally, a 15 A circuit breaker switch is illustrated by Fig. 4.3I and allowed for the entire ALD electronics board to not only be powered by one source, but also allowed the board to be safely turned off in the event of any electrical issues.

The solenoid digital connections were the only component of the ALD electronics that were in-house fabricated and are shown in Fig. 4.4A. Four digital connections were made for each of the four solenoids. Following the design principles outlined in Fig. 4.1A and the resulting practical applications outlined in Figure 4.1B, each of the solenoid digital connections contained an opto-coupled relay (Single-Pole, Normally Open DC Power SIP Relay, IXYS IC, Milpitas, CA). Figure 4.4B shows the circuit diagram with the opto-coupled relay between the solenoid and multifunction I/O device.

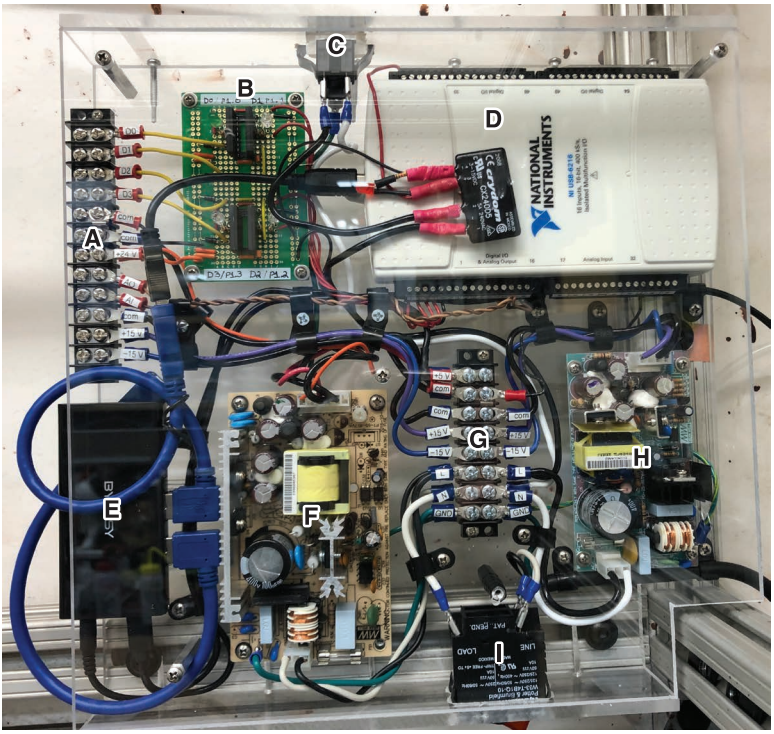

A Barrier Strip 1 (MFC, Pneumatics)	**E** USB Hub
B Solenoid Digital Connections	**F** +5, +24 V Power Supply
C TC Gauge 120 VAC Receptacle	**G** Barrier Strip 2 (Internal power)
D Multifunction I/O Device (NI USB-6216)	**H** ±15 V Power Supply
	I 15 A Circuit Breaker Switch

Figure 4.3 ALD electronics as mounted to aluminum struts in the fume hood. The two barrier strips (**A**, **G**) connected each individual component. The circuit breaker switch (**I**) supplied power to the whole system, while +5, +24 V and ±15 V power supplies supplied specific amounts of power to the USB hub (**E**), pneumatic valves, and mass flow controller. The USB hub (**E**) connected the multifunction I/O device (**D**) to the computer (not pictured). Solenoid digital connections (**B**) were made using an in-house fabricated integrated circuit, while a TC Gauge 120 V_{AC} receptacle (**C**) allowed for power to be supplied to temperature controllers and a TC gauge.

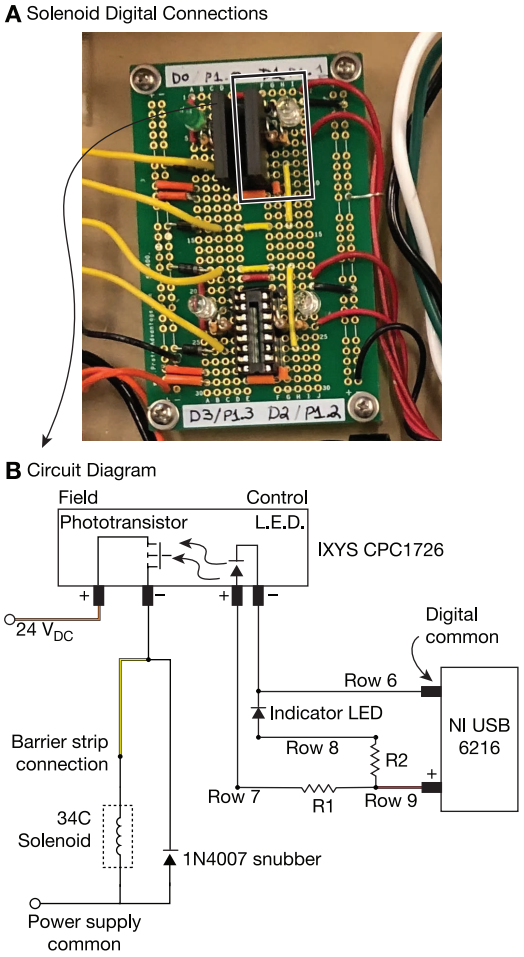

Figure 4.4 The integrated circuit for the solenoid digital connections (**A**) consisted of four separate opto-coupled relays for each of the four solenoids. A box is drawn around one of the digital connections and the circuit diagram (**B**) illustrates the configuration within the box.

Once the electronics fabrication was complete, the electronics board was covered with the top panel of polycarbonate and mounted vertically in the back of the fume hood.

4.2.1.2 Manifold and Precursors The manifold was constructed using VCR fittings. The Aera FC-770AC MFC (Hitachi Metals, Purchase, NY) had two male VCR fittings and was connected to a female VCR Swagelok 2-way pneumatic valve (6LVV-DPFR4-P-C, Swagelok). The pneumatic Swagelok 2-way valve was connected to a $\frac{1}{4}$" stainless steel, male VCR face sealing union tee

(SS-4-VCR-T, Swagelok). The union tee was connected to another Swagelok 2-way valve at the bottom and a female VCR connection to the right, made using $\frac{1}{4}$" stainless steel tubing. The connection to the pneumatic valve on the bottom portion of the union tee was for a precursor container. The connection to the $\frac{1}{4}$" stainless steel tubing on the right of the union tee was then connected to another union tee. Below that union tee was another 2-way Swagelok valve, for another precursor. This was repeated once more, so that one 2-way Swagelok valve was connected to the MFC and three 2-way Swagelok valves were positioned in a horizonal line below the valve connected to the MFC for three precursor containers. Finally, after the portions for the pneumatic valves that connected the precursor containers, a stainless steel $\frac{1}{4}$" male VCR union elbow connected the portion of the manifold dedicated to the precursor containers to a section of flexible stainless-steel tubing, which we refer to as the "down tube".

For each precursor container, from top to bottom, a VCR face seal fitting with a $\frac{1}{4}$" male VCR fitting and a $\frac{1}{4}$" male NPT connector body and fitting (SS-4-VCR-1-4, Swagelok) was connected to the Swagelok 2-way pneumatic valve by the VCR fitting. The NPT end was covered in Teflon tape and connected to a stainless-steel inch-to-NPT male-female hex thread adapter. The wide end of the hex thread adapter was 1" and needed to be connected to a to a 3" length of stainless-steel NPT pipe. However, this pipe also had a male fitting, so a threaded pipe fitting (4464K356, McMaster) was required to connect the two. The fitting was connected using Teflon tape and further sealed by Hysol 1C epoxy just to be safe and minimize any possibility of a leak at these pipe-thread fittings. The hex thread adapter and the pipe were connected using Teflon tape and were further sealed with Hysol 1C epoxy. Finally, the 3" pipe was connected to a female NPT cap (4464K512, McMaster) using Teflon tape and Hysol 1C epoxy to prevent leaks. The total space within this plumbing yielded volumes that are sufficiently large to provide ample vapor headspace when filled with 10–20 mL of their respective liquid precursor.

4.2.2 Reactor

The reactor consisted of a female-female 24/40 ₹ glass straight connecting adapter (Fisher Scientific) and two elbow connections. The elbow connections were in-house fabricated by connecting a 24/40 ₹ male glass joint and a $\frac{1}{4}$" valve. The valve was at a 90° angle to the joint. Two elbows were created to seal both ends of the straight connecting adapter. The valves allowed for sealing of the reactor from an air ambient to facilitate air free sample loading and sample transfer within a recirculating glovebox. The ground glass joints of the straight connecting adapter and the valve were lubricated using a high temperature vacuum grease that would be stable at ALD temperatures.

4.3 Bootstrapping

Following fabrication of the electronic controls, manifold, precursor containers, and glass reactor, the individual components of the ALD were combined to finish creating a functional experimental set-up. The combination of individual components included wiring solenoid, MFC, and temperature controller connections to the electronics board, wrapping the manifold and precursors in heating tape, and preparing the precursors.

The manifold was mounted in the back of the fume hood first. Mounting was affected by bolting the MFC to an aluminum strut in the back of the fume hood and then using clamps to hold the rest of the apparatus in place. The MFC came with several threaded holes in it which allowed for easy mounting.

Figure 4.5 shows the entire mounted ALD. We will discuss each component of this diagram throughout this chapter, but for reference, the MFC (Fig. 4.5A) is out of frame of the picture. The pneumatic valves for control of flow and each precursor are shown in Figure 4.5B, and Figure 4.5D–F. The pneumatic valves are titled D0–D3 where D0 corresponds to the MFC valve, and D1–D3 correspond to the precursor valves. D1 controls the water precursor, while D2 controls the TEMATi precursor. D3 was left blank and presents an opportunity to add an additional precursor for future experiments. The manifold is described by Fig. 4.5C and stretches the length of D1 to the down tube.

The precursors themselves are shown in Figure 4.5G–H, where the water precursor (G) was not wrapped, while the TEMATi precursor was wrapped. The down tube is described by Fig. 4.5I and is connected to the reactor (Fig. 4.5J) by a Swagelok valve. The down tube can also bypass the reactor by the middle Swagelok valve, which allows for easy detachment of the reactor without venting the entire ALD set-up. Figure 4.5K shows a trap, which is cooled with liquid nitrogen during depositions to collect unreacted precursors. The Schlenk-line itself (Fig. 4.5M) also has its own liquid nitrogen cooled trap as a second line of defense against the precursors. The Schlenk line that the ALD was attached to was also equipped with an inert gas line (Fig. 4.5N) which allowed for backfilling of the reactor with inert gas for easier detachment. The electronics are shown in Figure 4.5L to demonstrate the location of the electronics board with respect to the ALD itself.

4.3.1 Precursor Loading

Concomitant with manifold mounting, the precursor containers whose fabrication and location on the set-up is described above, were loaded with the precursors. The water precursor was simply poured into the precursor container using Milli-Q filtration system to provide all water at 18 MΩ cm resistivity (Millipore). The water precursor container was filled about halfway

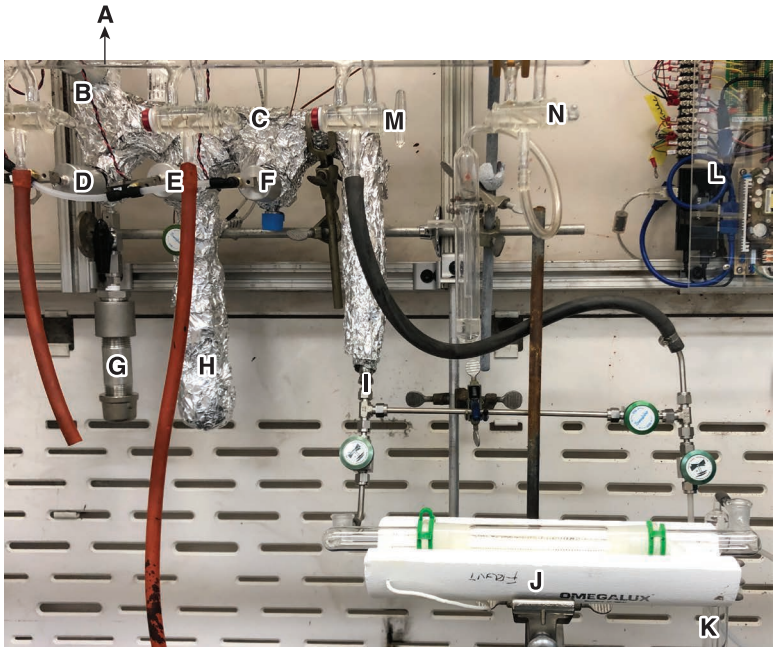

A MFC (out of frame)	**E** D2 (TEMATi pneumatic)	**I** Down Tube	**M** Schlenk line stopcock
B D0 (MFC pneumatic)	**F** D3 (unused)	**J** Reactor	
C Manifold	**G** Precursor 1 (H_2O)	**K** ALD Trap	**N** Inert gas line stopcock
D D1 (H_2O pneumatic)	**H** Precursor 2 (TEMATi)	**L** Electronics	

Figure 4.5 The mounted and heat-tape-wrapped ALD sits behind the Schlenk-line in the fume hood. The MFC (**A**) is not pictured but would be located above D0 (**B**) which is the pneumatic valve which controls the MFC. The electronics (**L**) were positioned up and away from the reactor furnace (**J**) so as to keep the electronics at a low temperature relative to the heated ALD.

to leave headspace for the water vapor to sit above the liquid precursor. Following loading of the water precursor, the precursor container was sealed with a Swagelok valve and the Swagelok valve was connected to the 2-way Swagelok pneumatic valve. With the water precursor sealed by the Swagelok valve, the connection between the 2-way Swagelok valve on the manifold and the Swagelok valve on the water precursor was leak tested using a temporary tube to the Schlenk line. After vacuum was established, with the manifold being actively pumped on by the Schlenk line and the Swagelok valve to the water precursor still closed a liquid nitrogen bath froze the water precursor. Once fully frozen (~30 min), the water precursor was pumped on by opening the Swagelok valve to vacuum. After fully pumping down, the water

precursor was thawed with the Swagelok valve closed and this process was continued for a total of 4 FPTs.

The titanium precursor was *tetrakis*(ethylmethylamino)titanium(IV) (TEMATi, Strem, >99% purity) and was loaded in the recirculating glovebox due to its pyrophoric nature. With the Swagelok valve already connected to the precursor container, the TEMATi was pipette transferred into the precursor container. Once fully transferred, the container was sealed and attached to the two-way pneumatic Swagelok valve adjacent to the water precursor and degassed via freeze-pump-thawing.

Following loading and degassing, the TEMATi precursor vessel was wrapped with heating tape, as detailed below. The water precursor was not initially wrapped with heating tape until later commissioning experiments that ultimately followed the same wrapping protocol as the TEMATi precursor vessel.

4.4 Heat Tape Wrapping

Fiber glass heating tape (BriskHeat Heavy Insulated Heating Tapes, part number BIH051020L for the 105 W tapes that are 0.5″ wide and 2′ long, and part number BIH051040L for the 210 W tapes that are 0.5″ wide and 4′ long) and K-type thermocouples (Nextel ceramic braid insulation, Omega Engineering, spot welded in house) that were positioned at the center of each heating tape zone were employed to maintain ALD heating temperatures. Temperature controllers (Love 32B, Dwyer Instruments, Michigan City, IN) recorded temperatures and an in-house-written LabVIEW program interfaced with the temperature controllers for conducting temperature profiles and recording temperature data. Importantly, the 32B unit can control a heater either by a +10 V_{DC} pulse out (that is designed to be compatible with solid-state relay switches) *or* an integrated mechanical relay switch that can switch up to 3 A or a 360 W (on 120 V_{AC} line voltage) heater that is connected to line voltage. The specific temperature controllers under use had been previously employed as controllers for round-bottom-flask heaters that utilized the built-in relay. However, many of these relays had since broken and the controllers themselves were largely unused. We rehabilitiated these units and included Crydom CX240D5 5 A solid-state relays (part number CC1063-ND at DigiKey) that are compatible with the +10 V_{DC} pulse out from the Love 32B controller, and can switch up to 600 W of heater power (again assuming the heater is powered by 120 V_{AC} line voltage).

Heat tape wrapping of the ALD manifold, down tube, and precursor containers was done by wrapping either 2′ or 4′ lengths of heating tape around the metal components. A K-type thermocouple was placed near the heating tape on a larger piece of metal and held in place with copper wire. Care was taken to evenly wrap the tape and not overlap it. Copper wires held the heating tape in place. Once wrapped with heating tape, fiber quartz was

generously wrapped around any visible metal. The fiber quartz was then tightly wrapped in aluminum foil.

Heat tape wrapping of the manifold and down tube preceded mounting, while wrapping of the precursors took place after mounting. The precursor tube wrapping occurred in such a way to enable straightforward unwrapping for future reloading or exchange of precursor chemicals.

4.4.1 Reactor Furnace

The reactor was heated by a furnace which utilized a horizontally mounted 5-cm-I.D. tube furnace that was constructed from two semicircular ceramic heaters (CRFC-series, Omega Engineering, Norwalk, CT). The bottom ceramic heater rested on a clamp and the top ceramic heater rested on the bottom heater and was chained in place during depositions.

A temperature controller (Love 32B, Dwyer Instruments, Michigan City, IN) recorded temperatures at a K-type thermocouple (Nextel ceramic braid insulation, Omega Engineering, spot welded in house) that were positioned at the center of the reactor. An in-house-written LabVIEW program interfaced with the temperature controller for conducting temperature profiles and recording temperature data.

The glass reactor protruded from the furnace at either circular opening so that both elbows cleared the ends and were able to be connected to the ALD for flow. The elbow on the left, which was connected to the down tube was fully wrapped with heating tape, fiber quartz, and foil. The elbow on the right was not wrapped.

4.5 Commissioning

Several experiments were undertaken in commissioning the ALD. Each experiment was conducted using the standard operating procedures (SOPs) outlined in Appendix C. Commissioning experiments were optimized to ascertain several factors. The commissioning experiments were designed to determine whether deposition was occurring with linearity between different amounts of cycles and whether that linearity met a generally expected thickness. We believe that one cycle would be equal to ~1 Å of TiO_2 and use this metric as a general estimate of film thickness based upon cycle amount.[64,71]

Table 4.1 details the temperatures of each component of the ALD set-up for each commissioning experiment and the flow of N_2 used during each experiment. The T_{Manifold} represents the temperature measured at the manifold, rather than the temperature the manifold was set to, as there was a ~50 °C difference between set temperatures and measured temperatures on the manifold due to thermocouple placement. T_{Water} and T_{TEMATi} represent

precursor temperatures while $T_{\text{Down Tube}}$ represents the temperature of the flexible, stainless-steel tube connected to the manifold by a union elbow as described above. The T_{Reactor} is the temperature measured inside the reactor furnace with the thermocouple touching the glass of the reactor for most accurate temperature control.

In conducting commissioning experiments, each of the temperature values and flow values were varied to improve deposition and encourage the reaction between precursors to occur at the desired substrate. The first three commissioning experiments utilized 20 sccm flow, which equated to ~850 mtorr of pressure. We found little-to-no deposition for such high flow, and following the first three commissioning experiments we reduced the flow rate to 5 sccm for ~350 mtorr of UHP N_2 flow.[64] The next issue we addressed was reactor temperature, as XP spectra of ALD deposited TiO_2 on silicon oxide surfaces lacked linearity in terms of expected Ti:Si sensitivity-factor-corrected peak are ratios. We expected that Si signal would be linearly attenuated following additional cycles during deposition but were finding that there was no linearity. Table 4.2 addresses changes made to the number of cycles and the μpulses used in each cycle for each commissioning experiment. We present the commissioning experiments in terms of both the variables in Table 4.1 as well as the variables in Table 4.2. In addressing a lack of linearity in terms of Ti:Si signal in XPS between many cycles of depositions and fewer cycles, we varied both temperatures and μpulses. Flow remained at 5 sccm after the first three experiments and will not be discussed further.

Following changes to flow, we varied reactor temperatures and μpulses. During the fourth commissioning experiment through the eight we decreased the reactor temperature to 150 °C in the hopes that a lower temperature would facilitate adsorption of the precursors to the substrate. It was presently unclear whether a lack of linearity in terms of film thickness with varying cycle amounts was due to an initiation issue or due to TEMATi not sticking after a certain film thickness had been deposited. Additionally, we ascertained that it could be due to not enough TEMATi being released during μpulses. Therefore, also beginning during commissioning experiment 4, we increased the number of TEMATi μpulses to two. A typical μpulse as described by Table 4.2 is denoted by μpulses/length of μpulse (ms)/wait time between μpulses, with a 25 s wait between each pulse set of μpulses.

Despite these changes, XP spectra of commissioning experiments 4–8 did not show linearity in terms of Ti:Si intensity across different film thicknesses. In response to this issue, we increased the temperature of the TEMATi precursor to increase the amount of titanium present during deposition and increased the reactor and down tube temperatures back to ~175 °C to further encourage the reaction to occur. Following these changes, we observed excess TiO_2 depositing in both the right elbow of the reactor and the LN_2 cooled trap (Fig. 4.5K). This suggested that titanium precursor temperatures were not

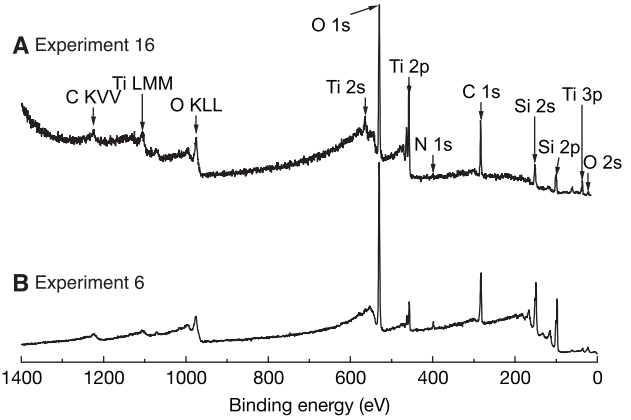

Figure 4.6 Representative XP spectra of a silicon oxide substrate with TiO_2 deposited from (**A**) ALD commissioning experiment 16 and (**B**) ALD commissioning experiment 6. Each feature is marked with an arrow. In some experiments where the precursors were not fully reacted nitrogen was present in the XP spectra of the resulting films as the TEMATi precursor contained both nitrogen and carbon.

to blame for the lack of linearity. In addition, increasing the amount of Ti precursor present during depositions resulted in the presence of unreacted TEMATi. This was observed in the XP spectra of Fig. 4.6B in the form of a visible N 1s feature. As the TEMATi precursor contains nitrogen, we expect that the presence of nitrogen in the XPS surveys suggests that there is unreacted Ti precursor.

This suggested to us that not enough water was making it to the substrate to react with the Ti precursor, so we decreased the number of Ti μpulses to be only one set of μpulses per cycle. We also wrapped the H_2O precursor with heating tape to increase the vapor pressure of the water. Heating the water precursor resulted in a large amount of condensed water in the LN_2 cooled trap, so water precursor heating temperatures were lowered.

Each of these optimizations resulted in eventual linearity of depositions. Figure 4.7 presents the representative O 1s, Ti 2p, N 1s, C 1s, and Si 2p3 X-ray photoelectron region of a silicon oxide substrate with ALD deposited TiO_2 following these commissioning experiments. We believe that this representative XP spectra demonstrates successful deposition after tuning specific aspects of the deposition set-up. Figure 4.7 normalizes the spectra between frames based on the cumulative area of all presented features.

The oxygen region of the spectrum demonstrated a doublet in which we ascribe the lower binding energy feature at ~530 eV in the O 1s region to metallic oxides. The higher binding energy feature in the O 1s region is likely dominated by the surface hydroxyl groups, –OH, that reports assign

Table 4.1 ALD Commissioning Experiments: Temperature and Flow. All temperatures in °C

Commissioning Experiment	T_{Manifold}	T_{water}	T_{TEMATi}	$T_{\text{Down Tube}}$	T_{Reactor}	N_2 Flow Rate (sccm)
1	140	0	75	150	175	20
2	140	0	75	150	175	20
3	140	0	75	150	175	20
4	140	0	75	150	175	5
5	140	0	75	150	175	5
6	140	0	75	150	175	5
7	140	0	75	150	175	5
8	140	0	75	150	175	5
9	195	0	100	175	175	5
10	195	0	100	175	175	5
11	195	0	100	175	175	5
12	195	0	125	175	0	5
13	195	0	110	150	150	5
14	195	0	110	150	150	5
15	195	80	115	175	175	5
16	195	50	115	175	175	5

Table 4.2 ALD Commissioning Experiments: Cycles and Pulses [a]

Commissioning Experiment	Total Cycles	1st TEMATi Pulse	2nd TEMATi Pulse	H_2O Pulse
1	10	3/100/900	*n/a*	3/10/90
2	20	3/100/900	*n/a*	3/10/90
3	1500	3/100/900	*n/a*	3/10/90
4	30	5/200/800	5/200/800	3/10/90
5	100	5/200/800	5/200/800	3/10/90
6	100	5/200/800	5/200/800	5/20/180
7	100	5/200/800	5/200/800	5/20/180
8	200	5/200/800	5/200/800	5/20/180
9	20	5/250/750	5/250/750	5/20/180
10	100	5/250/750	5/250/750	5/20/180
11	10	5/20/180	5/20/180	3/20/980
12	10	5/20/180	5/20/180	3/20/980
13	10	5/20/180	5/20/180	3/20/980
14	20	5/20/480	5/20/480	3/20/980
15	20	5/20/480	*n/a*	3/20/980
16	10	3/20/980	*n/a*	2/20/980

[a] A complete pulse is represented by number of μpulses/length of μpulse (ms)/wait time between *mu* pulses (ms). A second pulse of TEMATi was optionally used or excluded, *n/a* denotes the use of only one pulse of TEMATi.

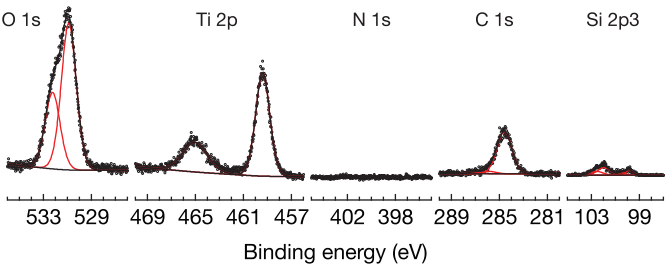

Figure 4.7 Representative XP spectra of a silicon oxide substrate with TiO_2 deposited onto it. The spectra shown in the figure is from commissioning experiment 16. Si $2p_{3/2}$ intensity is attenuated due to the TiO_2 layer as expected. The lack of signal in the N 1s region suggests full conversion of the TEMATi precursor to TiO_2. The total *y*-axis amplitude of photoelectron counts is normalized between each frame.

as 532.9 eV for titanium hydroxide[30] but may contain trace contributions of adventitious, oxidized contaminants as well. One doublet describes well the Ti 2p region throughout all samples studied that we ascribe to Ti^{4+} with Ti $2p_{3/2}$ at ~459 eV and Ti $2p_{1/2}$ at ~465 eV. In the representative spectra of Fig. 4.7, the N 1s region shows no observable nitrogen signal, suggesting that all of the TEMATi precursor has reacted to form TiO_2. In some samples, the N 1s region contained one feature which we attribute to unreacted TEMATi caused by not enough water, reactor temperatures that were too low, or TEMATi precursor temperatures that were too low. Contributions to the C 1s region include adventitiously adsorbed species at ~285 eV as well as features toward higher binding energy that would indicate oxidized adventitious contamination. The Si $2p_{3/2}$ region is well described by two doublets which indicates the presence of silicon oxides. It is difficult to deconvolve which of those oxides belong to the silicon oxide grown in by piranha etching prior to ALD and oxides which belong to TiO_2 bound to silicon.

The representative XP spectra presented in Fig. 4.7 are from the 10-cycle 16^{th} commissioning experiment. Expecting that one cycle deposits ~1 Å of TiO_2 we believe that 10 cycles yields ~1 nm of TiO_2 and believe that the Si $2p_{3/2}$ signal is attenuated linearly with the thickness of the TiO_2 film.

4.6 Conclusion

We developed and tested a Schlenk-line integrated ALD for deposition of metal oxides for passivation of various substrates. We proved the success of this concept by deposition onto silicon oxide surfaces and quantified film thicknesses and successful deposition via X-ray photoelectron spectroscopy. This proof of concept for a successful Schlenk-line integrated ALD provides a potential route for the passivation of air-sensitive materials by metal oxides.

CHAPTER 5

SURFACE CHEMISTRY, PASSIVATION, AND STABILITY, OF CESIUM TITANIUM(IV) BROMIDE THIN FILMS PASSIVATED BY ATOMIC-LAYER-DEPOSITED TITANIUM(IV) OXIDE

Abstract

Conflicting reports on Cs_2TiBr_6 stability suggest a need for passivation against oxidation. Here, we synthesize Cs_2TiBr_6 thin films by spin coating a CsBr layer and a subsequent reaction with $TiBr_4$ vapor. Following synthesis, we deposited TiO_2 by atomic layer deposition onto the subsequent Cs_2TiBr_6 films using an in-house developed, Schlenk-line integrated ALD instrument. X-ray photoelectron spectroscopy (XPS) quantified surface chemical species and X-ray diffraction (XRD) established successful synthesis. Presently, we were unsuccessful in fully converting the CsBr starting material to Cs_2TiBr_6 in our experimental set-up, which merits further study. We discuss the implications of these surface chemical and stability results on device relevant Cs_2TiBr_6 films for photovoltaics.

5.1 Introduction

Studies of large-grain Cs_2TiBr_6 suggested rapid oxidation in an air ambient.[26] Conflicting reports about the stabilities of powdered and thin film Cs_2TiBr_6 motivated us to further study this solar-energy conversion material due to promising preliminary PV results.[24,44] Given these stability issues, we were motivated to study the passivation of a more device relevant form of Cs_2TiBr_6 via atomic layer deposition. Atomic layer deposition has been demonstrated to improve stability and provide carrier transport in perovskite PV devices. These passivation studies present an opportunity to further improve Cs_2TiBr_6 as a PV material.[32,64,68] However, traditional atomic layer deposition does not lend itself to air-free sample transfer. In Chapter 4 we developed and fabricated a Schlenk-line integrated ALD for air-free sample transfer and passivation with metal oxides. Based upon these promising PV results, promising passivation results of other PV materials, and proof of concept of a Schlenk-line integrated ALD we aimed to synthesize high quality, thin film Cs_2TiBr_6 material and study passivation using of the resulting material to elucidate the interfacial chemistry and stability of the material.

Herein, we synthesize thin film Cs_2TiBr_6 from a reaction of $TiBr_4$ vapor with spin and drop deposited CsBr thin films on FTO substrates and characterize surface species, stability and passivation. We explore multiple methods to optimize synthesis including optimization of CsBr thin film deposition and multiple reaction set-ups to improve reaction between the $TiBr_4$ vapor and the CsBr films. X-ray diffraction (XRD) quantifies conversion of the CsBr starting material to the desired thin films of Cs_2TiBr_6. Photoelectron spectroscopies quantify chemical structures as a function of thin film preparation. X-ray photoelectron spectroscopy (XPS) ascertains chemical states and relative stoichiometries of near-interfacial species. Atomic layer deposition (ALD) attempts to passivate Cs_2TiBr_6 thin films. With these studies, we aim to elucidate the effects of interfacial chemical states and atmospheric stability on the properties of this solar-relevant material.

5.2 Experimental

5.2.1 Materials and Chemicals

All chemicals were used as received unless otherwise noted. Chemicals used in the synthesis of cesium titanium bromide thin films included cesium bromide (CsBr, 99.9% trace metals basis, Sigma Aldrich), and titanium(IV) bromide ($TiBr_4$, 98%, Sigma Aldrich) that was further purified by sublimation. TiO_2 and CsBr thin films were deposited on fluorine-doped tin oxide (FTO)/glass slides with a surface resistivity of ~7 Ω sq^{-1} (Sigma-Aldrich). Chemicals employed in the deposition of TiO_2 thin films on FTO include titanium(diisopropoxide)-*bis*-(2,4-pentanedionate) (75% in iso-

propanol, Alfa Aesar) and *n*-butanol (99.5%, Acros Organics) to form 0.15 and 0.30 M solutions. Precursors for atomic layer deposition (ALD) included tetrakis(ethylmethylamino)titanium(IV) (TEMATi, Strem, >99% purity), and DI water. Both precursors were freeze pump thawed before use. A Milli–Q filtration system provided all water at 18 MΩ cm resistivity (Millipore).

5.2.2 Cs_2TiBr_6 Thin Film Synthesis Optimization

Cs_2TiBr_6 thin films were synthesized by reacting $TiBr_4$ vapor with CsBr thin films on FTO substrates in inert atmospheres. Three different experimental set-ups were attempted during the synthesis optimization of the Cs_2TiBr_6 thin films. In addition to these differing experimental set-ups, deposition of TiO_2 onto the FTO substrates prior to CsBr thin film deposition was undertaken on some samples to provide both an electron transport layer for the Cs_2TiBr_6 thin films and to improve the "stickiness" of the metal oxide substrate for CsBr deposition. CsBr thin film deposition protocols were modified to improve uniformity and vary film thickness. $TiBr_4$ precursor loadings were also varied to improve the subsequent reactions with the CsBr films. Temperatures and reaction durations were also varied during the optimization of Cs_2TiBr_6 thin film synthesis. Herein, we present each of these variables for optimizing the synthesis of Cs_2TiBr_6 thin films.

5.2.2.1 TiO_2 Deposition on FTO Substrates The deposition of TiO_2 films onto FTO-coated slides is previously described.[28] In brief, FTO-coated glass slides were initially rinsed with water and dried before sequential sonication in acetone, isopropyl alcohol (IPA), and H_2O, dried in argon, and further dried in a 100 °C oven. Prior to the deposition, one edge of each FTO slide was covered with Kapton tape to leave an exposed, conductive edge for XPS and electrochemical characterization. For deposition of TiO_2, each FTO slide was initially covered with a 0.15 M titanium precursor solution, spun at 3000 rpm for 25 s, and then dried on a hot plate that was set to 100 °C under an air ambient. After a short period of cooling, the 0.30 M titanium precursor solution was spun onto the surface in the same fashion and dried on the hot plate. The Kapton tape was removed after the 0.30 M precursor dried. The compact TiO_2 films were directly annealed in a furnace at 500 °C for a minimum of 2 h to form the anatase phase and subsequently stored in plastic centrifuge tubes until CsBr film deposition.

5.2.2.2 Optimization of CsBr Deposition CsBr thin films deposited onto FTO slides either had or did not have TiO_2 deposited onto them. Similar to FTO slides prepared for TiO_2 deposition one edge of each FTO slide was covered with Kapton tape to leave an exposed, conductive edge for XPS and electrochemical characterization prior to spin coating. On substrates that already contained a TiO_2 layer, the Kapton tape was stuck to the same spot that it had been during TiO_2 deposition to leave an exposed section of FTO.

Table 5.1 Solvents and Concentrations of CsBr for CsBr Deposition Precursors

Solvent (ratio)	Precursor Concentration(s)
Water	1 M
Water:ethanol (1:5)	0.3 M
Water:ethanol (2:5)	0.6 M
Ethylene glycol	Saturated
Water:ethylene glycol (1:1)	1 M, 1.5 M, Saturated

Generally, CsBr spin deposition utilized a spin coater on the lab bench under an air ambient. The FTO slide was placed into the spin coater and suctioned to the stage using house vacuum. The spin coater was programmed with a spin speed, duration, and acceleration. The "A" key on the spin coater determined spin speed, the "B" key determined spin duration, and the "C" key determined spin acceleration. All numbers were locked in by hitting the pound key. The "A" key was hit twice to initiate the spin program. Once a spin program was input and the slide was suctioned to the spin stage by house vacuum, a 1 mL syringe with a hypodermic needle deposited enough drops of the CsBr precursor onto the FTO slide to cover the whole slide. "AA" was then whacked to initiate spinning and the lid was placed on the instrument. After spinning, vacuum was released, the slide was moved to a ~125 °C hot plate and dried under an air ambient. In some protocols, subsequent depositions were employed and followed the same steps. After all depositions were complete the Kapton tape was removed, and samples were either stored until reaction with $TiBr_4$ or were annealed in a two-zone tube furnace.

CsBr spin deposition was optimized by tuning several variables: precursor solvents and concentrations, spin speed, duration and acceleration, and annealing. Precursor solvents and concentrations were first varied. Table 5.1 shows each precursor solvent and CsBr concentration employed.

The first solvent considered was water, as CsBr is very soluble in water. Next, ethanol was considered, however, CsBr is so sparingly soluble in ethanol that it was not a viable option. Two mixtures of water and ethanol were attempted to improve CsBr solubility and speed up evaporation times. These mixtures included a 1:5 ratio and a 2:5 ratio of water:ethanol. Next, ethylene glycol was tried as a solvent. Mixtures of water and ethylene glycol were also considered in a 1:1 ratio.

Concentrations of CsBr were somewhat dependent on its solubility, with solutions ranging from ~0.3 M to saturated. Next, spin speed, duration, and acceleration were varied. Spin speed ranged between 1000–4000 rpm, duration varied from 25–120 seconds, and acceleration values ranged from

100–1000 rpm s^{-1}. Finally, annealing at 500 °C was attempted on some samples, but showed no difference upon visual inspection and is not considered further.

CsBr spin deposition was either done once or twice, depending on desired film thickness. Some CsBr depositions were conducted by drop coating the CsBr precursor onto the surface of the FTO slide while the slide was sitting on a ~125 °C hot plate under an air ambient. For these depositions, the solvent was allowed to completely evaporate following application of the precursor. These depositions were either done with one or two coats as well and utilized varying solvents of varying concentrations.

5.2.2.3 Cs_2TiBr_6 Thin Film Synthesis: Reactor Optimization Three experimental set-ups were employed to react $TiBr_4$ vapor with CsBr thin films. The first of these three set-ups utilized a large sublimator and a petri dish. In the recirculating glovebox, the FTO slides with CsBr thin films were carbon taped to the inside of a 60 mm petri dish lid so that if the lid was covering a petri dish the CsBr film would be upside-down, facing the bottom petri dish. The petri dish itself was loaded with 100–250 mg of $TiBr_4$ and the lid with the CsBr slide was placed over the $TiBr_4$. This "closed" petri dish was placed in the bottom of the sublimator and the sublimator was sealed. The sublimator with the CsBr film and $TiBr_4$ powder in the petri dish were transferred to an oil bath so that the sublimator was submerged in oil up to the cold finger. The sublimator was then connected to the Schlenk line and evacuated. Following evacuation, the oil bath was heated to ~150 °C (oil bath maximum temperature: 200 °C). Two protocols were attempted, one where the sublimator was actively pumped on for the duration of the $TiBr_4$ reaction with the CsBr film, and one where the sublimator was held under passive vacuum during the reaction. Neither of these two methods were successful in effecting a reaction between the CsBr film and the $TiBr_4$ vapor and therefore this set-up is not considered further.

The second experimental set-up that was attempted utilized a 15 mL pressure vessel and a sand bath for reactions. This allowed for longer reaction durations and higher reaction temperatures than the oil bath. CsBr films deposited onto FTO slides were added to a clean, dry 15 mL pressure vessel with ~100–250 mg of $TiBr_4$ in the flush box. Care was taken to include less $TiBr_4$ than the pressure tolerance of the pressure vessels as the reaction occurs with vapor phase $TiBr_4$. The CsBr films and the $TiBr_4$ powder were sealed in the pressure vessel under nitrogen in the flush box with a Teflon cap and a Viton gasket. The pressure vessel was transferred from the flush box and placed in a sand bath on a hot plate. For improved temperature control, the sand bath was wrapped with fiber quartz and aluminum foil. A temperature probe was placed halfway into the sand bath to measure and control the temperature during the reaction. The pressure vessel was placed 3/4 of the way into the sand bath, with the cap sticking out. The cap was wrapped with fiber quartz

and foil to keep the reaction at a constant temperature. This set-up had issues with temperature control, which facilitated the use of a third synthetic set-up.

The third experimental set-up attempted for the reaction of CsBr thin films on FTO substrates with $TiBr_4$ vapor to form Cs_2TiBr_6 thin films also utilized a 15 mL pressure vessel. The pressure vessel was loaded and sealed in the flush box, similar to the second set-up. However, once sealed, the pressure vessel was transferred to a two-zone tube furnace. Section §2.2.2 provides details about the two-zone tube furnaces utilized for these reactions. The pressure vessel was wrapped in fiber quartz prior to loading in the tube furnace. This was done mostly to ensure that if the pressure vessel blew out, that the corrosive $TiBr_4$ would be contained within the fiber quartz. The wrapped pressure vessel with the reactants was placed into the tube furnace so that the CsBr coated FTO slides were facing the front end and the Teflon cap was facing the back end. Figure 2.2A details a typical set-up in a two-zone tube furnace, the fiber quartz plug that enables a tilt (Fig. 2.2A) was not utilized for this particular set-up. An additional thermocouple was placed against the pressure vessel glass inside of the fiber quartz. This thermocouple was used to measure the temperature within the fiber quartz, which was about ~20 °C hotter than the temperature measured by the front-end thermocouple.

5.2.2.4 Cs_2TiBr_6 Thin Film Synthesis: Temperature Program Optimization

Temperature programs were considered with each of the three experimental set-ups. There were temperature limitations with the first two set-ups, but no temperature limitations with the third set-up. Thin films synthesized by the Padture group employed an "annealing" step for their CsBr films in $TiBr_4$ vapor to synthesize Cs_2TiBr_6.[24] This set-up utilized temperatures between 150–230 °C and the group found highest quality films from ~200 °C heating temperatures for a 24 h reaction. We considered these results when optimizing the temperature programs of Cs_2TiBr_6 thin-film synthesis.

The oil bath used in the first set-up had temperature stabilities of ~200 °C, but to err on the side of caution, temperatures utilized during this set-up did not exceed ~180 °C. In the first set-up, two temperature programs were attempted. In the first temperature program, the oil bath was immediately ramped to the heating temperature ~150 °C and held for 12–24 hours while the sublimator was either actively pumped on or under passive vacuum. In the second temperature program, the sublimator was slowly ramped to the heating temperature for 3 hours and then passively pumped on while at heating temperatures for 12–24 h.

In the second set-up, a sand bath heated the reaction vessel containing the CsBr substrate and the $TiBr_4$ powder. The sand bath had less temperature limitations than the oil bath, but still did not exceed ~250 °C due to limitations at the hot plate. In addition, the sand bath had difficulty heating quickly to heating temperatures. For temperature programs utilizing the second set-up

with the sand bath and the pressure vessel, the sand bath was ramped to ~170-250 °C for 2 h and held at heating temperatures for 24–72 h.

In the third set-up, the reaction vessel was placed into a two-zone tube furnace. A LabVIEW temperature program controlled this tube furnace. Temperature programs used in the third set-up were similar to those used for synthesis of large-grain Cs_2TiBr_6, however they differed in temperatures and durations. Heating temperatures utilized in the third set-up were ~200 °C at the front thermocouple and ~220 °C for the back thermocouple during the soak step. However, the fiber quartz wrapping was established by a third thermocouple to make the tube ~20 °C hotter than the temperature measured by the front-end thermocouple. The duration of ramping to the heating temperature only ranged from 1–5 hours. The soak step ranged from 12–72 hours and the cooling step ranged from 2–15 hours. A getter step was included in the cool down step of some of the temperature programs to getter any unreacted $TiBr_4$ vapor towards the pressure vessel cap so that the $TiBr_4$ would not recrystallize on the thin films at the front end.

5.2.3 Cs_2TiBr_6 Thin Film Characterization

All characterization methods to study the surface chemistry, stability, and properties of resulting Cs_2TiBr_6 thin films are detailed in full in §A.1 within Appendix A. The following sections detail each characterization method in brief.

5.2.3.1 X-ray diffraction A Bruker-AXS D8 focus powder X-ray diffractometer with Cu Kα_1 radiation collected X-ray diffraction (XRD) data in the range of 10–45° (2θ) on samples mounted in the recirculating glovebox and isolated from air with low-static Kapton.

5.2.3.2 Photoelectron Spectroscopy A PHI 5600 multitechnique system acquired all X-ray photoelectron and ultraviolet photoelectron spectra as described previously.[19−−22] The apparent rapid oxidation of the material necessitated a vacuum suitcase (Transfer Engineering and Manufacturing, Inc., Fremont, CA) for air-free transfer of puck-mounted Cs_2TiBr_6 samples from a recirculating glovebox to the instrument. Peak quantification utilized an in-house-developed LabVIEW program based on published spectral shapes and corrected for instrument-specific sensitivity factors[31,47] and background energy loss functions.[48–50] For ultraviolet photo-electron spectroscopy, a gas discharge lamp (UVS 40A2, Prevac, Rogów, Poland) generated the He I spectroscopic line, $\mathbf{E}_{\mathrm{He\,I}} = h\nu = 21.218$ eV. We report sample work function values, ϕ, as the difference between $\mathbf{E}_{\mathrm{He\,I}}$ and the secondary electron cutoff energy, or $\phi = \mathbf{E}_{\mathrm{He\,I}} - \mathbf{E}_{\mathrm{SEC}}$. We report Fermi- level energies relative to valence band maximum energies, or $\mathbf{E}_{\mathrm{F}} - \mathbf{E}_{\mathrm{VBM}}$.

5.2.3.3 UV-Vis Spectroscopy A UV–visible spectrometer (Evolution 300, Thermo Fisher Scientific, Waltham, MA) collected scattered light from Cs_2TiBr_6

samples mounted in a Praying Mantis diffuse reflection accessory (Harrick Scientific Products, Pleasantville, NY) and isolated from the air ambient with Kapton tape.

5.2.4 Atomic Layer Deposition of TiO_2 onto Cs_2TiBr_6 Thin Films

Cs_2TiBr_6 thin films on FTO substrates were loaded into the ALD reactor in the recirculating glovebox following generally the same loading protocol as employed during air stable commissioning experiments. In brief, two Cs_2TiBr_6 thin films were placed into the reactor using tweezers. One thin film was placed at the front end of the reactor and the other film was placed at the back end. Once inside the reactor, the elbow joints with vacuum grease were carefully placed into the 24/40 T joint and rotated. Care was taken to not rotate the reactor itself and just rotate the elbows so as the keep the Cs_2TiBr_6 films facing upwards. Once sealed, two plastic joint clips fastened the elbows to the reactor. The stopcocks on either elbow were closed and the reactor was connected to the ALD.

The reactor was evacuated once it had been fully connected to the instrument. The front elbow was wrapped with the heating tape, fiber quartz, and foil. The reactor furnace was closed and sealed and the ALD running temperatures were set. For preliminary studies we employed reactor temperatures of 175 °C with the down tube also equilibrated at 175 °C. The manifold, water precursor, and TEMATi precursor were set to 140 °C, 50 °C, and 115 °C respectively. A UHP nitrogen flow of 5 sccm resulting in pressures of ~380 mtorr and an initial wait of 30 min allowed for temperature equilibration. For the depositions, 10 cycles with one Ti pulse (3 μpulses / 20 ms open / 980 ms delay between each μpulse) and one water pulse (2/20/980) and a 25 s wait between each pulse effected ~1 nm of TiO_2 on the Cs_2TiBr_6 surfaces. The resulting films were transferred via the reactor to the recirculating glovebox directly following deposition and stored until further characterization.

5.3 Results

5.3.1 Properties and Characterization of CsBr Thin Films

The optimization of CsBr thin films remains an area of continued exploration. In each deposition employed, FTO substrates with CsBr films appeared a semi-transparent milky white color. Uniform films had consistent color and transparency across the whole slide, while films that lacked uniformly were filled with gaps and concentrated areas of CsBr. SEM imaging of CsBr thin films to establish film thickness, surface morphology, and uniformity was unsuccessful due to the insulating nature of the films that created instrumental charging resulting in blurry images. We therefore only examined CsBr films qualitatively in terms of visual appearance.

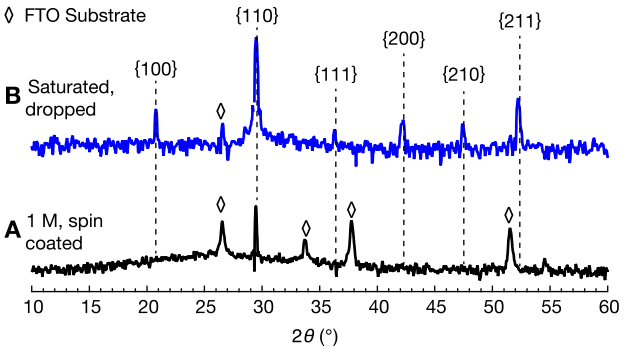

Figure 5.1 Representative XRD traces for CsBr thin films on FTO prepared by (**A**) spin coating and (**B**) drop coating. FTO substrate features are denoted as ◇. The spin coated film (**A**) utilized a 1 M CsBr precursor solution while the film that was drop coated employed a saturated CsBr solution.

Based on visual observations we found that films deposited using saturated solutions with either a 1:1 mixture of water and ethylene glycol or entirely ethylene glycol are most uniform. We have also found that employing multiple deposition steps resulted in more uniform films, with subsequent depositions filling gaps in films and increasing film thickness. Films deposited using solutions with concentrations less than 1 M had visible gaps in CsBr coverage. Additionally, films deposited using mixtures of ethanol and water evaporated too quickly for uniform crystallization to occur. A 24 h annealing at 500 °C was attempted to improve uniformity but, in our hands, did not visually change the morphology of the surfaces.

After establishing ideal precursor solvents and concentrations, deposition protocols were varied. Figure 5.1 shows X-ray diffraction traces of two CsBr films. The film in trace A was deposited by spinning a 1 M CsBr solution in 1:1 water and ethylene glycol at 4000 rpm for 25 s with a 500-rpm-s^{-1} acceleration. This film possessed only the CsBr(110) reflection. The film in trace B was deposited by drop coating the FTO substrate with a saturated CsBr solution in 1:1 water and ethylene glycol. This film has many more CsBr reflections and was much thicker than the film from trace A. CsBr reflections other than the CsBr(110) reflection in trace B do not necessarily suggest a better film, just one with multiple facets of polycrystalline CsBr.

CsBr film deposition remains an area of active study, but based upon preliminary visual observations, films that are deposited by spin coating look more uniform and are not as thick. Film thickness is an issue that we address in the following sections, as full conversion of CsBr to Cs_2TiBr_6 is necessary for optimized Cs_2TiBr_6 films. SEM studies would be incredibly useful in solving the issue of film morphology and uniformity of CsBr thin films, however

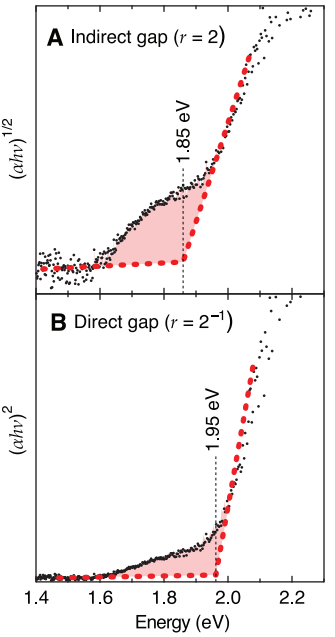

Figure 5.2 UV-Vis data plotted as $(\alpha h\nu)^{1/r}$ vs energy Tauc plots for thin-flim Cs_2TiBr_6 showing (**A**) the indirect band gap of the material at 1.85 eV for $r = 2$, and (**B**) the direct band gap of the material at 1.95 eV when $r = 2^{-1}$. The red shaded areas underneath each plot most likely represents an Urbach tail.

the charging of CsBr surfaces would need to be addressed in order to get well-resolved images.

5.3.2 Properties of Cs_2TiBr_6 Thin Films

As synthesized from a 24–72 hour anneal in the third experimental set-up detailed in the experimental section of this chapter, thin films appeared dark red. Extrapolations in Fig. 5.2, respectively, indicate the indirect and direct forbidden energy gaps of 1.85 and 1.95 eV for the dark-red, thin film Cs_2TiBr_6 material under study. We attribute the shaded region of the figure between the two linear fits to an Urbach tail, which merits further investigation.[72] While slightly higher, the calculated indirect and direct forbidden energy gaps agree well with early reports of 1.8 eV band gaps for thin film Cs_2TiBr_6, and is logical given the red color of the resulting films.[24–25] All UV–Vis data collection utilized samples that were isolated from an air ambient by Kapton tape.

Qualitatively, thin film samples appeared to have higher ambient stability than large-grain Cs_2TiBr_6. Thin film samples began to appear wet and white

within one hour of air exposure. This demonstrates higher stability than large-grain samples which within minutes following exposure to ambient air become wet and lighten in color. Unfortunately, due to instrumental limitations, a quantitative analysis of ambient atmospheric stability of the resulting Cs_2TiBr_6 films using X-ray diffraction was not possible but would be merited. Observations of both large-grain and thin film material suggest that it is hygroscopic and air sensitive. Interestingly, thin film Cs_2TiBr_6 began to have pinholes within 1 h of air exposure.

5.4 Characterization of Optimized Cs_2TiBr_6 Thin Films

We found that none of the three reaction set-ups were successful in fully converting the CsBr starting material to Cs_2TiBr_6, as quantified by XRD. Ideally, a successful synthesis would be one which fully converts the CsBr thin film to Cs_2TiBr_6, however, in our hands this was not possible. Therefore, we considered a successful set-up as one which had uniform temperature control and one which converted the largest quantity of the CsBr starting material to Cs_2TiBr_6. Herein we present both the qualitative and quantitative methods undertaken to optimize the synthesis of and characterize Cs_2TiBr_6 thin films.

Qualitatively, we observed each reaction set-up following heating, and suspect the limited conversion of CsBr to Cs_2TiBr_6 in the first and second reaction set-ups was due to cold spots that drew $TiBr_4$ vapor away from the FTO substrates. In the first reaction set-up, active pumping with the Schlenk line resulted in rapid trapping of $TiBr_4$ in the trap on the Schlenk line. This suggested that $TiBr_4$ was being pumped away too quickly to react with the CsBr surfaces. To amend this, we used passive vacuum in a second iteration of the first reaction set-up in the sublimator but $TiBr_4$ tended to recrystallize on the sides of the sublimator away from the substrate. In further promoting collisions of $TiBr_4$ with the CsBr films, we employed the second set-up which used a pressure vessel of a much smaller volume with much better temperature control in the form of a sand bath. However, following these syntheses, $TiBr_4$ was visible in the threading of the vessel at the opening, suggesting $TiBr_4$ vapor was trying to escape the vessel through the top, which was opposite the substrates at the bottom of the vessel. This suggested that the top of the vessel was colder than the bottom and was effectively gettering the $TiBr_4$ vapor away from the substrates at the bottom before conversion from CsBr to Cs_2TiBr_6 could occur. To ameliorate this, the third reaction set-up utilized a two-zone tube furnace for optimal temperature control to encourage $TiBr_4$ vapor to react with the CsBr substrates and not escape the vessel. This set-up resulted in reaction vessels that had crystallized $TiBr_4$ near the substrates, which suggests that the $TiBr_4$ vapor was near the CsBr substrates but presents further issues in terms of $TiBr_4$ contamination on Cs_2TiBr_6 films, which we considered in depth during studies of large-grain Cs_2TiBr_6 in Chapter 3.

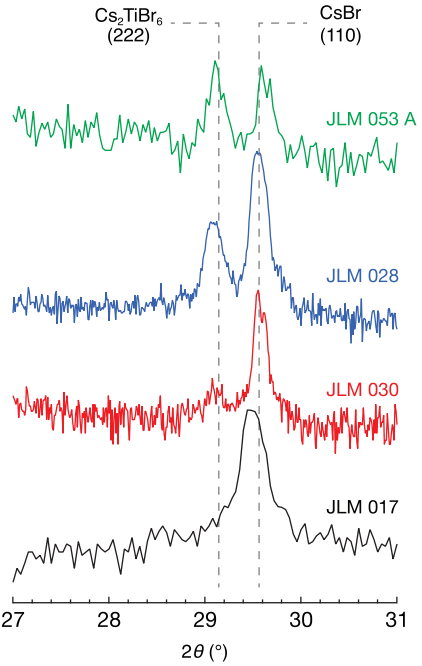

Figure 5.3 Representative XRD traces for CsBr (JLM 017, black trace) and Cs_2TiBr_6 (JLM 030, 028, and 053 A) thin films which were isolated from air by Kapton tape during analysis. CsBr(110) reflections at 28.9° dominate the CsBr and Cs_2TiBr_6 samples (JLM 030, red trace, and 028, blue trace) due to incomplete conversion of the CsBr starting material. As improved reaction set-ups allow for better reaction of $TiBr_4$ vapor with CsBr thin films, the CsBr(110) reflection diminishes in favor of a feature at 29.4° attributed to the Cs_2TiBr_6(222) reflection. However, the highest level of conversion we measured (JLM 053 A, green trace) still resulted in the presence of crystalline CsBr starting material, suggesting the reaction is not going to completion.

In a more quantitative approach to optimizing Cs_2TiBr_6 thin film reaction set-ups and reaction conditions, we collected XRD and photoelectron spectra of the resulting thin films. Conversion of the crystalline CsBr starting material to crystalline Cs_2TiBr_6 was first quantified by collecting XRD scans in a narrow range at 2θ angles of 28–30.5° to view both the Cs_2TiBr_6(222) and CsBr(110) reflections simultaneously.

Figure 5.3 illustrates representative diffraction traces of samples synthesized utilizing both the second and third reaction set-ups. We did not include XRD traces from Cs_2TiBr_6 thin films synthesized using the first set-up as it was unsuccessful in effecting an XRD detectable Cs_2TiBr_6(222) reflection.

In Fig. 5.3 a control sample was included (JLM 017). This control sample was a CsBr thin film that was excluded from air using Kapton tape to better

demonstrate the conversion of the CsBr starting material to Cs_2TiBr_6 under different reaction conditions in the other three traces. While each of the three Cs_2TiBr_6 films were synthesized using CsBr thin films that had been prepared using different deposition parameters, each CsBr thin film had characteristic CsBr(111) reflections which would not be affected by morphology or uniformity issues. Thus, when considering Fig. 5.3 we only consider conversion of the CsBr films and not the quality of the CsBr films themselves.

The traces labeled JLM 028 and JLM 030 utilized the second reaction set-up, in which a pressure vessel was heated in a sand bath. These traces both contained the Cs_2TiBr_6(222) and CsBr(110) reflections, however the CsBr(110) reflection was larger than the Cs_2TiBr_6(222) refection in both representative samples synthesized using the second reaction set-up. Interestingly, JLM 030 had much less detectable Cs_2TiBr_6(222) signal than JLM 028. This may be due to the fact that despite both reactions being set to a temperature of 250 °C, JLM 028 got up to 240 °C while JLM 030 did not exceed 230 °C. The lack of temperature control in the second set-up could be the reason for the lack of linearity between conversion of the starting materials.

The trace labeled JLM 053A utilized the third reaction set-up, which employed a pressure vessel for an inert reaction of vapor phase $TiBr_4$ with CsBr thin films on FTO substrates in the two-zone tube furnace. As shown in Fig. 5.3, JLM 053 A was most successful in converting the CsBr starting material to the desired Cs_2TiBr_6 product. The relative intensity of the Cs_2TiBr_6(222) reflection is the largest in this trace, and is barely detectable in JLM 030 and smaller than the CsBr(110) reflection in JLM 028. This suggests that temperature control is a large determining factor in successful conversion of the CsBr starting material to the desired Cs_2TiBr_6 crystalline product. Temperature control in the tube furnace was much more uniform than in the sand bath.

X-ray photoelectron spectra of the Cs_2TiBr_6 thin films was also collected to establish surface chemistry. Figure 5.4 presents the representative Cs $3d_{5/2}$, O 1s, Ti 2p, C 1s, and Br 3d X-ray photoelectron regions of several thin films. Thin films in Figure 5.4 include a (A) TiO_2 thin film on an FTO slide, (B) a CsBr thin film on a TiO_2 film on FTO, and (C) Cs_2TiBr_6 thin film on TiO_2 on FTO. While Fig. 24 only includes one representative spectra of a Cs_2TiBr_6 thin film, we observed similar stoichiometries of Cs:Ti:Br on thin films that possessed varying levels of starting material conversion because of the surface sensitivity of this technique. Figure 24 normalizes the spectra between frames based on the cumulative area of all presented features. The cesium region of the spectrum demonstrated a singular feature in frames B and C at ~723 eV that we ascribe to lattice Cs^+. As expected, the TiO_2 film in frame A demonstrated no observable cesium within detection limits. For frames A–C, we ascribe a feature at ~530 eV in the O 1s region to metallic oxides. The higher binding energy feature in each O 1s region is likely dominated by the surface hydroxyl groups, –OH, that reports assign as 532.9 eV for titanium

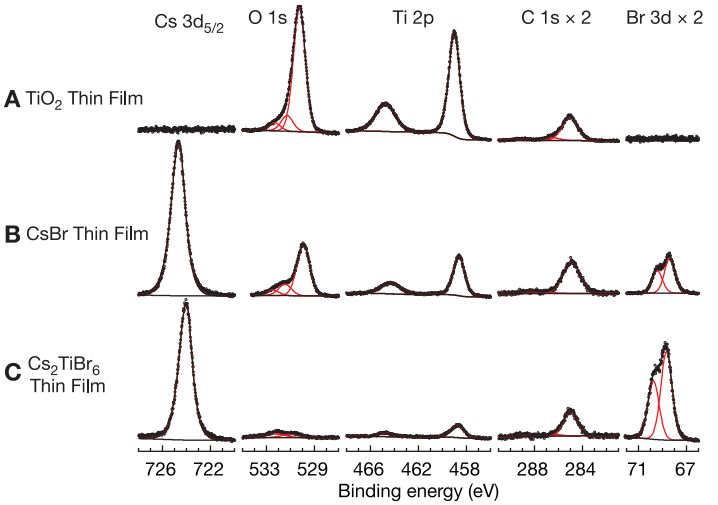

Figure 5.4 Representative XP spectra of (**A**) TiO_2, (**B**) CsBr on TiO_2, and (**C**) Cs_2TiBr_6 on TiO_2 thin films on FTO substrates. TiO_2 sample interfaces (**A**) demonstrate no observable cesium or bromine, which is expected for such surfaces. CsBr thin films (**B**) show highly attenuated O 1s and Ti 2p regions suggesting successful coverage and Cs_2TiBr_6 thin films (**C**) show little to no metal oxide contaminants, suggesting nearly oxide free interfaces contrary to the oxide dominate surfaces of large-grain Cs_2TiBr_6. The total y-axis amplitude of photoelectron counts is normalized between each frame with the C 1s, and Br 3d regions all magnified by 2× vs Cs $3d_{5/2}$, O 1s, and Ti 2p.

hydroxide[30] but may contain trace contributions of adventitious, oxidized contaminants as well. Interestingly, the O 1s spectra in trace C demonstrates very little metal oxide features which further supports findings of improved stability of thin films over large-grain material. One doublet describes well the Ti 2p region throughout all samples studied that we ascribe to Ti^{4+} with Ti $2p_{3/2}$ at ~459 eV and Ti $2p_{1/2}$ at ~465 eV. Both lattice and interfacial oxidized titanium likely contribute to the cumulative photoelectron signal and cannot be easily deconvolved for the similar 4+ oxidation state of each titanium species. Contributions to the C 1s region include adventitiously adsorbed species at ~285 eV as well as features toward higher binding energy that would indicate oxidized adventitious contamination. Br 3d is well described by a singular d-orbital doublet with Br $3d_{5/2}$ at ~69 eV for frames B and C.

Beyond the position of each representative spectral feature, the relative change in intensities yields significant insight into each surface composition. Table 5.2 displays sensitivity-factor-corrected peak area ratios for each Cs_2TiBr_6 surface under study that we normalize to Ti ≡ 1 for its contribution to the overall material stoichiometry. Each value in Table 5.2 represents the peak area ratios of the representative spectra in Fig. 5.4.

Table 5.2 XP Peak Area Ratios for Thin Film TiO_2, CsBr, and Cs_2TiBr_6 [a]

	Cs	Ti	Br
TiO_2 thin film	*n/a*	1	*n/a*
CsBr thin film	1.03	1	0.87
Cs_2TiBr_6 thin film	2.45	1	6.81

[a] We consider sensitivity-factor-corrected peak area ratios in the context of the Cs:Ti:Br stoichiometry and normalize to Ti ≡ 1 based on the Cs_2TiBr_6 stoichiometry.

As expected, the TiO_2 thin film peak area ratios of Cs:Ti:Br include no detectable Cs or Br. The CsBr thin film has detectable Ti signal suggesting that the film was thin and some TiO_2 underneath the film was visible. This makes sense in terms of the thinner CsBr films deposited by spin coating, rather than drop coating. Interestingly, despite XRD studies confirming unsuccessful conversion of the CsBr starting material to Cs_2TiBr_6, the peak area ratios of Cs_2TiBr_6 thin films are almost at the ideal bulk stoichiometry of 2:1:6 for Cs:Ti:Br. Given the proclivity of the large-grain material to forming metal oxides on nascent surfaces, these near ideal stoichiometries on Cs_2TiBr_6 thin films, combined with relatively small oxide features further suggests improved stability.

$TiBr_4$ loadings did not seem to have an impact on conversion, as a large amount of excess $TiBr_4$ was present after the three reaction set-ups were cooled. However, this excess of $TiBr_4$ could present future stability issues which prompted the addition of a getter step to draw $TiBr_4$ away from cooling FTO substrates. In our hands this getter step did not have a large effect on discouraging excess $TiBr_4$ from recrystallizing near the samples. Beyond $TiBr_4$ loadings, reaction duration was another variable of Cs_2TiBr_6 thin film synthesis considered but not explored in depth due to time constraints.

5.5 Atomic Layer Deposition of TiO_2 onto Cs_2TiBr_6 Thin Films

Atomic layer deposition of TiO_2 onto Cs_2TiBr_6 thin films followed optimized protocols from the commissioning experiments detailed previously in §4.3. We estimate a ~1 nm thickness of TiO_2 following a 10-cycle deposition with the belief that each cycle equates to one atomic layer of TiO_2 (1 Å). Each cycle consisted of one TEMATi pulse with 3 μpulses that was followed by one H_2O pulse with 2 μpulses.

X-ray photoelectron spectra of the resulting TiO_2 layer on the Cs_2TiBr_6 thin films was collected to establish surface chemistry. Figure 5.5 presents the representative Cs $3d_{5/2}$, O 1s, Ti 2p, C 1s, and Br 3d X-ray photoelectron regions of the thin films. Thin films in Fig. 5.5 include a (A) nascent Cs_2TiBr_6 thin film

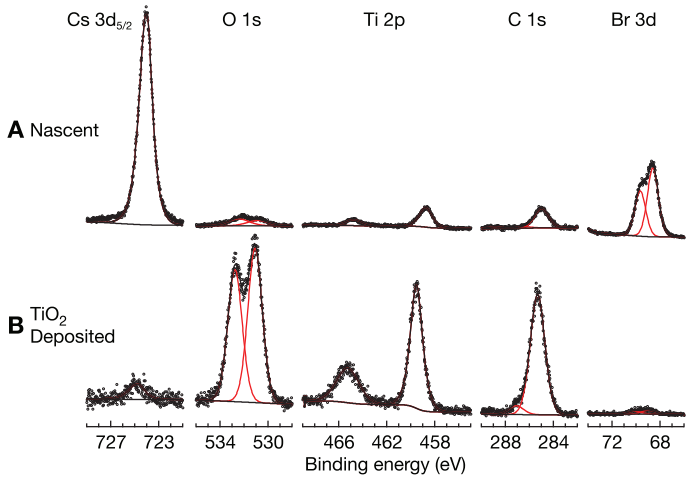

Figure 5.5 Representative XP spectra of a (**A**) nascent Cs_2TiBr_6 thin film and (**B**) a TiO_2 deposited by ALD onto a Cs_2TiBr_6 thin film on TiO_2 thin films on FTO substrates. TiO_2 deposited surfaces contained ~1 nm of TiO_2 (10 cycles) and had very little relative Cs and Br signal compared to substrate signals from depositions onto Si. The total *y*-axis amplitude of photoelectron counts is normalized between each frame.

on FTO and a (B) Cs_2TiBr_6 thin film with 10 cycles of ALD deposited TiO_2 on its surface. Figure 5.5 normalizes the spectra between frames based on the cumulative area of all presented features. The cesium region of the spectrum demonstrated a singular feature in frames A and B at ~723 eV that we ascribe to lattice Cs^+. For frames A–B, we ascribe a feature at ~530 eV in the O 1s region to metallic oxides. The higher binding energy feature in each O 1s region is likely dominated by the surface hydroxyl groups, –OH, that reports assign as 532.9 eV for titanium hydroxide[30] but may contain trace contributions of adventitious, oxidized contaminants as well. As expected, the TiO_2 deposited sample in frame B contains significantly higher oxide contributions than the nascent Cs_2TiBr_6 thin film in frame A. One doublet describes well the Ti 2p region throughout all samples studied that we ascribe to Ti^{4+} with Ti $2p_{3/2}$ at ~459 eV and Ti $2p_{1/2}$ at ~465 eV. Both lattice and interfacial oxidized titanium likely contribute to the cumulative photoelectron signal and cannot be easily deconvolved for the similar 4+ oxidation state of each titanium species. Contributions to the C 1s region include adventitiously adsorbed species at ~285 eV as well as features toward higher binding energy that would indicate oxidized adventitious contamination. Br 3d is well described by a singular d-orbital doublet with Br $3d_{5/2}$ at ~69 eV. Interestingly, the Cs $3d_{5/2}$ and Br 3d signals in the TiO_2 deposited sample in frame B are more attenuated than expected after a ~1 nm deposition which suggests that a reaction may be occurring between the Cs_2TiBr_6 and the ALD precursors.

Table 5.3 XPS Ratios for Nascent and ALD Deposited TiO_2 Cs_2TiBr_6 Thin Films [a]

	Cs	Ti	Br
Nascent Cs_2TiBr_6 thin film	2.45	1	6.81
ALD TiO_2 on a Cs_2TiBr_6 thin film	0.03	1	0.08

[a] We consider sensitivity-factor-corrected peak-area ratios that are normalized to Ti ≡ 1 based on the Cs_2TiBr_6 stoichiometry.

Beyond the position of each representative spectral feature, the relative change in intensities yields significant insight into each surface composition. Table 5.3 displays sensitivity-factor-corrected peak area ratios for both Cs_2TiBr_6 surfaces under study that we normalize to Ti ≡ 1 for its contribution to the overall material stoichiometry. Each value in Table 5.3 represents the peak area ratios of the representative spectra in Fig. 5.5.

Figure 5.5 and Table 5.3 elucidate the effect of TiO_2 deposition on nascent Cs_2TiBr_6 thin film surfaces. Nascent surfaces have sensitivity-factor-corrected peak area ratios that are fairly close to the ideal bulk 2:1:6 stoichiometry for Cs:Ti:Br. However, TiO_2 deposited surfaces, while expected to somewhat vary from the 2:1:6 Cs:Ti:Br stoichiometry, significantly varied from the bulk stoichiometry of Cs_2TiBr_6 after only a ~1 nm deposition. This goes against our expectation of such a thin layer of deposited TiO_2 and further suggests that the reaction had deleterious effects to the Cs_2TiBr_6 surface. Further studies would be necessary to deconvolve the TiO_2 contributions to the Ti peak area ratio and the contributions of Ti in the Cs_2TiBr_6 lattice.

5.6 Discussion

5.6.1 Cs_2TiBr_6 and CsBr Thin-Film Optimization

In our hands, we were unable to fully convert CsBr thin films to Cs_2TiBr_6. Instrumental and time limitations prevented characterization of further optimization efforts. Preliminary XRD data, as in Fig. 5.3, show that the CsBr(110) reflection was still present after a 72 h reaction with $TiBr_4$ vapor at 200 °C. We believe that the cause of this incomplete conversion is due to two possible variables. Firstly, CsBr thin film quality seems to be an area that requires further optimization in terms of uniformity and film thickness. One possible explanation that we believe could be the cause of incomplete conversion is that CsBr films were too thick for the $TiBr_4$ to intercalate into during the reaction. This resulted in only the surface of the films being converted to Cs_2TiBr_6 and would explain the nearly stoichiometric sensitivity-factor-corrected peak

area ratios of the surface of Cs_2TiBr_6 sample (Table 5.2). While the surfaces of the CsBr films were being stoichiometrically converted to Cs_2TiBr_6, the bulk of the material was not. This is supported by the surface sensitivity of XPS paired with the bulk sensitivity of XRD. Another cause of incomplete conversion of CsBr to Cs_2TiBr_6 could be poor temperature control. If the $TiBr_4$ vapor is not colliding with the CsBr films during the reaction, conversion is not possible. This was supported by the observation of $TiBr_4$ escaping through the first and second set-ups and suggests that temperature control may also be responsible for incomplete conversion. The third reaction set-up seemed to be successful in keeping the $TiBr_4$ vapor near the CsBr substrates during the reaction, however further XRD data would be needed to confirm such success.

5.7 Stability and Passivation of Cs_2TiBr_6 Thin Films

Qualitative observations of Cs_2TiBr_6 thin films suggests longer stability in ambient air. Samples did not change colors or appear wet until one hour of air exposure, which is a longer stability than that of large-grain samples that appear wet and lighter in color within minutes of air exposure. Quantitative studies using XRD would be necessary to better understand the timescales of this oxidation and are merited.

Given that even large grain material appears to decompose in air, further passivation of the surfaces is necessary. Preliminary passivation attempts with atomic layer deposited TiO_2 revealed that Cs_2TiBr_6 surfaces react during a 10-cycle deposition. X-ray photoelectron spectra revealed Cs and Br signals that were significantly more attenuated than expected. As demonstrated by XP spectra of TiO_2 deposited onto oxidized silicon substrates, substrate signal should still be relatively large following a 10-cycle deposition. While the existing Ti features of Cs_2TiBr_6 make it more difficult to deconvolve what belongs to the substrate and what belongs to the deposited film, it is clear that the Cs and Br signal were too attenuated to be only underneath ~1 nm of TiO_2.

Given the hygroscopic nature of Cs_2TiBr_6 and the fact that one of the ALD precursors is water, it is not unreasonable to consider that the H_2O may be interacting with the Cs_2TiBr_6 thin film rather than the TEMATi during depositions. Alternatively, TiO_2 layers may be porous, and water could be intercalating in subsequent cycles to react with the Cs_2TiBr_6 surfaces. In Chapter 3 we established that Cs_2TiBr_6 reacts with air to form amorphous TiO_2 on its surface and crystalline CsBr in its bulk. Therefore, a reaction between ALD precursors and Cs_2TiBr_6 surfaces may increase the overall thickness of the TiO_2 film to further attenuate the Cs and Br contributions from the substrate.

5.8 Conclusions and Future Work

We established a synthetic route for Cs_2TiBr_6 thin films by a reaction of $TiBr_4$ vapor with spin and drop deposited CsBr thin films on FTO substrates. We characterized the resulting films via XRD and XPS and found that despite surface chemistries resembling an ideal 2:1:6 Cs:Ti:Br stoichiometry, the bulk material contained unreacted CsBr. Optimization was undertaken to reduce the amount of unreacted CsBr but in our hands was unsuccessful in fully reacting the CsBr and merits further exploration. The resulting Cs_2TiBr_6 thin films qualitatively possessed a slightly longer stability in ambient air than that of the large-grain material, which is of interest in considering the properties of this material and also merits further exploration. We found that ALD deposited TiO_2 reacts with the Cs_2TiBr_6 surface, which indicates that optimization may be necessary in order to passivate the surfaces using ALD.

CHAPTER 6

FUTURE DIRECTIONS

We synthesized large-grain and thin film Cs_2TiBr_6. The properties of the resulting crystals were examined using multiple spectroscopic probes. We found that thin film and large-grain Cs_2TiBr_6 was not air-stable and degraded in air to form cesium bromide and titanium oxide. The electronic properties of Cs_2TiBr_6 differed based upon surface processing, with nascent samples having Fermi levels and work functions that were characteristic of TiO_2 and UHV cleaving yielding valence band structure that agreed with the density-of-state calculations for Cs_2TiBr_6 and a Fermi level indicative of an n-type semiconductor. Furthermore, we established the basicity of interfacial bromine species on both oxide-dominated and oxide-free surfaces, which provides a potential route for future soft organic contacts necessary for device relevant studies. However, preliminary studies that adsorbed Lewis acids to interfacial halides on large-grain Cs_2TiBr_6 surfaces did not improve ambient stability. These results hold promise for potential application in tandem-junction PV but present additional questions about the stability of the material, while surface metal oxide species present a potential route for future surface passivation.

With the results of these two explorations in mind, we developed and constructed a Schlenk-line integrated atomic layer deposition instrument to passivate Cs_2TiBr_6 surfaces with metal oxide electron transport layers. The ALD instrument allows for controlled deposition of single atomic layers of metal oxides and showed success in depositing films of varying thickness onto oxidized silicon surfaces.

While this work has produced promising results that contribute to cesium titanium bromide's future as a solar absorber candidate, its instability in ambient atmosphere remains an area of ongoing investigation. Future experiments are needed to optimize this material for tandem junction PV applications. Herein, we detail three potential routes for further optimizing and understanding Cs_2TiBr_6 as a solar-energy-conversion material.

6.1 Surface Attachment of Soft Organic Ligands

In Chapter 2 we established that Lewis acids adsorb to basic interfacial bromines. This ligand attachment was confirmed by XPS however, bond energy information would be useful in establishing the strength of these adsorbed species, especially when looking towards device-relevant studies. Temperature programmed desorption studies would be of great use in establishing binding energies of surface adsorbed ligands.

Additionally, in looking towards more device-relevant chemistry, junctions between Si and Cs_2TiBr_6 would likely have lattice mismatch, and junctions between Cs_2TiBr_6 and metal oxide passivating electron transport layers may change the surface chemistry of the Cs_2TiBr_6 itself. Therefore, when considering Cs_2TiBr_6 in a device sense it may be worthwhile to explore cation exchange and other ligand adsorption methods at the Cs_2TiBr_6 surface to not only facilitate carrier transport, but to also improve stability.

6.2 Optimization of Device-Relevant Thin Film Cs_2TiBr_6

Another device-relevant area of interest that merits further study based upon the findings of this work include optimizing Cs_2TiBr_6 thin film synthesis. As detailed in Chapter 5, we were not successful in fully converting CsBr thin films to Cs_2TiBr_6 in the presence of $TiBr_4$. A layered configuration of FTO / CsBr / Cs_2TiBr_6 presents issues in terms of carrier transport as the CsBr layer is insulating. Therefore, it is of interest to improve these thin films for further photoelectrochemical characterization.

We believe that CsBr thin films and temperature control during the reaction of $TiBr_4$ vapor with CsBr films are the most important variables in improving the synthesis of this thin film material. Spin deposition seemed to yield films of ideal thickness for optimal conversion, however these films often had issues

with uniformity which would present issues during photoelectrochemical characterization in the form of short circuits.

Analytical techniques such as X-ray diffraction and scanning electron microscopy would be incredibly valuable in establishing an ideal synthetic method. However, instrumental limitations (XRD always broken) present a challenge to the former characterization method and charging issues present a challenge to the latter characterization method.

6.3 Passivation of Cs_2TiBr_6

Finally, in considering future directions for the improvement of Cs_2TiBr_6 as a top absorber in a tandem junction PV configuration, passivation will be necessary. In Chapter 3 we established that the band edges of oxide-free Cs_2TiBr_6 surfaces are well aligned for facile electron transport by TiO_2. And in Chapter 4 we detailed the construction and testing of a Schlenk-line integrated ALD instrument which would enable air free sample transfer and depositions of metal oxides onto Cs_2TiBr_6 surfaces. Establishing a protocol for depositing metal oxides onto Cs_2TiBr_6 surfaces and examining the resultant stability of such passivated surfaces would be of great interest in furthering the stability of this material.

Initial studies (Fig. 5.5) of a ~1 nm ALD deposition of TiO_2 onto Cs_2TiBr_6 thin films suggests some kind of surface reaction occurring between the Cs_2TiBr_6 interface and the ALD precursors. This was supported by the small amount of Cs and Br signal relative to Ti and O signal in XPS. This indicates that reactivity studies will need to be conducted in order to elucidate the nature of and eventually prevent the reaction of ALD precursors with the Cs_2TiBr_6 surface. These studies would include doing 1–2 cycles to view how initiation of deposition occurs and the resulting chemical speciation. Much is unknown about the porosity of the deposited metal oxide and water precursors may be able to intercalate into already deposited layers to interact with the Cs_2TiBr_6 surface. Shutting this reaction and all other side reactions down may be done by simply increasing furnace temperature or by adding annealing steps between cycles. While initial passivation attempts brought up more questions than answers about the delicate stability of this material, these results also present many future routes to learn more about this promising solar energy material.

A

SUPPORTING INFORMATION FOR CHAPTER 3

A.1 Experimental Section

A.1.1 Materials and Chemicals

All chemicals were used as received unless otherwise noted. Chemicals used in the synthesis of cesium titanium bromide included cesium bromide (CsBr, 99.9% trace metals basis, Sigma Aldrich), and titanium(IV) bromide ($TiBr_4$, 98%, Sigma Aldrich) that was further purified by sublimation. Dichloromethane (DCM, ACS Grade, Fisher) was dried in a commercial solvent drying system and was further degassed then stored over molecular sieves (3Å, Alfa Aesar, freshly activated prior to use). A Milli–Q filtration system provided all water at 18 MΩ cm resistivity (Millipore).

Inert environments for sample synthesis, processing, reactions, and storage included an argon-purged (ultrahigh purity, UHP, Airgas) Schlenk line equipped with an oil diffusion pump having a base pressure below 1×10^{-3} torr. Larger inert environments included a nitrogen-purged (UHP, Airgas) recirculating glove box (mBraun Inc., Stratham, NH) with an active catalyst to maintain oxygen concentrations below 1 ppm, as measured by a commercial O_2 sensor. A commercial N_2 generator (Model N2-45, Parker Balston, Lancaster, NY) provided the atmosphere for a flush box (Terra Universal, Fullerton, CA) with an O_2 concentration below 5 ppt (thousand), as measured at a commercial O_2 sensor.

A.2 Synthesis of Large-Grain Cs_2TiBr_6

Prior to the synthesis of cesium titanium bromide, titanium(IV) bromide was purified via vacuum sublimation on the Schlenk line and transferred to the recirculating glove box. Cesium bromide was opened under an air ambient, covered with a laboratory wipe, and remained in the recirculating glove box antechamber overnight prior to entry.

All synthesis reactions proceeded in quartz ampoules. The ampoules were prepared from quartz tubes (19 mm O.D., 17 mm I.D., GM Associates, Oakland, CA and Technical Glass Products, Painesville, OH) by sealing one end in a propane-oxygen flame and cut- ting to 45 cm lengths. Prior to use, the ampoules were submerged in a 10 wt % solution of $KOH_{(aq)}$ for at least 48 h, rinsed thoroughly in water, and stored in a >100 °C oven until use. Inside the recirculating glove box, we loaded cesium bromide and titanium(IV) bromide with a 10% stoichiometric excess of $TiBr_4$ to a total reagent mass of 3 ± 0.3 g. For transfer out of the recirculating glove box and onto a Schlenk line for ampoule sealing, a KF-flanged butterfly valve and a 0.75-inch, ultra-torr-style compression fitting isolated the tube from the air ambient.

Ampoules were sealed in an in-house built tube-sealing apparatus described earier,[46] and shown in Fig. A.1. In brief, the apparatus is built around a repurposed rotary evaporator (Rotavapor R110, BÜCHI) to rotate the tube during in vacuo sealing to assure even, consistent heating, and steady, safe flamework. In place of a solvent trap, a direct connection to the Schlenk line affords high vacuum conductivity and rapid pumping (50 mm Rotavap flange adapter, Adams & Chittenden Scientific Glass Coop., Berkeley, CA). Sealing against the rotavapor vacuum gasket, a 6061 aluminum tube replaces the standard vapor tube and with a bottom connection consisting of a KF flange in place of a traditional 24/40 ₹ fitting. For sealing, a loaded tube was transferred to the sealing apparatus and initially evacuated with the butterfly valve closed to minimize possible contamination of the highly reactive $TiBr_4$ with oxygen. Prior to opening the butterfly valve, the reactants at the bottom of the ampoule were submerged in liquid nitrogen to minimize unwanted

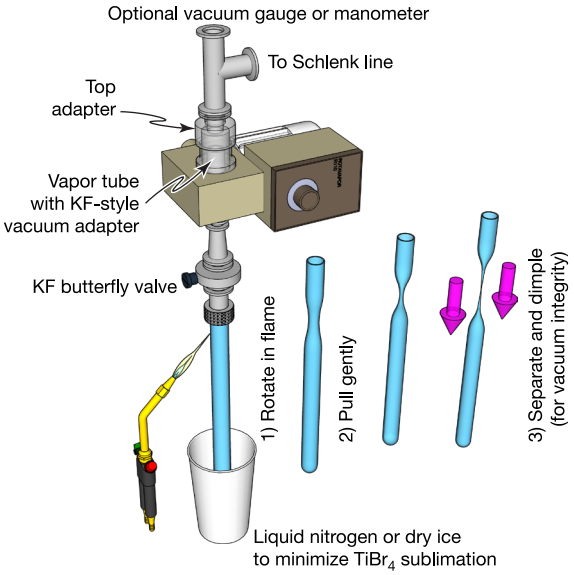

Figure A.1 Cartoon depiction of the tube-sealing setup. Due to the instability of $TiBr_4$ in an air ambient, tubes are loaded in a recirculating glove box and isolated from the atmosphere with a ultratorr-to-KF-flange adapter and a KF-flange butterfly valve. A Styrofoam cup holding either liquid nitrogen or dry ice minimizes sublimation of $TiBr_4$ during tube evacuation.[26]

vacuum sublimation of $TiBr_4$. Following evacuation of the connecting tubing, the butterfly valve was opened to the Schlenk line slowly to fully evacuate the quartz tube. The quartz tube was rotated at ~1 Hz and a propane-oxygen flame sealed the tube to yield a 22–25-cm-long ampoule.

High-temperature melt syntheses utilized horizontally mounted 5-cm-I.D. tube furnaces that were constructed from two abutting tubular ceramic heaters (CRFC-series, Omega Engineering, Norwalk, CT). A 30-cm-long and a 15-cm-long heater defined two independently controlled heating zones. Temperature controllers (Love 32B, Dwyer Instruments, Michigan City, IN) recorded temperatures at K-type thermocouples (Nextel ceramic braid insulation, Omega Engineering, spot welded in house) that were positioned at the center of each zone. An in-house-written LabVIEW program interfaced with the temperature controllers for conducting temperature ramp-and-soak profiles and recording temperature data.

Melt reactions utilized a 15-h linear ramp step to 680 °C at the reactant end of the ampoule and 710 °C at the opposite end of the ampoule, and a 25-hour soak step at 680 and 710 °C. Cooling consisted of a 96-hour linear ramp step to room temperature during which the reactant end remained 30 °C lower in

temperature relative to the opposite end of the ampoule. Certain synthesis runs utilized a rapid cooldown of the opposite end of the ampoule starting at 300 °C in the cooldown phase so as to getter unreacted $TiBr_4$ away from the reactant end, but that did not yield large-grain material and we do not consider that cooldown strategy further. Following synthesis, ampoules were transferred to a flush box and cracked open to reveal dark-red, polycrystalline Cs_2TiBr_6 samples of ~1 cm^3 total volume with visible facets in excess of 1 mm^2 in area. Crystals were transferred from the flush box to the recirculating glove box in sealed containers for storage until further use.

A.2.1 Surface Processing

Samples analyzed via photoelectron spectroscopy included nascent crystals with no surface preparation, DCM-rinsed, physically abraded, a sequential rinsing in DCM followed by physical abrasion, UHV surface cleaving, and air exposure following UHV cleaving. In the flush box, rinsing consisted of repeated ~1 mL applications of dichloromethane that yielded a yellow coloration of the collected liquid that likely resulted from the removal of interfacial $TiBr_4$. Rinsing was repeated with fresh DCM until the collected liquid remained colorless. Physical abrasion in the flush box consisted of sanding with 400-grit sandpaper (Saint-Gobain Abrasives Inc., Worcester, MA). Typical durations between physiochemical processing, sample mounting and air-free sample transfer to the XPS, and subsequent evacuation of the sample transfer suitcase was 10–20 min.

A modification to the photoelectron spectrometer described below enabled UHV sur- face cleaving. We fastened a commercial straight-edge razor blade to the magnetically coupled transport arm that moves samples between the ultrahigh vacuum analysis chamber and the high-vacuum, temperature-programmed-desorption side chamber.[29] The fastened blade enabled cleaving of a Cs_2TiBr_6 sample mounted on a PHI sample puck (Model 190; Physical Electronics, Inc.; via RBD Instruments, Inc., Bend, OR) while in the analysis chamber. During cleaving, analysis chamber pressures remained at or below 1×10^{-8} torr as measured at a UHV ion gauge. XPS and UPS analyses directly followed UHV cleaving on freshly exposed regions of the sample with a maximum of 20 minutes between sample cleaving and photoelectron data acquisition.

For air exposures that followed UHV cleaving and photoelectron analyses, samples were transferred from the analysis chamber to the instrument load lock that was subsequently equilibrated to an air ambient. Following ten minutes under the ambient atmosphere of 20 °C and 40–50% relative humidity, the load lock was re-evacuated for photoelectron analyses.

A.2.2 Photoelectron Spectroscopy

A PHI 5600 multitechnique system with a third-party data acquisition system (RBD Instruments, Inc.) acquired all X-ray and UV photoelectron spectra detailed earlier.[28–29,45–46] Analysis chamber base pressures were $< 1 \times 10^{-9}$ torr. A hemispherical energy analyzer collected the photoelectrons for both X-ray and ultraviolet photoelectrons. A monochromated Al Kα source provided X-rays at a 90° angle with respect the takeoff angle for the energy analyzer. Typical XPS data collection utilizes a level sample puck that yields 45° angles both for the incoming monochromated X-radiation and for the photoelectron take-off angle with respect to the sample normal angle. Typical UPS data collection utilizes direct alignment of the sample normal angle with the photoelectron takeoff angle that yields a ~51° angle between that angle and the incoming He I UV radiation.

In the recirculating glove box, samples were mounted on freshly cleaned sample pucks using carbon adhesive tape. For samples to be subjected to UHV cleaving, we additionally applied Hysol 1C epoxy between the sample and the puck for rigidity and allowed the epoxy to cure for 48 h. Epoxy components were pumped in small volumes with sufficient time in the antechamber to effect degassing. A vacuum suitcase (Transfer Engineering and Manufacturing, Inc., Fremont, CA) enabled air-free transfer of puck-mounted Cs_2TiBr_6 samples from the recirculating glove box to the instrument load lock.

X-ray photoelectron acquisitions included wide-energy survey scans as well as high-resolution scans of the C 1s, O 1s, Ti 2p, Cs $3d_{5/2}$, and Br 3d regions for all samples. Survey spectra utilized a 117 eV analyzer pass energy, a 0.5 eV step size, and a 50-ms-per-step dwell time. High-resolution spectra employed a 23.5 eV pass energy, a 0.025 eV step size, and a 50-ms-dwell-time per step. Nascent samples with no surface processing necessitated charge neutralization, while all other samples did not require charge neutralization. Neutralization parameters were optimized to yield a C 1s feature from adventitious contaminants of minimal full-width-at-half maximum (fwhm) value that was corrected to 285.0 eV during post-acquisition analyses.

Peak quantification utilized an in-house-developed LabVIEW program based on published spectral shapes and corrected for instrument-specific sensitivity factors,[31,47] and background-energy-loss functions.[48–50] A universal Tougaard-style baseline with $B = 2900$ eV^2 and $C = 1643$ eV^2 was utilized for the Cs $3d_{5/2}$ and Br 3d regions;[48–49] a Shirley-style baseline was used for the Ti 2p region;[50] and linear baselines described the C 1s, and O 1s regions. Data fitting employed baseline-corrected, pseudo-Voigt, GL(x)-style functions where x non-linearly scales from a pure Gaussian ($x = 0$) to a pure Lorentzian ($x = 100$).[47] GL(30) peak shapes described the C 1s, O 1s, Br 3d, and Ti $2p_{1/2}$ regions. GL(70) peak shapes were utilized for the Cs $3d_{5/2}$ and Ti $2p_{3/2}$ regions. Fits that employ multiple peaks within a spectral region were constrained to identical full-width-at-half-maximum (fwmh) values for

each peak, with the exception of Ti 2p spectra. We report sensitivity-factor-corrected XPS peak areas (raw peak area ÷ respective sensitivity factor). We employed instrument- and analyzer-specific sensitivity factors for photoelectron collection at 90° with respect to the incident X-ray beam. Sensitivity factors for Cs $3d_{5/2}$, C 1s, O 1s, Br 3d, and Ti 2p were 6.032, 0.296, 0.711, 0.895, and 1.789 respectively.[31]

For ultraviolet photoelectron spectroscopy, a gas discharge lamp (UVS 40A2, Prevac, Rogów, Poland) generated the He I spectroscopic line, $\mathbf{E}_{\mathrm{He\,I}} = h\nu$ = 21.218 eV. We utilize a –35 V substrate bias versus the grounded sample chamber to both maximize the desired spectral contributions of electrons from the sample and isolate unwanted secondary electrons from the analyzer. We chose the –35 V bias based on an invariance in spectral features and good linearity in analyzer response for UP spectra of a freshly Ar^+-sputtered gold foil between biases of –20 and –50 V vs the sample chamber ground. UP spectra of a freshly Ar^+ sputtered gold foil verified instrumental calibration with the bias-corrected Fermi level of gold, $\mathbf{E}_{\mathrm{F,\,Au}} \equiv 0.00 \pm 0.05$ eV. From plots of photoelectron counts vs bias-corrected binding energy, the x-axis intercept of linear regressions quantifies a secondary-electron-cutoff energy, $\mathbf{E}_{\mathrm{SEC}}$, and a valence-band-edge (maximum) energy, $\mathbf{E}_{\mathrm{VBM}}$. Considering the binding energy calibration of the instrument, we report sample work function values, ϕ, as the difference between $\mathbf{E}_{\mathrm{He\,I}}$ and the secondary electron cutoff energy, or $\phi = \mathbf{E}_{\mathrm{He\,I}} - \mathbf{E}_{\mathrm{SEC}}$. We report Fermi-level energies vs valence-band-maximum energies, or $\mathbf{E}_{\mathrm{F}} - \mathbf{E}_{\mathrm{VBM}}$. As ultrahigh vacuum bakeouts can yield a small perturbation in instrument calibration and spatial alignment that would deleteriously affect data analyses, both gold calibration and Cs_2TiBr_6 data were acquired during the same "bakeout window."

A.2.3 X-ray Diffraction

A Bruker-AXS D8 focus powder X-ray diffractometer with Cu K? radiation collected X- ray diffraction (XRD) data in the range of 10–45° (2θ) with a step size of 0.05° and a 5-s-dwell-times per step. X-ray tube operating conditions were 40 kV and 40 mA. In the flush box, Cs_2TiBr_6 samples were sandwiched between the XRD sample mount and low-static Kapton tape (KaptonTape.com, Torrance, CA) to minimize contact with ambient air during data acquisition. For studies of the evolution of XRD trace features as a function of air exposure, the Kapton tape was removed for sample exposure to an air ambient. Air exposure utilized two distinct protocols. In one protocol, either 10- or 100-minute air exposures were followed by transfer back into the recirculating glove box, resealing under Kapton, and full 10–45° trace acquisitions as above. In the second protocol, Kapton tape was removed, and a sample as successively and repetitively scanned in 10-min intervals at 2θ angles between of 28–30.5° (2θ) with a step size of 0.02° and 4-s dwell times per step. The Cs_2TiBr_6(222) and CsBr(110) reflections in the XRD traces gath-

ered in the range of 28–30.5° (2θ) were fitted in Igor Pro (WaveMetrics, Lake Oswego, OR) to yield the peak areas $A_{Cs_2TiBr_6}$ and A_{CsBr}. The relative intensities were subsequently calculated by normalizing the $A_{Cs_2TiBr_6}$ and A_{CsBr} values to the total fitted peak area, $A_{Cs_2TiBr_6} + A_{CsBr}$.

A.2.4 UV-Vis Spectroscopy

A UV-Visible spectrometer (Evolution 300, Thermo Fisher Scientific, Waltham, MA) collected scattered light from Cs_2TiBr_6 samples mounted in a Praying Mantis diffuse reflection accessory (Harrick Scientific Products, Pleasantville, NY) and sealed with Kapton tape. The sample holder with Kapton tape serves as the background reference for each scan. Scans were obtained in a range of 300 nm to 1000 nm, using a scan speed of 160 nm min^{-1} and a bandwidth of 1 in absorbance mode.

A.2.5 Imaging

A Tescan Analytics Vega3 (Tescan Orsay Holding, A.S., Brno-Kohoutovice, Czechia) SEM with a tungsten cathode operating at a 10 kV acceleration potential and a secondary-electron detector acquired the images in Fig. 3.1B–C. A Hitachi TM3000 TableTop SEM (Hitachi High-Tech America, Inc., Schaumburg, Illinois) operating with a 15 kV acceleration potential, a four-segment backscatter electron detector, and a silicon drift detector for energy-dispersive X-ray (EDX) analysis yielded the images in Fig. 3.1D–E. The EDX was calibrated using a copper grid standard and a built-in calibration curve provided by Hitachi. Samples for SEM and EDX analyses were prepared in the recirculating glovebox and transported to the instruments in sealed vials with rapid transfer for SEM analyses.

A.2.6 Computational Methods

We modeled a bulk cell of Cs_2TiBr_6 using DFT to obtain details on its electronic structure. We used a unit cell based on a $Fm\bar{3}m$ space group (number 225) with a unit cell length of $a = b = c = 1.092$ nm and a Ti–Br distance of 0.273 nm to match published XRD results. We used the Vienna *Ab Initio* Simulation Package (VASP)[51–54] for the simulations. Core electrons were represented by projector augmented wave (PAW) potentials,[73–74] while valence electrons were represented by a plane-wave basis set with a cutoff energy of 450 eV. Calculations used the HSE06 exchange correlation functional,[75] and were spin-polarized. We used a $2 \times 2 \times 2$ k-point mesh to sample reciprocal space.

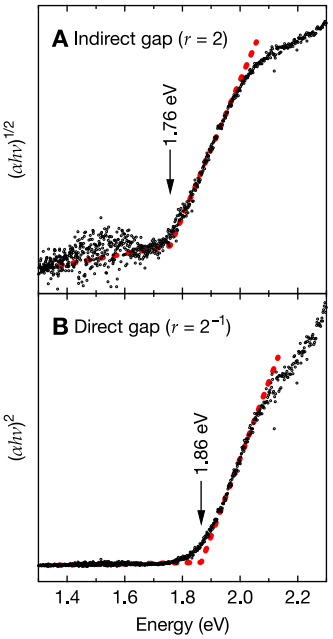

Figure A.2 UV-Vis data plotted as $(\alpha h\nu)^{1/r}$ vs energy for large-grain Cs_2TiBr_6 showing (**A**) the indirect band gap of the material at 1.76 eV for $r = 2$, and (**B**) the direct band gap of the material at 1.86 eV when $r = 2^{-1}$.[26] ©2020 American Chemical Society

A.3 Supplemental Results

A.3.1 Absorption-Spectra-Derived Band Gap Energies

As synthesized from a high-temperature melt and a long cooling period, crystals appeared red-black to black with red fringing along thin edges. Scattering patterns demonstrated crystal facets with areas in excess of 1 mm^2.

Figure A.2 presents $(\alpha h\nu)^{1/r}$-vs-energy Tauc plots for large-grain Cs_2TiBr_6 samples that were loaded into the UV-Vis sample holder under an inert atmosphere and isolated with Kapton tape. Linear fits to the absorption onset feature when $r = 2$ in frame A reveal a baseline-corrected energy-axis intercept of 1.76 eV, and 1.86 eV when $r = 2^{-1}$ as presented in frame B. Therefore, extrapolations respectively indicate indirect and direct forbidden energy gaps of 1.76 and 1.86 eV for the dark-red, large-grain Cs_2TiBr_6 material under study. This agrees well with early reports of 1.8 eV band gaps for thin film Cs_2TiBr_6,[24–25] and somewhat lower as compared to the 1.9 eV indirect and 2.0 eV direct band gaps from recent powder studies.[44]

B

UHV CLEAVING SET-UP

B.1 Construction of UHV Cleaving Set-Up

A UHV cleaving set-up was constructed to cleave Cs_2TiBr_6 in the XPS analysis chamber. The cleaving set-up was constructed so that it could clamp to the magnetically paired transfer arm within the TPD chamber.

In brief, the UHV cleaving set-up consisted of 3 rectangular aluminum pieces, each 1″ in width, $\frac{1}{4}$″ thick and varying length. Two of the pieces were 2″ long, while the third piece was 1″ long. The 2″ long pieces were equipped with tapped holes and one piece acted as a bottom while one acted as a top. The top and bottom pieces were able to clamp around the sample transfer fork with titanium screws holding the pieces in place around the fork. The third piece of machined aluminum was a 1×1″ square and could be attached to the top piece of the clamp to clamp a half of a razor blade in place. Figure B.1 shows the UHV cleaving set-up on the TPD sample transfer arm.

B.2 Standard Operating Protocols for UHV Cleaving

First, the TPD chamber was vented to atmosphere and the UHV cleaving set-up was attached to the sample transfer arm. The TPD chamber was then sealed and baked out for 24 h. Once baked out, the UHV cleaving set-up was ready for use.

Samples for UHV cleaving were prepared by mounting a Cs_2TiBr_6 crystal that was >1 cm^2 to an XPS puck with a $\frac{1}{8}$″ well. The crystal was carbon taped to the bottom of the well and Hysol 1C epoxy was applied to the edges of the crystal. The expoy cured for ~48 h at room temperature in the recirculating glovebox. Once cured, carbon tape was applied generously to the edges of the puck to catch any dust or chunks from cleaving. Once fully mounted, the sample was transferred to the XPS load lock via a vacuum suitcase.

Once on the sample stage in the XPS analysis chamber, the gate valve connecting the XPS and TPD chambers was opened, and the TPD sample transfer arm was slowly moved into the XPS chamber. Whilst looking through the 6″ Conflat window above the sample stage, the arm was slowly slid against the sample. A small amount of force and on some occasions hacking gently at the crystal while lowering the sample stage was required for successful cleaving. Figure B.2 shows what cleaving looked like up close.

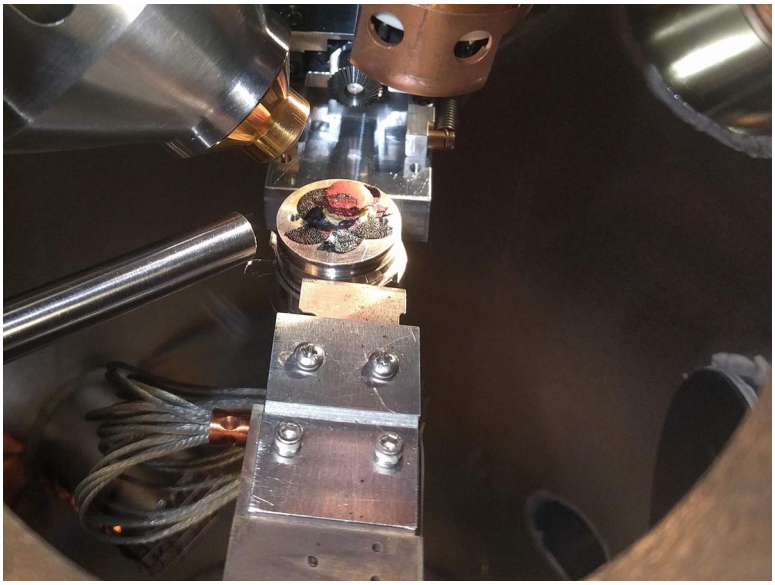

Figure B.1 The UHV cleaving set-up in the bottom of the image is moving towards the sample on the puck through the TPD chamber using the TPD sample transfer arm.

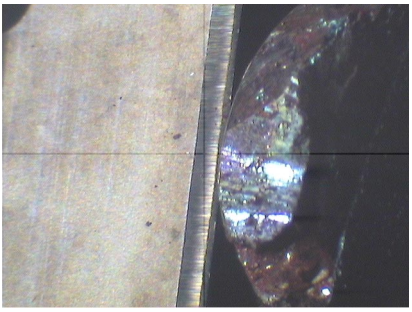

Figure B.2 A close-up image of the razor blade on the UHV cleaving set-up making contact with the Cs_2TiBr_6 crystal. Crystals were typically only cleaved about ~1 mm into the sample.

C

ATOMIC-LAYER DEPOSITION STANDARD OPERATING PROTOCOLS

The glass ALD reactor was loaded with substrates and sealed with the 90° elbow joints. The elbow joints were greased with high-temperature vacuum grease prior to sealing and were rotated within the glass reactor after sealing to ensure equal lubrication. As shown in the ALD image in Fig. 4.5, the stopcocks on the elbow joints were then put into the closed position and the sealed reactor was connected to the two Swagelok valves at the end of the ALD using black silicone tubing. While connecting the ALD reactor, care was taken to ensure that it sat evenly in the ALD furnace and that the thermocouple was touching the glass of the reactor. Copper wire held the silicone tubing in place for extra sealing. Once the reactor was connected, the ALD temperature program was set to "pre-run" temperatures. The bypass Swagelok valve was closed and the volume between the reactor stopcock and the right-most Swagelok valve was opened to evacuate the LN_2 trap. The right reactor stopcock was opened to pump down the reactor. Once pumping, the left reactor stopcock and the left Swagelok valve was opened.

After everything was under active vacuum, the left elbow of the reactor was wrapped with heating tape. Copper wire held the heating tape in place and fiber quartz and foil provided insulation. Then, the top portion of the reactor furnace was placed over the reactor and clamped in place. Arrangement of fiber quartz around the circular openings on either end of the reactor furnace ensured insulation of the furnace itself.

Once sealed, the ALD temperature program was set to ALD running temperatures and the dosing and flow program was set. A typical dosing program employed a 30–90-minute wait and 5 sccm flow. The wait was employed to ensure that every portion of the ALD had gotten to temperature. The dosing program was set for specific μpulses of water and TEMATi precursors. Once set, the program was run. After running the program, the liquid nitrogen dewars for the ALD trap and the Schlenk line trap were refilled. These dewars were topped off during the depositions.

After completion of the dosing program, the temperature program was set to "standby" temperatures and the reactor furnace was opened to accelerate the cooling of the reactor. In some cases, extra water pulses were manually done to fully react the pyrophoric TEMATi precursor. Once the TEMATi had been quenched, the flow was set to 0 sccm and the reactor was fully evacuated. Once fully evacuated, the left Swagelok valve and left stopcock were closed. The inert gas line on the Schlenk-line was used to backfill the reactor with UHP argon or nitrogen. Once filled, the right stopcock and right Swagelok valve were closed. In the event that the substrate was air sensitive, the reactor was left under vacuum before detaching.

To detach the reactor, both Swagelok valves connected to the stopcocks were closed, the left elbow was unwrapped and the copper wires holding the black silicone tubing in place were removed. The reactor was carefully detached. To open the reactor, one of the stopcocks was opened to air and the samples were tweezed out of the reactor.

Following successful ALD, both traps were dropped and cleaned while the ALD manifold and down tube remained under passive vacuum. Upon reattachment, the ALD was left under active vacuum.

D

CESIUM TITANIUM(IV) BROMIDE HIGH-TEMPERATURE MELT PARAMETER TABLE

Table D.1 Cs_2TiBr_6 High-Temperature Melt Parameter Table [a]

Batch	Tilted Up?	Grinding?	CsBr Loading	$TiBr_4$ Loading	$TiBr_4$ Excess	T_{soak} front	T_{soak} back	t_{ramp}	t_{soak}	$t_{cooling}$	Facets
1	no	no	0.005	0.0025	1.00	200	200	600	600	600	no
3[†]	no	no	0.005	0.0025	1.00	750	750	900	1500	3000	no
4	no	no	0.005	0.0025	1.00	515	515	0	30	4500	yes?
5	no	yes	0.005	0.0025	1.00	800	800	900	1800	7000	no
6	no	yes	0.005	0.0025	1.00	700	700	1800	900	7200	no
7	no	yes	0.007	0.00375	1.00	700	700	1800	1400	6700	no
8	no	yes	0.005	0.0025	1.00	*n/a*	*n/a*	*n/a*	*n/a*	*n/a*	*n/a*
9	no	yes	0.005	0.0025	1.00	700	800	300	600	6300	no
10	yes	yes	0.003	0.00125	1.00	700	800	300	600	9350	no
11	no	yes	0.003	0.00125	1.00	700	800	600	600	9000	no
12	no	yes	0.003	0.00125	1.00	700	800	600	600	9000	yes
13	no	yes	0.005	0.00253	1.00	680	730	900	900	7800	no
14	yes	yes	0.005	0.00253	1.00	680	705	900	900	7800	no

Batch	Tilted Up?	Grinding?	CsBr Loading	$TiBr_4$ Loading	$TiBr_4$ Excess	T_{soak} front	T_{soak} back	t_{ramp}	t_{soak}	$t_{cooling}$	Facets
15	yes	yes	0.008	0.00381	1.00	680	705	900	900	7800	no
16	yes	no	0.008	0.00381	1.00	680	705	900	900	2600	yes
17	yes	no	0.008	0.00381	1.00	670	700	900	900	5600	yes
18	yes	no	0.008	0.00419	1.10	680	705	900	900	7600	yes
19	yes	no	0.008	0.00419	1.10	680	700	900	1800	6500	yes
20	yes	no	0.008	0.00419	1.10	680	710	900	1500	6500	yes
21	yes	no	0.008	0.00397	1.04	680	710	900	1500	6800	yes
22	yes	no	0.008	0.00397	1.04	680	710	900	1500	6500	*n/a*
23	yes	no	0.008	0.00419	1.10	680	710	900	1500	6500	yes
24	yes	no	0.008	0.00419	1.10	680	710	900	1500	6500	yes
25	yes	no	0.008	0.00419	1.10	680	710	900	1500	6500	yes
26	yes	no	0.008	0.00419	1.10	680	710	900	1500	6500	yes

[a] All loadings are in moles. All Temperatures are in °C. All times in min. [†] Crystal growth batch 2 exploded, so no results are recorded.

E

PHOTOELECTROCHEMICAL EXPERIMENTS GUIDE

Given the overall time constraints of the project, the photoelectrochemical measurements of Cs_2TiBr_6 thin films were not successfully collected and represents an important target for future study. For future photoelectrochemical experiments, consult Curtis Doiron's MQP thesis for the necessary redox couples, glassware, and data acquisition procedures.[76]

F

REFERENCES

1. Arguez, A.; Hurley, S.; Inamdar, A.; Mahoney, L.; Sanchez-Lugo, A.; Yang, L., Should We Expect Each Year in the Next Decade (2019–28) to Be Ranked among the Top 10 Warmest Years Globally? *Bull. Am. Meterorol. Soc.* **2020**, *101*, E655–E663.
2. Oreskes, N., The Scientific Consensus on Climate Change. *Science* **2004**, *306*, 1686.
3. Arvizu, D.; Balaya, P.; Cabeza, L.; Hollands, T.; Jäger-Waldau, A.; Kondo, M.; Konseibo, C.; Meleshko, V.; Stein, W.; Tamaura, Y.; Xu, H.; Zilles, R., Direct Solar Energy. In IPCC Special Report on Renewable Energy Sources and Climate Change Mitigation, Edenhofer, O.; Pichs-Madruga, R.; Sokona, Y.; Seyboth, K.; Matschoss, P.; Kadner, S.; Zwickel, T.; Eickemeier, P.; Hansen, G.; Schlömer, S.; von Stechow, C., Eds. Cambridge University Press: Cambridge, United Kingdom and New York, NY, USA, 2011.
4. Chueh, W. C.; Falter, C.; Abbott, M.; Scipio, D.; Furler, P.; Haile, S. M.; Steinfeld, A., High-Flux Solar-Driven Thermochemical Dissociation of CO_2 and H_2O Using Nonstoichiometric Ceria. *Science* **2010**, *330*, 1797–1801.

5. Walter, M. G.; Warren, E. L.; McKone, J. R.; Boettcher, S. W.; Mi, Q.; Santori, E. A.; Lewis, N. S., Solar Water Splitting Cells. *Chem. Rev.* **2010**, *110*, 6446–6473.

6. Lin, K.-T.; Lin, H.; Yang, T.; Jia, B., Structured graphene metamaterial selective absorbers for high efficiency and omnidirectional solar thermal energy conversion. *Nat. Commun.* **2020**, *11*, 1389.

7. Fu, H.-C.; Li, W.; Yang, Y.; Lin, C.-H.; Veyssal, A.; He, J.-H.; Jin, S., An efficient and stable solar flow battery enabled by a single-junction GaAs photoelectrode. *Nat. Commun.* **2021**, *12*, 156.

8. Jean, J.; Brown, P. R.; Jaffe, R. L.; Buonassisi, T.; Bulović, V., Pathways for solar photovoltaics. *Energy & Environ. Sci.* **2015**, *8*, 1200–1219.

9. Lewis, N. S., Research opportunities to advance solar energy utilization. *Science* **2016**, *351*, aad1920.

10. Bhattacharya, S.; John, S., Beyond 30% Conversion Efficiency in Silicon Solar Cells: A Numerical Demonstration. *Sci. Rep.* **2019**, *9*, 12482.

11. Horowitz, K. A. W.; Remo, T.; Smith, B.; Ptak, A., A Techno-Economic Analysis and Cost Reduction Roadmap for III–V Solar Cells. National Renewable Energy Laboratory: Golden, CO, 2018.

12. Zhao, D.; Wang, C.; Song, Z.; Yu, Y.; Chen, C.; Zhao, X.; Zhu, K.; Yan, Y., Four-Terminal All-Perovskite Tandem Solar Cells Achieving Power Conversion Efficiencies Exceeding 23%. *ACS Energy Lett.* **2018**, *3*, 305–306.

13. Green, M. A.; Jiang, Y.; Soufiani, A. M.; Ho-Baillie, A., Optical Properties of Photovoltaic Organic–Inorganic Lead Halide Perovskites. *J. Phys. Chem. Lett.* **2015**, *6*, 4774–4785.

14. Hailegnaw, B.; Kirmayer, S.; Edri, E.; Hodes, G.; Cahen, D., Rain on Methylammonium Lead Iodide Based Perovskites: Possible Environmental Effects of Perovskite Solar Cells. *J. Phys. Chem. Lett.* **2015**, *6*, 1543–1547.

15. Wygant, B. R.; Ye, A. Z.; Dolocan, A.; Vu, Q.; Abbot, D. M.; Mullins, C. B., Probing the Degradation Chemistry and Enhanced Stability of 2D Organolead Halide Perovskites. *J. Am. Chem. Soc.* **2019**, *141*, 18170–18181.

16. Shockley, W.; Queisser, H. J., Detailed Balance Limit of Efficiency of p?n Junction Solar Cells. *J. Appl. Phys.* **1961**, *32*, 510–519.

17. Guo, F.; Li, N.; Fecher, F. W.; Gasparini, N.; Quiroz, C. O. R.; Bronnbauer, C.; Hou, Y.; Radmilović, V. V.; Radmilović, V. R.; Spiecker, E.; Forberich, K.; Brabec, C. J., A generic concept to overcome bandgap limitations for designing highly efficient multi-junction photovoltaic cells. *Nat. Commun.* **2015**, *6*, 7730.

18. Yu, Z.; Leilaeioun, M.; Holman, Z., Selecting tandem partners for silicon solar cells. *Nat. Energy* **2016**, *1*, 16137.

19. Wang, Z.; Song, Z.; Yan, Y.; Liu, S.; Yang, D., Perovskite—a Perfect Top Cell for Tandem Devices to Break the S–Q Limit. *Adv. Sci.* **2019**, *6*, 1801704.

20. Kim, D.; Jung, H. J.; Park, I. J.; Larson, B. W.; Dunfield, S. P.; Xiao, C.; Kim, J.; Tong, J.; Boonmongkolras, P.; Ji, S. G.; Zhang, F.; Pae, S. R.; Kim, M.; Kang, S. B.; Dravid, V.; Berry, J. J.; Kim, J. Y.; Zhu, K.; Kim, D. H.; Shin, B., Efficient, stable silicon

tandem cells enabled by anion-engineered wide-bandgap perovskites. *Science* **2020**, *368*, 155–160.

21. Rong, Y.; Hu, Y.; Mei, A.; Tan, H.; Saidaminov, M. I.; Seok, S. I.; McGehee, M. D.; Sargent, E. H.; Han, H., Challenges for commercializing perovskite solar cells. *Science* **2018**, *361*, eaat8235.
22. Li, J.; Cao, H.-L.; Jiao, W.-B.; Wang, Q.; Wei, M.; Cantone, I.; Lü, J.; Abate, A., Biological impact of lead from halide perovskites reveals the risk of introducing a safe threshold. *Nat. Commun.* **2020**, *11*, 310.
23. Li, J.; Duan, J.; Yang, X.; Duan, Y.; Yang, P.; Tang, Q., Review on recent progress of lead-free halide perovskites in optoelectronic applications. *Nano Energy* **2021**, *80*, 105526.
24. Chen, M.; Ju, M.-G.; Carl, A. D.; Zong, Y.; Grimm, R. L.; Gu, J.; Zeng, X. C.; Zhou, Y.; Padture, N. P., Cesium Titanium(IV) Bromide Thin Films Based Stable Lead-Free Perovskite Solar Cells. *Joule* **2018**, *2*, 558–570.
25. Ju, M.-G.; Chen, M.; Zhou, Y.; Garces, H. F.; Dai, J.; Ma, L.; Padture, N. P.; Zeng, X. C., Earth-Abundant Nontoxic Titanium(IV)-based Vacancy-Ordered Double Perovskite Halides with Tunable 1.0 to 1.8 eV Bandgaps for Photovoltaic Applications. *ACS Energy Lett.* **2018**, *3*, 297–304.
26. Mendes, J. L.; Gao, W.; Martin, J. L.; Carl, A. D.; Deskins, N. A.; Granados-Focil, S.; Grimm, R. L., Interfacial States, Energetics, and Atmospheric Stability of Large-Grain Antifluorite Cs_2TiBr_6. *J. Phys. Chem. C* **2020**, *124*, 24289–24297.
27. Chénard, E.; Sutrisno, A.; Zhu, L.; Assary, R. S.; Kowalski, J. A.; Barton, J. L.; Bertke, J. A.; Gray, D. L.; Brushett, F. R.; Curtiss, L. A.; Moore, J. S., Synthesis of Pyridine– and Pyrazine–BF_3 Complexes and Their Characterization in Solution and Solid State. *J. Phys. Chem. C* **2016**, *120*, 8461–8471.
28. Carl, A. D.; Grimm, R. L., Covalent Attachment and Characterization of Perylene Monolayers on Si(111) and TiO_2 for Electron-Selective Carrier Transport. *Langmuir* **2019**, *35*, 9352–9363.
29. Gao, W. R.; Zielinski, K.; Drury, B. N.; Carl, A. D.; Grimm, R. L., Elucidation of Chemical Species and Reactivity at Methylammonium Lead Iodide and Cesium Tin Bromide Perovskite Surfaces via Orthogonal Reaction Chemistry. *J. Phys. Chem. C* **2018**, *122*, 17882–17894.
30. Krishnan, P.; Liu, M.; Itty, P. A.; Liu, Z.; Rheinheimer, V.; Zhang, M.-H.; Monteiro, P. J. M.; Yu, L. E., Characterization of photocatalytic TiO_2 powder under varied environments using near ambient pressure X-ray photoelectron spectroscopy. *Sci. Rep.* **2017**, *7*, 43298.
31. Moulder, J. F.; Stickle, W. F.; Sobol, P. E.; Bomben, K. D., Handbook of X-ray Photoelectron Spectroscopy; Perkin-Elmer Corporation: Physical Electronics Division, 1992.
32. Hwang, B.; Lee, J.-S., Hybrid Organic-Inorganic Perovskite Memory with Long-Term Stability in Air. *Sci. Rep.* **2017**, *7*, 673.
33. International Energy Agency, World Energy Outlook 2019, 2019.

34. Solangi, K. H.; Islam, M. R.; Saidur, R.; Rahim, N. A.; Fayaz, H., A review on global solar energy policy. *Renew. Sust. Energ. Rev.* **2011**, *15*, 2149–2163.

35. Essig, S.; Allebé, C.; Remo, T.; Geisz, J. F.; Steiner, M. A.; Horowitz, K.; Barraud, L.; Ward, J. S.; Schnabel, M.; Descoeudres, A.; Young, David L.; Woodhouse, M.; Despeisse, M.; Ballif, C.; Tamboli, A., Raising the one-sun conversion efficiency of III–V/Si solar cells to 32.8% for two junctions and 35.9% for three junctions. *Nat. Energy* **2017**, *2*, 17144.

36. National Renewable Energy Laboratory, Best Research-Cell Efficiency Chart. `https://www.nrel.gov/pv/cell-efficiency.html` (accessed May 20, 2020).

37. Qiu, L.; He, S.; Ono, L. K.; Liu, S.; Qi, Y., Scalable Fabrication of Metal Halide Perovskite Solar Cells and Modules. *ACS Energy Lett.* **2019**, *4*, 2147–2167.

38. Zhou, Y.; Chen, J.; Bakr, O. M.; Sun, H.-T., Metal-Doped Lead Halide Perovskites: Synthesis, Properties, and Optoelectronic Applications. *Chem. Mater.* **2018**, *30*, 6589–6613.

39. Meggiolaro, D.; Mosconi, E.; De Angelis, F., Formation of Surface Defects Dominates Ion Migration in Lead-Halide Perovskites. *ACS Energy Lett.* **2019**, *4*, 779–785.

40. Li, J.; Stoumpos, C. C.; Trimarchi, G. G.; Chung, I.; Mao, L.; Chen, M.; Wasielewski, M. R.; Wang, L.; Kanatzidis, M. G., Air-Stable Direct Bandgap Perovskite Semiconductors: All-Inorganic Tin-Based Heteroleptic Halides $A_xSnCl_yI_z$ (A = Cs, Rb). *Chem. Mater.* **2018**, *30*, 4847–4856.

41. Lang, F.; Gluba, M. A.; Albrecht, S.; Rappich, J.; Korte, L.; Rech, B.; Nickel, N. H., Perovskite Solar Cells with Large-Area CVD-Graphene for Tandem Solar Cells. *J. Phys. Chem. Lett.* **2015**, *6*, 2745–2750.

42. Boix, P. P.; Agarwala, S.; Koh, T. M.; Mathews, N.; Mhaisalkar, S. G., Perovskite Solar Cells: Beyond Methylammonium Lead Iodide. *J. Phys. Chem. Lett.* **2015**, *6*, 898–907.

43. Maughan, A. E.; Ganose, A. M.; Scanlon, D. O.; Neilson, J. R., Perspectives and Design Principles of Vacancy-Ordered Double Perovskite Halide Semiconductors. *Chem. Mater.* **2019**, *31*, 1184–1195.

44. Euvrard, J.; Wang, X.; Li, T.; Yan, Y.; Mitzi, D. B., Is Cs_2TiBr_6 a promising Pb-free perovskite for solar energy applications? *J. Mater. Chem. A* **2020**, *8*, 4049–4054.

45. Carl, A. D.; Kalan, R. E.; Obayemi, J. D.; Kana, M. G. Z.; Soboyejo, W. O.; Grimm, R. L., Synthesis and Characterization of Alkylamine-Functionalized Si(111) for Perovskite Adhesion With Minimal Interfacial Oxidation or Electronic Defects. *ACS Appl. Mater. Interfaces* **2017**, *9*, 34377–34388.

46. Martin, J. L.; Stoflet, R.; Carl, A. D.; Himmelberger, K. M.; Granados-Fócil, S.; Grimm, R. L., Quantification of Surface Reactivity and Step-Selective Etching Chemistry on Single-Crystal BiOI(001). *Langmuir* **2020**, *36*, 9343–9355.

47. Fairley, N. Peak Fitting in XPS. `http://www.casaxps.com/help_manual/manual_updates/peak_fitting_in_xps.pdf`.

48. Jansson, C.; Hansen, H. S.; Yubero, F.; Tougaard, S., Accuracy of the Tougaard method for quantitative surface analysis. Comparison of the Universal and REELS inelastic cross sections. *J. Electron Spec. Rel. Phen.* **1992**, *60*, 301–319.

49. Tougaard, S., Formalism for quantitative surface analysis by electron spectroscopy. *J. Vac. Sci. Technol. A* **1990**, *8*, 2197–2203.

50. Shirley, D. A., High-Resolution X-Ray Photoemission Spectrum of the Valence Bands of Gold. *Phys. Rev. B* **1972**, *5*, 4709–4714.

51. Kresse, G.; Hafner, J., Ab initio molecular dynamics for liquid metals. *Phys. Rev. B.* **1993**, *47*, 558–561.

52. Kresse, G.; Hafner, J., Ab initio molecular-dynamics simulation of the liquid-metal–amorphous-semiconductor transition in germanium. *Phys. Rev. B.* **1994**, *49*, 14251–14269.

53. Kresse, G.; Furthmüller, J., Efficient iterative schemes for ab initio total-energy calculations using a plane-wave basis set. *Phys. Rev. B* **1996**, *54*, 11169-11186.

54. Kresse, G.; Furthmüller, J., Efficiency of ab-initio total energy calculations for metals and semiconductors using a plane-wave basis set. *Comp. Mater. Sci.* **1996**, *6*, 15–50.

55. Gleason-Rohrer, D. C.; Brunschwig, B. S.; Lewis, N. S., Measurement of the Band Bending and Surface Dipole at Chemically Functionalized Si(111)/Vacuum Interfaces. *J. Phys. Chem. C* **2013**, *117*, 18031–18042.

56. Zhang, Z.; Yates, J. T., Band Bending in Semiconductors: Chemical and Physical Consequences at Surfaces and Interfaces. *Chem. Rev.* **2012**, *112*, 5520–5551.

57. Zhang, J.-Y.; Boyd, I. W.; O'Sullivan, B. J.; Hurley, P. K.; Kelly, P. V.; Sénateur, J. P., Nanocrystalline TiO_2 films studied by optical, XRD and FTIR spectroscopy. *J. Non-Cryst. Solids* **2002**, *303*, 134–138.

58. Maheu, C.; Cardenas, L.; Puzenat, E.; Afanasiev, P.; Geantet, C., UPS and UV spectroscopies combined to position the energy levels of TiO_2 anatase and rutile nanopowders. *Phys. Chem. Chem. Phys.* **2018**, *20*, 25629–25637.

59. Klug, J. A.; Weimer, M. S.; Emery, J. D.; Yanguas-Gil, A.; Seifert, S.; Schlepütz, C. M.; Martinson, A. B. F.; Elam, J. W.; Hock, A. S.; Proslier, T., A modular reactor design for in situ synchrotron X-ray investigation of atomic layer deposition processes. *Rev. Sci. Instrum.* **2015**, *86*, 113901.

60. Larrabee, T. J.; Mallouk, T. E.; Allara, D. L., An atomic layer deposition reactor with dose quantification for precursor adsorption and reactivity studies. *Rev. Sci. Instrum.* **2013**, *84*, 014102.

61. Leskelä, M.; Ritala, M., Atomic layer deposition (ALD): from precursors to thin film structures. *Thin Solid Films* **2002**, *409*, 138–146.

62. George, S. M., Atomic Layer Deposition: An Overview. *Chem. Rev.* **2010**, *110*, 111–131.

63. Xiong, M.; Gao, Z.; Qin, Y., Spillover in Heterogeneous Catalysis: New Insights and Opportunities. *ACS Catal.* **2021**, *11*, 3159–3172.

64. Hu, S.; Shaner, M. R.; Beardslee, J. A.; Lichterman, M.; Brunschwig, B. S.; Lewis, N. S., Amorphous TiO_2 coatings stabilize Si, GaAs, and GaP photoanodes for efficient water oxidation. *Science* **2014**, *344*, 1005–1009.

65. Lubitz, M.; Medina, P. A.; Antic, A.; Rosin, J. T.; Fahlman, B. D., Cost-Effective Systems for Atomic Layer Deposition. *J. Chem. Ed.* **2014**, *91*, 1022–1027.

66. Bermudez, V. M., Design and construction of a research atomic layer deposition system for in situ infrared and electron spectroscopies. *Rev. Sci. Instrum.* **2014**, *85*, 114101.

67. Selvaraj, S. K.; Jursich, G.; Takoudis, C. G., Design and implementation of a novel portable atomic layer deposition/chemical vapor deposition hybrid reactor. *Rev. Sci. Instrum.* **2013**, *84*, 095109.

68. Zhao, R.; Zhang, K.; Zhu, J.; Xiao, S.; Xiong, W.; Wang, J.; Liu, T.; Xing, G.; Wang, K.; Yang, S.; Wang, X., Surface passivation of organometal halide perovskites by atomic layer deposition: an investigation of the mechanism of efficient inverted planar solar cells. *Nanoscale Adv.* **2021**.

69. Mali, S. S.; Shim, C. S.; Park, H. K.; Heo, J.; Patil, P. S.; Hong, C. K., Ultrathin Atomic Layer Deposited TiO_2 for Surface Passivation of Hydrothermally Grown 1D TiO_2 Nanorod Arrays for Efficient Solid-State Perovskite Solar Cells. *Chem. Mater.* **2015**, *27*, 1541–1551.

70. Das, C.; Kot, M.; Hellmann, T.; Wittich, C.; Mankel, E.; Zimmermann, I.; Schmeisser, D.; Khaja Nazeeruddin, M.; Jaegermann, W., Atomic Layer-Deposited Aluminum Oxide Hinders Iodide Migration and Stabilizes Perovskite Solar Cells. *Cell Rep. Phys. Sci.* **2020**, *1*, 100112.

71. McDowell, M. T.; Lichterman, M. F.; Carim, A. I.; Liu, R.; Hu, S.; Brunschwig, B. S.; Lewis, N. S., The Influence of Structure and Processing on the Behavior of TiO_2 Protective Layers for Stabilization of n-Si/TiO_2/Ni Photoanodes for Water Oxidation. *ACS Appl. Mater. Interfaces* **2015**, *7*, 15189–15199.

72. Urbach, F., The Long-Wavelength Edge of Photographic Sensitivity and of the Electronic Absorption of Solids. *Phys. Rev.* **1953**, *92*, 1324–1324.

73. Kresse, G.; Joubert, D., From ultrasoft pseudopotentials to the projector augmented-wave method. *Phys. Rev. B* **1999**, *59*, 1758–1775.

74. Blöchl, P. E., Projector augmented-wave method. *Phys. Rev. B* **1994**, *50*, 17953–17979.

75. Krukau, A. V.; Vydrov, O. A.; Izmaylov, A. F.; Scuseria, G. E., Influence of the exchange screening parameter on the performance of screened hybrid functionals. *J. Chem. Phys.* **2006**, *125*, 224106.

76. Doiron, C. W., Modification of Back-Surface Contacts to Antimony Sulfide Active Layers Using Carrier-Selective Thionated Perylene Derivatives for Improved Photovoltaic Performance. Major Qualifying Project (MQP Thesis), Worcester Polytechnic Institute, Worcester, Massachusetts. E-project-030719-154643. 2019.